

https://dspace.org/

Synthesis and performance evaluation of optimized silica sodalite in polysulfone mixed matrix membranes for pre-combustion CO2 capture

Eden, Christin Leigh

2020

https://hdl.handle.net/10539/31310

Downloaded from a DSpace repository. https://dspace.org/



UNIVERSITY OF THE
WITWATERSRAND,
JOHANNESBURG

Synthesis and performance evaluation of optimized silica sodalite in polysulfone mixed matrix membranes for pre-combustion CO_2 capture

MSc RESEARCH DISSERTATION

Prepared by

Christin Leigh Eden
(803769)

Submitted to

School of Chemical and Metallurgical Engineering, Faculty of Engineering and the Built Environment, University of the Witwatersrand, Johannesburg, South Africa, for the Degree of Masters of Science in Chemical Engineering

Supervisor[s]: Prof. M.O. Daramola

September, 2020

Plagiarism declaration

I, Christin Eden (803 769), declare this work to be my own unaided work except where I have explicitly indicated otherwise. I have followed the required conventions in referencing the thoughts and ideas of others.

This work is submitted for the degree of Master of Science in engineering to the University of the Witwatersrand, Johannesburg, South Africa.



15/09/2020

Christin Eden (803 769) Date

Abstract

Increasing carbon dioxide emissions, resulting primarily from increasing energy demand and industrial activity, are a major concern for environmental climate change. This has led to a global movement towards CO_2 capture from point source emitters such as power plants. Membranes designed to purify H_2 from CO_2 and CO, such as in pre-combustion coal gasification, need to be thermally and mechanically stable with good separation performance in order to make them an economically attractive alternative to traditional separation methods. Polymeric membranes, although mechanically stable and inexpensive, exhibit a trade-off between permeability and selectivity. This limits their separation performance. Mixed matrix membranes which combine polymer matrix with inorganic zeolite particle, have the potential to increase the separation performance of H_2 from CO_2. Hydroxy sodalite (HSOD) is a common zeolite with potential applications in absorption and catalysis. The small cage aperture enables the permeation of small molecules such as hydrogen. However, traditional hydrothermal synthesis of HSOD results in occluded water and organic matter within the cage structures, hindering permeation. Attempts to remove these occluded molecules, through dehydration above 400 °C, result in the collapse of the cages, rendering the substance completely ineffective. Topotactic conversion has the potential to produce higher quality sodalite without the presence of occluded matter. However, previous research has exhibited discrepancies in the quality of the sodalite synthesized and the synthesis variables utilized.

This study aimed to produce high porosity silica sodalite through topotactic conversion and investigate the effects of synthesis variables such as; acid strength, acid treatment time, and calcination time and temperature on the textural and morphological quality of the sodalite. Silica sodalite was synthesized from the fabricated RUB-15 precursor and converted through topotactic conversion to SSOD through treatment with propionic acid and calcination. The synthesized sodalite was then utilized in mixed matrix membranes (silica sodalite/ polysulfone (PSF)) by dissolving the various loadings in PSF solution and casting to a thin film. The membranes were tested for hydrogen/carbon dioxide separation potential, membrane strength and thermal stability.

Preliminary investigation of the effect of synthesis variables via the response surface modelling approach revealed acid treatment time to be an insignificant influencing factor affecting the quality of silica sodalite prepared via topotactic conversion and was thus removed from further investigations. Consequently, higher acid strength, lower calcination time and temperature were observed to favour higher quality silica sodalite. Therefore, optimum synthesis variables obtained via the RSM approach were acid strength: 5 M, calcination time: 1 h treatment and

calcination temperature: 873 K. The sodalite reproduced under these conditions displayed higher surface area and pore volume than the HSOD crystals produced via traditional hydrothermal synthesis of 2.35 m^2/g and 0.012 cm^3/g, respectively but fell short of the model predicted SA and PV values of 148.5 m^2/g and 0.093 cm^3/g, respectively.

The subsequent stage of the study considered the utilization of the silica sodalite crystals as a filler in PSF membranes to form SSOD/PSF mixed matrix membranes. The improved separation performance of the fabricated membranes over that of the pure PSF membrane was evaluated via single gas permeation and mixed gas separation using pure H_2 and CO_2; and mixed CO_2/H_2 gas (40:60), respectively. The tests were carried out using a custom-built gas separation set-up at atmospheric temperature (25 °C) and pressures from 1-5 Bar. The addition of the filler lead to improved permeability (582 % > PSF) and permeance (184 % > PSF) over the pure PSF membrane, at the cost of reduced H_2/CO_2 selectivity (68 % < PSF). Increasing the filler loading produced a parabolic effect, suggesting a cap on permeability enhancement at 4.246×10^{-11} $mol.m/m^2.s.Pa$ in the 10 wt. % membrane through the addition of silica sodalite. The results of this study demonstrate the enhanced separation potential of silica sodalite filled mixed matrix membranes for gaseous applications if defect free membranes can be fabricated.

Acknowledgements

Thank you to Air products South Africa for the funding of this research project and the Norwegian TCCs conference. A special thank you to my supervisor Michael Daramola for his continued criticism and support to make this project the best it could be.

A special mention to the SEERU research group for continuous assistance, encouragement and friendship, as well as to the laboratory management staff at the School of Chemical and Metallurgical engineering; J. Smith, M. Phali and B. Mothibedi.

Thank you all

Table of contents

Plagiarism declaration 1

Abstract 2

Acknowledgements 4

Table of contents 5

Journal articles and Conference proceedings 9

List of Figures 10

List of Tables 12

Nomenclature 13

Chapter 1: Introduction 14

1.1 Motivation 14

1.2 Problem statement 16

1.3 Research questions and objectives 17

1.3.1 Research questions 17

1.3.2 Research objectives 17

1.4 Research scope and contributions of the study 17

1.4.1 Scope of research 17

1.4.2 Contribution to research 18

1.5 Dissertation overview 18

Chapter 2: Background and Literature Review 19

2.1 Carbon dioxide emissions and environmental impacts 19

2.1.1 Sources of anthropogenic CO_2 emissions 19

2.1.2 Health and environmental impacts of CO_2 emissions 20

2.1.3 Methods of reducing CO_2 emissions 21

2.1.4 Technologies for CO_2 capture 22

2.2 Membrane based CO_2 capture 24

2.2.1 Types of membranes 24
2.2.2 Transport of gas in membranes 25
2.3 Mixed matrix membranes for CO_2/H_2 separation 30
2.3.1 Types of Mixed Matrix Membranes 30
2.3.2 Polymeric Membranes for Mixed Matrix Applications 35
2.3.3 Preparation and characterization of MMMs 39
2.4 Sodalite crystals as fillers in MMMs 42
2.4.1 Hydroxy sodalite and silica sodalite crystals 42
2.4.2 Synthesis and characterization of sodalite crystals 42
2.4.3 Factors affecting synthesis of high-quality silica sodalite 46
2.4.4 Sodalite crystals in membrane applications 46
2.5 Membrane properties and operating conditions 47
2.5.1 Thermal and Hydro-thermal Stability 47
2.5.2 Mechanical Strength 48
2.5.3 Operating Conditions 49
2.5.4 Economic Feasibility 49
2.6 Concluding remarks 50
Chapter 3: Methodology 51
3.1 Introduction 51
3.2 Equipment and devices 51
3.3 Synthesis of sodalite crystals and membrane fabrication 51
3.3.1 Silica sodalite 51
3.3.2 Hydroxy Sodalite 52
3.3.3 Mixed matrix membranes 52
3.4 Analysis and characterization 53
3.5 Model formulation and explanation 54
3.5.1 Preliminary Investigation 54
3.5.2 Extended Investigation 55
3.5.3 Regression model 58

3.5.4 Gas transport experiments 59
3.6 Ethics 60
3.7 Waste 60
3.8 Concluding remarks 60
Chapter 4: Development of silica sodalite with enhanced porosity via topotactic conversion 61
4.1 Introduction 61
4.2 Experimental 61
4.2.1 Synthesis and characterization 61
4.2.2 Investigating the effect of synthesis variables using response surface methodology (RSM) 62
4.3 Results and discussion 62
4.3.1 Analysis and characterization: preliminary and extended investigation 62
4.3.2 Effect of synthesis variables using RSM 72
4.3.3 Validation an analysis of optimized sodalite 85
4.4 Concluding remarks 93
Chapter 5: The fabrication of silica sodalite/polysulfone mixed matrix membranes and evaluation in H_2/CO_2 separation 95
5.1 Introduction 95
5.2 Experimental 95
5.2.1 Synthesis and characterization 95
5.2.2 Separation performance of fabricated membranes 95
5.3 Results and discussion 95
5.3.1 Membrane Morphology 95
5.3.2 Mechanical properties 100
5.3.3 Gas separation performance 103
5.4 Concluding remarks 107
Chapter 6: Conclusions and Recommendations 110
6.1 Conclusions 110
6.2 Recommendations 111

References I
Appendix A: Supplementary data and imaging XIII
A.1) Chapter 4 additional images XIII
A.2) Chapter 5 additional images XV
A.3) Chapter 7 additional data XVI
Table 18: Membrane thickness for single gas permeations XVI
A.4) RUB-15 Comparative XRD graphs from literature XXIV
Appendix B: Design expert data XXV
B.1) Preliminary Investigation XXV
Surface Area candidate models XXV
Pore Volume candidate models XXVII
B.2) Extended Investigation XXX
Surface Area model XXX
Pore Volume model XXXII
Optimization XXXV
Appendix C: Operating procedures XXXVI
C.1) Procedure for operating membrane gas separation system XXXVI
C.2) GC operating procedure XXXVIII
Appendix D: Copy right permissions XXXIX
D.1) Figure 1 XXXIX
D.2) Figure 2 XL
D.3) Figure A.4 XLII
Appendix E: Copy of first page of publications XLIV
Appendix F: Similarity Index Report XLVI

Journal articles and Conference proceedings

1. Eden, C; Daramola, M.O, 2019. Performance evaluation of fabricated nanocomposite silica sodalite infused polysulfone mixed matrix membranes for H_2/CO_2 separation, Materials Today Proceedings.
   (In Press, March 2020, DOI: 10.1016/j.matpr.2020.02.393).

2. Eden, C; Daramola, M.O, Ntombela, N, 2019. Development of silica sodalite with enhanced porosity via topotactic synthesis for pre-combustion CO_2 capture, In: SINTEF Proceedings of the 10th Trondheim Carbon Capture and Storage conference, pp.13-20, Published SINTEF Proceedings (ISSN 2387-4295, online; ISBN 978-82-536-1646-9, PDF).

3. Eden, C; Daramola, M.O, 2018. Synthesis and Evaluation of Silica Sodalite infused Polysulfone membranes for H2/CO2 separation, International Workshop on Porous Materials and their Applications (IWPMA-2018), 13 September 2018, Pretoria, South Africa (oral presentation).

List of Figures

Figure 1: Upper bound correlation for H_2/CO_2 separation (Robeson, 2008) 30
Figure 2: Sodalite framework (International Zeolite Association, 2007; Khajavi, et al., 2007) 42
Figure 3: Design space for preliminary investigation 55
Figure 4: Design space for extended investigation 56
Figure 5: BET surface rea and pore volume of SSOD relative to HSOD results 64
Figure 6: Surface area graph for extended investigation 65
Figure 7: Powder X-ray diffraction patterns for RUB-15 synthesized in a) the preliminary study and b) the extended investigation 66
Figure 8: XRD patterns for sodalite samples synthesized in the preliminary investigation 67
Figure 9: XRD pattern for a) simulated IZA standard; b) Preliminary investigation SSOD 2; c) SSOD 6; d) SSOD 9 68
Figure 10: SEM imaging for synthesized samples a) RUB-15; b) HSOD; c) SSOD1; d) SSOD2; e) SSOD3; f) SSOD8 69
Figure 11: SEM imaging of synthesized samples; a) RUB-15; b) SSOD6; c) SSOD 9 (20kX) and d) SSOD 9 (5kX) 70
Figure 12: FTIR absorbance spectrum (a.u.) for synthesized samples (preliminary investigation) 71
Figure 13: FTIR absorbance spectrum (a.u.) of synthesized sodalite (extended investigation) .. 72
Figure 14: a) Half-Normal and b) Pareto chart for PV model (factorial design) 73
Figure 15: a) Predicted vs. actual plot; b) residual vs. run plot (factorial design) 74
Figure 16: a) contour and b) response surface plot for acid strength (A) and calcination temperature (C) at B= 95 min 75
Figure 17: a) half-normal; b) Pareto plots for SA model 75
Figure 18: a) Predicted vs. run plot and b) Residual vs. run plot for SA model (factorial design) 76
Figure 19: a) Contour and b) response surface plot for acid strength (A) and calcination temperature (C) at B= 95 min 77
Figure 20: Model graphs a) Predicted vs actual results; b) 2D Contour plot of model terms A and C at B= 3h; c) 3D response surface for model terms A and C at B=3h 79
Figure 21: a) Predicted vs actual values; b) Normal plot of residuals 81
Figure 22: 2D contour plots and 3D response surfaces for model factors A, B and C (third factor not shown is at an intermediate level in each case) 83
Figure 23: Overlay plots for model factors; a) A&B, b) A&C and c) B&C at optimum conditions 85
Figure 24: 3D desirability responses for optimization of factors; a) A&B, b) A&C and c) B&C 85

Figure 25: a) SA and b) PV results for optimized SSOD 86
Figure 26: Adsorption isotherms for optimized SSOD 87
Figure 27: Adsorption isotherm for $SSOD_m$ 88
Figure 28: XRD patterns for a) simulated IZA standard; b) RUB-15 (MMM); c) SSOD m; d) OPT 1; e) OPT 2; f) OPT 3 89
Figure 29: SEM imaging for optimized SSOD; a)OPT1; b)OPT2; c)OPT3 and d)SSODm 90
Figure 30: FTIR absorption spectrum for optimized silica sodalite 91
Figure 31: TGA results for SSODm 92
Figure 32: Particle size distribution curve 93
Figure 33: SEM images of membranes surface for a) purely PSF; b)5wt. % HSOD/PSF ; c) 5wt. % SSOD/PSF MMM's (Mag =120 X) 96
Figure 34: SEM images of membranes surface for SSOD/PSF MMM a)5 wt. %; b)10 wt. %; c)15 wt. % (Mag=1.76 kX) under SE2 (left) and InLense (right) detection 97
Figure 35: Cross-sectional SEM images of a) 5 wt. % HSOD; b) 5wt % SSOD MMM's (Mag= 800 X) and c) surface layer of 5wt % SSOD MMM's (Mag= 8.21 kX) 99
Figure 36: Cross-sectional view of SEM images for SSOD/PSF MMMs at a) 5wt. %; b) 10wt. %; c) 15wt. % at magnifications of 2.21 kX (left) and 10 kX (right), respectively. 100
Figure 37: a) Young's Modulus and b) tensile strength for MMMs 102
Figure 38: TGA weight (solid) and derivative weight (dashed) graphs for polysulfone mixed matrix membranes 103
Figure 39: Effect of silica sodalite loading on membrane a) permeability and b) selectivity (1 Bar) 105
Figure 40: a) Robeson's H_2/CO_2 boundary and b) Effect of pressure on H_2 permeability 105
Figure 41: Effect of SSOD loading on a) permeance and b) relative permeability 107
Figure 42: Schematic diagram of membrane gas separation rig XXXVI

List of Tables

Table 1: Summary of sample preparation methods and results (Koike et al, 2017) 45
Table 2: Synthesis variables for factorial design 55
Table 3: Experimental design for factorial design 55
Table 4: Synthesis variables for BBH design 57
Table 5: BBH experimental design 57
Table 6: BET results for preliminary investigation 63
Table 7: BET results for extended investigation 64
Table 8: Analysis of variance for PV response (factorial design) 74
Table 9: Solutions for optimum design variables for preliminary investigation 77
Table 10: Model summary statistics for PV response 78
Table 11: Analysis of variance for PV response (BBH design) 79
Table 12: Model summary statistics for SA response 80
Table 13: Analysis of variance for SA response (BBH design) 81
Table 14: Solutions for optimum design variables for extended investigation 84
Table 15: BET results of optimized SSOD 86
Table 16: Single gas permeation results conducted at 1 Bar and 25°C 104
Table 17: Mixed gas permeation (60 H_2: 40 CO_2) results conducted at 1 Bar and 25°C 107
Table 18: Membrane thickness for single gas permeations XVI
Table 19: Robeson updated upper limit data (Appendix E.1) XVI
Table 20: H_2 single gas permeation results (averages of 4 membranes) XVII
Table 21: N_2 single gas permeation results (averages of 4 membranes) XVIII
Table 22: CO_2 single gas permeation results (averages of 4 membranes) XIX
Table 23: Mixed gas ($60H_2$:$40CO_2$) separation data XXI
Table 24: Mixed gas ($60H_2$:$40CO_2$) calculated results XXII

Nomenclature

Symbol/ Abbreviation	Definition
Al	Aluminium
CCS	Carbon capture and storage
CO_2	Carbon dioxide
H_2	Hydrogen
HSOD	Hydroxy sodalite
IGCC	Integrated gasification combined cycle
MMM	Mixed matrix membrane
N_2	Nitrogen
P	Permeability
PES	Polyethersulfone
ppm	Part per million
PSF	Polysulfone
RSM	Response surface methodology
SF	Separation factor
Si	Silicon
SSOD	Silica sodalite
α	Selectivity

Chapter 1: Introduction

This chapter deals with critical sections involved in any scientific research; the motivation for the study, the contribution to the body of scientific knowledge and the research specific questions and objectives. The scope of the study is also included in this chapter

1.1 Motivation

Anthropogenic carbon dioxide emissions are a significant factor contributing to global warming and ocean acidification. Atmospheric concentrations of CO_2 have risen from 280 ppm before the industrial revolution to 407 ppm in 2018, with expected increases up to 1500 ppm if carbon capture methods are not implemented (Pachauri et al, 2014; Leung et al, 2014; Lindsey, 2019).

The effective separation of CO_2 produced in industrial activities and power generation is vital. Recent occurrences such as; the energy crisis– which has resulted in the hyperinflation of energy costs (ONE Energy, 2017), the rapid depletion of fossil fuels and climate change (Earth Life Africa Johannesburg, 2009; Lindsey, 2019) have resulted in a push towards the high energy efficiency of industrial processes. Currently cryogenic distillation and pressure swing absorption form the universally accepted practice for large scale CO_2 separation from gas mixtures. These processes are simple, require low capital cost and have good reliability to produce high purity products but are highly energy intensive (Huang et al, 2010). To combat this, membranes have been intensively studied as an alternative technology for applications in gas separation.

Membranes for gas separation applications have generated much interest over the past decade. Such technologies are favoured over conventional gas separation methods as they have reported consistently high fluxes and selectivity, low energy requirements and maintenance, low cost and easy operation with minimal labour intensity (Basu et al, 2004). However, traditional technologies are still favoured for their higher purity. Subsequently, membranes designed to purify hydrogen from carbon dioxide and carbon monoxide need to be thermally and mechanically stable with good separation performance to make them an economically attractive alternative.

Most industrial membrane systems utilize polymeric membranes over non-polymeric and ceramic membranes due to their good processing feasibility, mechanical strength and inexpensive nature (Nunes & Peinemann, 2001; Baker, 1991; Wang & Hong, 2005). However, these membranes are known to have poor thermal stability and a trade-off between permeability and selectivity, limiting their separation potential following the Robeson plot

(Robeson, 1991; 2008). For this reason, much research has gone into the development of mixed matrix membranes (MMMs). MMMs combine polymers with inorganic molecular sieves or zeolites to increase membrane permeability while maintaining the selectivity in the hope to transcend the Robeson upper boundary.

Glassy polymers have strong size-sieving abilities producing high selectivity. Polysulfone (PSF) is widely used glassy polymer in membrane preparations that can be easily fabricated on a large scale and display excellent mechanical, thermal and oxidative stability necessary for industrial applications (Madaeni & Moradi, 2011). PSF has been intensively investigated for both pure gas permeations and mixed gas separations but possess poor transport properties, making enhancement of polysulfone through inorganic fillers highly favourable (Ahn et al., 2008). The combination of zeolite and polymer membranes results in improved separation performance, making them industrially attractive if synthesis can be made feasible (Chakraborty et al, 2016).

Mixed matrix membranes (MMMs), with fillers dispersed within polymer matrices, are commonly used in gas separation applications. For instance, polymer filled with sodalite particles could be applied in the separation of hydrogen from a gas mixture containing H_2, CO, and CO_2, usual products in IGCC power generation from fossil-fuels (Kim et al, 2007). Pre-combustion carbon capture is favourable over post-combustion methods due to the higher CO_2 concentration (> 20 %) within the gas resulting in a high removal efficiency (Leung et al, 2014).

Hydroxy Sodalite (HSOD) is a common zeolite with a cage structure with pores of approximately 2.6 Å free diameters (Breck, 1974). The cage structure allows the permeation of small molecules such as helium (2.60 Å (Matteucci et al, 2006)) hydrogen (2.89 Å (Ismail et al, 2015)) and ammonia (2.60 Å (Breck, 1974)), which have molecular sizes similar to the average cage dimension of the zeolite. However, the trapped guest species such as organic matter, water and anions within the cage of the sodalite hinder the permeation of the gases (Breck, 1974). Removing these occluded materials from the cage via dehydration or calcination at high temperature (> 400 °C) collapses the cage and thus renders the sodalite useless (Khajavi et al, 2010; Daramola et al, 2015). Therefore, it is imperative to develop a technique to produce sodalite without the presence of occluded matter without collapsing the sodalite cage structure.

1.2 Problem statement

Most membranes used industrially are purely polymeric but in order for membrane systems to compete with adsorption and distillation systems, the separation performance in atmospheric gas applications needs to be improved. While feasibility studies have shown good potential for membrane separation, this often comes at the expense of reduced purity (Hinchliffe & Porter, 2000; Moparthi, et al., 2010). Despite the long list of advantages associated with membrane separation, the higher purities produced through distillation are still preferable over lower energy penalties. Mixed matrix polymer membranes filled with inorganic molecular sieves have the potential to replace commercial distillation should high permeability, high selectivity membranes become available on an industrial scale. This would enable a system with ideal separation, with reduced cost and environmental impact (Hinchliffe & Porter, 2000).

Hydroxy sodalite is a zeolite with excellent potential in catalysis, separation and adsorption applications. HSOD is widely produced through hydrothermal synthesis which prevents the effective use of the sodalite micro pores due to the presence of occluded molecules within the sodalite cages. Attempts to remove the occluded matter through dehydration have resulted in the structural collapse of the sodalite cages preventing their use in separation applications (Moteki et al, 2011). Topotactic conversion has the potential to produce zeolite structures with new unique chemical compositions and morphologies. However, limited research has been done on using this method for the production of silica sodalite (SSOD) and the methodology proposed by Moteki et al. (2008) and modified by Koike et al. (2017) reported a few inconsistencies around the quality of SSOD produced.

Furthermore, limited experimentation has been conducted and reported on the fabrication and application of mixed matrix membranes for H_2/CO_2 separation, with those tested failing to improve the separation performance beyond Robeson's upper boundary, thus limiting their industrial application. In particular, reports on the fabrication and application of SSOD infused MMMs for gas separation are very limited. SSOD/polymer membranes have the potential for improved gas separation performance due to the enhanced porosity of the SSOD crystals and its high thermal and oxidative stability (Ahn et al, 2008).

1.3 Research questions and objectives

1.3.1 Research questions

1. What are the optimal topotactic conversion operating conditions to synthesize high porosity silica sodalite?
2. Would the use of the silica sodalite produced in (1) as a filler in polysulfone membranes improve the separation performance of the membrane for H_2/CO_2 separation?
3. What is the effect of varying the SSOD loading on the performance of the mixed matrix membranes produced in (2)?

1.3.2 Research objectives

1. To synthesize silica sodalite via topotactic conversion and investigate the effect of synthesis parameters such as the strength and treatment time of organic acid, as well as the calcination temperature on the textural and morphological quality of silica sodalite.
2. To use the optimized SSOD produced in (1) to fabricate SSOD/PSF membranes and evaluate the performance of the membrane for H_2/CO_2 separation.
3. To investigate the effects of SSOD loading on SSOD/PSF membranes on the separation performance of H_2/CO_2.

1.4 Research scope and contributions of the study

1.4.1 Scope of research

This study was limited to investigating the effect of key synthesis variables; such as propionic acid strength, acid treatment time, calcination time and temperature in the topotactic conversion of RUB-15 to silica sodalite. No variables relating to the synthesis of RUB-15 were tested or other second-stage synthesis factors such as the ratio of RUB-15 to propionic acid or acid type were tested. Hydroxy sodalite was synthesized following a standard hydrothermal synthesis method for comparison. Membranes were synthesized utilizing SSOD particles formed after the investigation of synthesis variables. Various SSOD loadings were used in the membranes and fabrication was done using wet phase inversion. These membranes were used to separate hydrogen from carbon dioxide only. No fabrication procedures were investigated. The fabricated membranes were tested in separating hydrogen from carbon dioxide using pure components of the gases and a mixture of the gases in the ratio, 40:60 (H_2/CO_2). The effects of other contaminants such as SO_2 and CO, etc. were not considered in this study. Separation

performance was conducted at ambient temperature (ranging from 23-25 °C) and low pressures from 1-5 bar only.

1.4.2 Contribution to research

This research aimed to improve the current topotactic conversion process to produce high porosity SSOD crystals and a reproducible synthesis method. Past research has produced inconsistent qualities of SSOD with multiple discrepancies between various researchers. An optimized procedure would enable the formation of a high quality SSOD for use in catalysis, adsorption and separation applications. A better depiction of the relationship between the operating variables and SSOD quality may also guide future research into the use of this method for the formation of other zeolite materials.

As a filler silica sodalite is expected to offer molecular sieving abilities to improve the performance of the PSF membrane for gas separation. A MMM with the potential to effectively separate hydrogen from carbon dioxide opens the door to future research into such membranes for industrial application. Research is continually focused at exceeding Robeson's upper boundary but very few membranes have successfully achieved this. Limited literature is available for membranes utilizing these specific materials, with those previously reported for low-quality silica sodalite failing to improve the gas separation performance or test their application in H_2/CO_2 separations.

1.5 Dissertation overview

Chapter 2 provides background on the problem of carbon dioxide and the cause and means to separate it. It highlights current research in zeolite synthesis and membrane fabrication and as well as membrane gas separation. Chapter 3 reports the methodology followed in this study, making note of chemicals, instrumentation and procedures followed. Chapter 4 investigates the effect of topotactic conversion variables on the SSOD surface area and pore volume by investigating; acid strength, acid treatment time and calcination time and temperature. It consists of the characterization of textural and physio-chemical properties of the sodalite crystals, the modeling and optimization of synthesis variables and the validation of these models for both the preliminary and extended investigations. Chapter 5 investigates the membranes separation performance of the sodalite polysulfone mixed matrix membranes. The study is concluded in Chapter 6 with the main conclusions and recommendations for future research.

Chapter 2: Background and Literature Review

2.1 Carbon dioxide emissions and environmental impacts

2.1.1 Sources of anthropogenic CO_2 emissions

Economic growth over the last few decades has seen an increase in energy consumption of 39 % worldwide from 1990-2008, with an increased consumption of 70 % for the African continent. Urbanization and industrialization play a major role in the high energy consumption of developing countries, this is often accompanied by a rapid increase in CO_2 emissions, fossil fuel consumption and environmental degradation (Mrabet et al, 2019). In order to produce a sustainable pathway for both economic growth and environmental sustainability, energy efficiency has been emphasised as a useful tool to ensuring environmentally sensitive energy production. Mrabet et al. (2019) concluded that a 1 % rise in urbanization equated to a 0.72 % increase in non-renewable energy consumption for developing countries, such as South Africa.

Urbanization and industrialization are expected to rapidly increase over the coming years; it is predicted by Sadorsky (2013) that by 2020 the urbanization of less developed countries will reach the 50 % marker. Sadorsky concluded that increasing income positively reduced the energy intensity of developing countries while increasing industrialization has a negative effect. The increase of economic activity due to increased consumption and production with increased urbanization leads to increased energy intensity but also provides opportunities for increased energy efficiency. Reductions in the energy intensity of industrial and commercial operations are encouraged as a way to partially reduce the concerns of climate change, the depletion of fossil fuels and energy security (Sadorsky, 2013).

Global energy consumption and emissions are expected to increase with increasing urbanization and global industrialization. The adoption of cost-effective energy efficiency measures in addition to new environmental policies following the IEA efficient world scenario (EWS) and new policies scenario (NPS) has the potential to reduce energy usage and anthropogenic emissions. The implementation of these policies was projected to reduce emissions by 10 % compared to current levels and result in 40 % abatement, in line with the Paris targets required by 2040. Following these scenarios, significant reductions in CO_2 emissions are possible with the implementation of high energy efficiency despite a 20 % population increase and a 60 % increase in building space (Lane, 2018).

The majority of the world's energy production currently originates from fossil fuels; natural gas (24 %), oil (36 %) and coal (28 %) (International Energy Agency, 2015). Natural Gas Combined

Cycles (NGCC) and Integrated Gasification Combined Cycles (IGCC) form important processes for energy production. Coal and natural gas are converted to hydrogen and carbon monoxide through steam reforming (Equation 1), partial oxidation or gasification (Equation 2). These products are then converted to hydrogen and carbon dioxide (a desirable alternative to carbon monoxide) via the water-gas shift reaction (Equation 3) (Jansen et al, 2015). In-order to use this hydrogen in combined-cycle plants, the carbon dioxide needs to be removed. Carbon dioxide not only lowers the heating value, thus decreasing the efficiency of the fuel but releases anthropogenic CO_2 into the environment after combustion.

$$C_xH_y + xH_2O \leftrightarrow xCO + \left(x + \frac{y}{2}\right)H_2 \qquad \Delta H = 206\ kJ/mol \qquad \text{Equation 1}$$

$$C_xH_y + \frac{x}{2}O_2 \leftrightarrow xCO + \left(x + \frac{y}{2}\right)H_2 \qquad \Delta H = -36\ kJ/mol \qquad \text{Equation 2}$$

$$CO + H_2O \leftrightarrow CO_2 + H_2 \qquad \Delta H = -41 kJ/mol \qquad \text{Equation 3}$$

2.1.2 Health and environmental impacts of CO_2 emissions

The continuous accumulation of CO_2 within the atmosphere has resulted in the accelerated effect of global warming. CO_2 concentrations have risen from 280 to 407 ppm accompanying an 0.8 ℃ increase in global temperatures (Pachauri et al, 2014; Lindsey, 2019) with predicted concentrations of 600 to 1550 ppm in 2030 without the use of climate change mitigation (Leung et al, 2014) . While 85.9 % of these emissions are attributed to the industrialization of developed countries, these emissions have reached a peak (Grubler & Fujii, 1991). Increasing urbanization and industrialization of developing countries is expected to generate the majority of the world's future carbon emissions (World Bank group, 2010). Dong et al. (2019) found that urbanization and income level had a double-threshold effect on CO_2 emissions, at low stages of urbanization no correlation was seen but increased urbanization levels promoted an increase in CO_2 emissions (Dong et al, 2019).

Global temperatures have risen by 0.87 ℃ (2006-2015) relative to pre-industrial levels (1850-1900) and this change has been accompanied by more frequent extreme heatwaves in the majority of land regions as well as more frequent and longer durations of marine heatwaves. In addition human-induced global warming has seen an increase in the frequency and intensity of precipitation on a global scale and increased drought periods in Mediterranean regions. In general extreme weather conditions have occurred at increasing frequency for increasing durations. Changes to phenology, shifts in fauna and flora and increased tree mortality reduce the functioning of ecosystems, biodiversity and impact human populations. Changing patterns of diseases and invasive species were also reported, with risks to human populations due to sea level rise (IPCC, 2018).

Limiting the global increase to 1.5 °C as opposed to 2 °C would prevent 420 million people from being exposed to frequent extreme heatwaves. Increasing global temperatures past the 1.5 °C limit is predicted, with high confidence, to further exacerbate the frequency and intensity of extreme climate conditions. Natural and human systems face the risk of long-lasting and irreversible impacts, such as the loss of ecosystems and biodiversity, leading to reduced economic activities and poverty (Nagelkerken & Connell, 2015). Lower risk is associated with the 1.5 °C as opposed to 2 °C increase due to a slower rate of change, enhancing the ability for natural and systems to adapt. This benefits all land and marine ecosystems as well as human food production, health, tourism, energy and transportation systems. A 2 °C rise in temperature increases the risks to crop yields, energy and water security that may overlap to escalate the portion of people exposed and susceptible to poverty (IPCC, 2018).

2.1.3 Methods of reducing CO_2 emissions

Legislation and carbon capping strategies are an effective method to reduce carbon emissions. This limits the maximum CO_2 emissions by large-scale emitters and organizations through the purchase of permits. The permits set an enforceable maximum cap on the amount of anthropogenic CO_2 released into the atmosphere. Permits become stricter on renewal until the reduction goal is met. Such a plan has been implemented by the United States of America (Carbon Cap-and-Trade Plan) following the successful implementation of the Clean Air Act 1990 which successfully reduced sulphur emissions at lower costs to industry than expected (Evans, 2019).

Carbon tax is noted as “the most efficient market-based mitigation instrument” (Lin & Li, 2011). The estimate and analysis of real mitigation impacts of north European countries such as Denmark, Finland, Sweden, Netherlands and Norway were conducted. Carbon tax was found to have a negative impact on the increase of per capita CO_2 emissions however; mitigation effects were limited by the tax exemption of a number of energy intensive industries. High tax rates and the recycling of revenue back into mitigation were concluded to contribute to reduced emissions (Lin & Li, 2011).

As power generation forms one of the largest emitters of anthropogenic CO_2, switching to the use of clean fuels and reducing electricity demand through the high energy efficiency of industrial processes are important methods required for the reduction of CO_2 emissions (Lane, 2018; IEA, 2019). Carbon offsetting through projects such as reforestation and the development of solar/wind power stations, aid in the reduction of an organization’s carbon footprint.

Carbon sequestration through capture and storage was identified as the best means of remediation to reach the IPCC's goal of limiting the global temperature increase to 1.5 °C above pre-industrial levels. This can occur naturally though biological, chemical and physical processes such as photosynthesis, chemical weathering and dissolution of CO_2 into the oceans. Synthetic processes are also available, using different technologies to capture CO_2 from point source emitters and store it in underground reservoirs. CCS would need to form a significant part of mitigation options and operate on a large scale to achieve carbon neutrality and ultimately carbon negativity. The implementation of CCS is currently limited by high capital costs and negative perceptions (Wennersten et al, 2015)

2.1.4 Technologies for CO_2 capture

Carbon capture and storage methods fall into three main categories: pre-combustion, post-combustion and oxy-fuel combustion capture (Anwar et al, 2018).

Pre-combustion capture involves reacting a fuel with oxygen or air and/or steam to give a 'synthesis gas (syngas) ' or 'fuel gas' compose mainly of carbon monoxide and hydrogen. The carbon monoxide is further reacted with steam via the water-gas shift reaction in a catalytic reactor to give CO_2 and hydrogen. CO_2 is then separated, usually by a physical or chemical absorption process, resulting in a hydrogen-rich fuel which can be used in many applications. Boilers, furnaces, gas turbines, engines and fuel cells all make use of high purity H_2. Pre-combustion capture is favoured due to the ease of the process and high efficiency due to the high concentration of CO_2 (>20%). This process is easily applied to IGCC power plants utilizing coal (such as in Southern Africa), at an efficiency loss of approximately 8% (Leung et al, 2014).

Post-combustion capture involves the capture of CO_2 from flue gas streams after combustion through the use of adsorption systems such as amine solutions. These processes are disadvantaged by the low CO_2 concentration but are mature technologies that are easily retrofitted to existing power plants (Leung et al, 2014).

Oxy-fuel combustion is usually applied to coal-gasification plants and replaces the air in the combustion stage with pure oxygen which reduced the nitrogen concentration in the exhaust gas. Carbon dioxide thus forms the main product improving adsorption efficiency, the smaller volume of gas processed reduces the capital costs of equipment. However, this process is disadvantaged by a large efficiency loss, corrosion and energy penalties (Leung et al, 2014).

Many technologies have been developed for the separation of CO_2 from other flue gasses; the main methods include absorption, adsorption and cryogenic distillation.

2.1.4.1 Absorption

In absorption systems the flue gas is passed through a liquid solvent where the CO_2 is removed by attraction to the solvent via van der Waals and electrostatic forces. This is done at low temperature and high operating pressures. The CO_2 is then stripped at high temperature, low pressure and the solvent is recycled to the feed (Anwar, et al., 2018). Monoethanolamine (MEA), diethanolamine (DEA) and potassium carbonate are common sorbents for CO_2 capture. This process yields a high efficiency above 90 % and is well understood but utilizes large amounts of energy for solvent regeneration and the environmental impact of amine absorbents and their degradation products is unfavorable (Leung et al, 2014; Gouedard et al, 2012).

2.1.4.2 Adsorption

Physical adsorption involves the use of solid catalyst particles such as zeolites in packed beds which form surface attractions with the CO_2 molecules. High efficiencies can be achieved and the adsorbents can be recycled. The CO_2 is recovered via pressure or temperature swing processes at the cost of high energy requirements. Other limitations include the loss of material during operation, mass transfer resistance and pressure drop (Anwar et al, 2018).

2.1.4.3 Cryogenic distillation

CO_2 can be separated from other gases through condensation on the basis of dew and sublimation points. Despite the good separation achieved, this process is highly energy intensive due to the low temperature (-100 to -135 °C) and high pressure (100- 200 atm) required to liquefy the CO_2 (Anwar et al, 2018). Current technologies utilizing cryogenic distillation for CO_2 capture liquefy the CO_2 at ambient temperatures and high pressure with reductions in the traditional water consumption, chemical usage and related corrosion problems (Pires et al, 2011).

2.1.4.4 Chemical looping

During the combustion process, metals are added to the oxygen rich stream, the metals react to form metal oxides which are fed to the combustion reactor. The oxides form the oxygen carrier which is then combusted with the fuel to form only CO_2 and water. This enables easy sequestration of CO_2 after the condensation of the water. The metal oxide can then be regenerated through reaction with air (Leung et al, 2014; Oloye & Daramola, 2017). This process is advantageous due to the inexpensive nature of the metal additives as well as the minimal production of nitrogen oxides that results(Anthony, 2010).

2.1.4.5 Membrane technologies

Membranes technologies form an alternative to the traditional processes of adsorption and cryogenic distillation. The membranes employed industrially are mostly polymeric, combining a

thin selective layer with a thicker non-selective layer for mechanical support. Membranes comprising of a host of materials (ceramic, metallic and polymeric) have been investigated for gas separation applications. The separation performance of these membranes was found to be linked to flue gas concentrations and system pressure and temperatures (Leung et al, 2014). There is a large potential in this area due to the low cost, ease of fabrication and strong mechanical strength of membranes but separation performance still needs to be improved to compete with traditional technologies (Basu et al, 2004; Pires et al, 2011).

2.2 Membrane based CO_2 capture

Membranes for gas separation applications have generated much interest over the past decade. Such technologies have reported consistently high fluxes and selectivity, low energy requirements and maintenance, low cost and easy operation with minimal labour intensity (Basu et al, 2004).

2.2.1 Types of membranes

Polymeric, inorganic and ceramic membranes are the most common in membrane separation. Inorganic membranes such as zeolites, alumina and carbon possess excellent separation performance, chemical and thermal stability over polymer membranes but are disadvantages by high fabrication costs and poor mechanical strength. Ceramic membranes show good chemical and thermal stability, desirable selectivity and high permeability but are undesirable for industrial applications due to their high cost and highly brittle nature (Nunes & Peinemann, 2001; Baker, 1991; Wang & Hong, 2005).

The majority of industrial membrane systems utilize polymeric membranes due to processing feasibility and cost. However, these membranes are known to have a trade-off between permeability and selectivity, limiting their separation potential following the Robeson plot. (Robeson, 1991) For this reason much research has gone into the development of mixed matrix membranes (MMMs) which combine polymers with inorganic molecular sieves or zeolites in an attempt to transcend the Robeson upper boundary.

MMMs are commonly used in gas applications for the separation of hydrogen molecules from CO and CO_2 such as in pre-combustion processes, coal gasification, water-gas shift reactions and hydrogen purification (Kim et al, 2007) and so need to produce effective separation at high temperatures and pressures and show good mechanical strength.

2.2.2 Transport of gas in membranes

Four gas transport mechanisms are commonly cited for diffusion within polymer and mixed matrix membranes; molecular sieving, Knudsen diffusion, molecular diffusion and viscous flow (Hashemifard et al, 2011). The gas molecular size and physical properties such as condensability influence the permeability and selectivity of gas species (Basu et al, 2004).

2.2.2.1 Pure Gas Permeations

Gas permeation through a membrane is a function of the membranes chemical and physical properties, the properties (shape, size and polarity) of the permeant gas as well as the interaction between the membrane and the permeant (Bastani et al, 2013). From this the permeability can be derived as a product of the gas solubility and diffusivity (Equation 4).

The permeability (P) of single gas diffusion through a membrane can be calculated by Equation 6. Where the derivative of the gas volume through the membrane (Vi) (Hashemifard et al, 2011) can be equated to the volume of gas though the membrane (Q) assuming steady state (Basu et al, 2004), l is the membrane thickness, A the membrane surface area and Δp the trans-membrane pressure drop, accounting for temperature deviations, T.

$$P_a = S_a D_a \qquad \text{Equation 4}$$

$$P = \frac{l}{A \Delta p} \frac{dVi}{dt} \frac{273.15}{T} \qquad \text{Equation 5}$$

$$P = \frac{l Q}{A \Delta p} \frac{273.15}{T} \qquad \text{Equation 6}$$

The ideal selectivity (α) of one pure gas (a) to the other (b) can be determined by the ration of the permeability of the two gasses (Equation 7) (Basu et al, 2004; Hashemifard et al, 2011).

$$\alpha_{a/b} = \frac{P_a}{P_b} \qquad \text{Equation 7}$$

2.2.2.2 Mixed gas separation

The permeability of mixed gas separation is similar to that of Equation 6 but considers the mole fractions of the components (x) in the feed and the permeate (Basu et al, 2004).

$$Pa = \frac{X_{perm}\, l\, Q}{A\,(p_{feed}\, X_{feed} - p_{\,perm}\, X_{perm})} \qquad \text{Equation 8}$$

The real selectivity of the mixed gas follows the same equation as Equation 7, substituting in Equation 8 this reduces to

$$\alpha_{a/b} = \frac{X_{perm,a}\,(p_{feed}\,X_{feed} - p_{perm}\,X_{perm})b}{X_{perm,b}\,(p_{feed}\,X_{feed} - p_{perm}\,X_{perm})a}$$ Equation 9

Permeability is usually referred to in Barrer (1×10^{-10} cm^3 (STP).cm/cm^2.cmHg.s) but can also be expressed in SI values (1 Barrer = 3.35×10^{-16} mol.m/m^2.s.Pa).

2.2.2.3 Transport Properties in Mixed Matrix Membranes

The basic permeability equation (Equation 5) applies to non-concentration dependant Fickian diffusion and relates the permeability to the diffusion coefficient (D) and the solubility coefficient (S). The solubility coefficient follows Henry's Law for most common gasses but dual mode sorption is observed for strongly polar gas pairs such as CO_2 and CH_4.

The transport mechanism is dependent on the filler pore size. Molecular sieving dominates at filler pore sizes below 5 Å. The Knudsen number (K_n) is based on the ratio of gas mean free path (λ) to the filler pore size (d) (Equation 10) (Hashemifard et al, 2011).

$$K_n = \frac{\lambda}{d}$$ Equation 10

$$\lambda = \frac{1.38\times10^{-23}\,T}{\sqrt{2}\pi\sigma^2 p}$$ Equation 11

T is the absolute temperature (K), 1.38 X 10^{-23} the Boltzmann constant (J/K), σ molecular size (m) and p the average pressure (Pa). If the pore size is very small and Kn $\geq$ 10 Knudsen diffusion results, if Kn $\leq$ 0.1 molecular diffusion dominates the transport mechanism and if $0.1 \leq Kn \leq 10$ then the diffusion lies within the transition regime (Karger & Ruthven, 1992; Karniadakis et al, 2005).

The molecular diffusion coefficient (D_m) can be calculated following the Chapman and Cowling equation (Equation 13) (Karger & Ruthven, 1992). The number density, n ($1/m^3$) can be calculated by Equation 14.

$$D_m = \frac{3}{8\,\sigma^2 n}\sqrt{\frac{1.38\times10^{-23}\,T}{m\,\pi}}$$ Equation 12

$$n = \frac{6.02\times10^{26}\,\rho g}{Mw}$$ Equation 13

The Knudsen diffusion coefficient (D_k) is calculated following Equation 14 and that of the transition regime (D_{mix}) following Equation 16.

$$D_k = \frac{97\,d}{2}\sqrt{\frac{T}{M_w}} \qquad \text{Equation 14}$$

$$\frac{1}{D\,mix} = \frac{1}{Dm} + \frac{1}{Dk} \qquad \text{Equation 15}$$

If a significant difference exists between the beginning and end of the permeation experiment, viscous flow predominates. The Poiseuille diffusion coefficient (Dp) an be calculated by Equation 16.

$$\mathrm{Dp} = \frac{\mathrm{d}^2}{32\,\mu}\,(\mathrm{p}_o - \mathrm{p}_l) \qquad \text{Equation 16}$$

P represents the upstream (subscript o) and downstream (subscript l) pressures and μ the gas viscosity (Pa.s) (Hashemifard et al, 2011).

Maxwell Model

The Maxwell model predicts the separation performance for dilute suspensions of spherical particles in a polymer membrane (Equation 17).

$$P_{eff} = P_c\left(\frac{Pd+2\,Pc-2\,\phi_d(\,Pc-Pd)}{Pd+2\,Pc+\,\phi_d(\,Pc-Pd)}\right) \qquad \text{Equation 17}$$

P_{eff} is the composite membrane effective permeability, ϕ the volume fraction and P the component permeability of the dispersed (d, zeolite and polymer) and continuous (c, pure polymer) phases.

Modified Equations

The Maxwell model represents the ideal case with the absence of defects and distortion. In order to better predict these systems, a three-phase model proposed by Mahajan et al. utilizing a molecular sieve phase, a polymer phase and interfacial voids (Mahajan et al, 2002). Mahajan suggested a modified Knudsen diffusion through the voids following Equation 18.

$$D_{AK} = 9.7 \times 10^{-5}\, r\sqrt{\frac{T}{M_A}}\,\left(1 - \frac{dg}{2\,r}\right) \qquad \text{Equation 18}$$

$$S = \frac{1}{RT}\left(1 - \frac{dg}{2r}\right)^2 \qquad \text{Equation 19}$$

D_{AK} represents the diffusion coefficient, r the pore effective radius (Å), the absolute temperature T, the molecular weight M_A and the diameter of the gas molecule d_g (Å). Mahajan assumes that the solution coefficient (S) in the voids is the same as in the gas phase and takes into account the size of the gas molecule. Maxwell's equation was revised and applied twice to incorporate the interfacial voids (subscript i).

$$P_{eff} = P_i \left(\frac{Pd+2\,Pi-2\,\phi_d(Pi-Pd)}{Pd+2\,Pi+\phi_d(Pi-Pd)} \right)$$ Equation 20

$$\phi s = \frac{\phi d}{\phi d+\phi i}$$ Equation 21

$$P_{3MM} = P_c \left(\frac{P_{eff}+2\,Pc-2(\phi_d+\phi_i)(Pc-P_{eff})}{P_{eff}+2\,Pc+(\phi_d+\phi_i)(Pc-P_{eff})} \right)$$ Equation 22

P_{eff} represents the combined permeability of the dispersed and void phases, ϕ the void fractions of the relative phases and P_{3MM} the permeability of the 3 phase membrane. This method can be implemented if the volume fraction and permeability of the voids can be estimated (Chunga et al, 2007).

Singh et al. developed empirical calculations to represent single-component permeations within mixed matric membranes (Singh et al, 2013). While the Maxwell model is believe to predict permeations reasonably accurately, the model fails to effectively predict permeations in real MMM who's interface equilibrium constants are usually greater of less than one. The assumption that the permeability ratio sufficiently defines the membranes permeability is thus flawed as both the diffusivity ratio and interface equilibrium constant have a large effect on the resulting permeability. When the gas specie is poorly absorbed, despite rapid diffusion through the filler regions of $D_{eff}/D_m < 1$ exist for permeability ratios $P_f/P_m > 1$. The opposite was also fond o be true of strongly absorbed species with slow diffusion. Such anomalies are often attributed to defects within the membrane but Singh believes these arrive from local depletions or increases in the concentration driving force within the MMM. Plots of D_{eff}/D_m, K and P_f/P_m revealed plateaus and valleys at high and very low values, respectively of D_{eff}/D_m and K. This lead to the formation of a generalized logistic function based on 10 parameters. This model was to be used in combination with adsorption and diffusion data for the respective filler and membrane phases. Ranges for the three independent variables were determined and were solved through nonlinear regression to ensure the convergence of a global minimum. This model was hen tested on a number of MMM with varying volume fractions of filler particles. No direct effects of the filler particle size were observed, dependence evident in other works was believed to be due to indirect effects of particle size such as enhanced interfacial interactions (Singh et al, 2013).

2.2.2.4 Robeson Upper boundary

Robeson's upper boundary exists as a gas separation limitation for polymeric membranes. A trade-off between permeability and selectivity is made with the separation of many binary mixtures being unable to surpass the boundary limit.

In 1991 Robeson analysed over 300 literatures sources and plotted the experimental results for binary gas mixtures of O_2, N_2, H_2, CO_2, CH_4 and He. Robeson found that a log-log plot of the selectivity versus the permeability of the more permeable gas yielded a linear upper boundary which none of the membranes were able to transcend, with the exception of a few experimental points. The slope of the upper bound (n) was found to be linked to the difference in molecular diameter of the gasses (Δd- Lennard-Jones kinetic diameter). The plot of -1/n versus Δd_{ab} yields a linear relationship (Robeson, 1991).

The following relationship was produced to relate permeability (P) to selectivity (α), utilizing a front factor (k).

$$P = k \ \propto_{a/b}{}^{n} \qquad \text{Equation 23}$$

Robeson extended his initial investigation in 2008 to encompass a wider range of data based on newer membrane technologies as well as include more binary mixtures (Robeson, 2008). Robeson reported a large shift in a few of the upper bound relations which he attributed to the use of perfluorinated polymer membranes, smaller shifts were seen in rigid glassy polymers or ladder structured polymers. Upper bound data for H_2/CO_2 mixtures produced k and n values of 1 200 and - 1.9363 respectively. More recent works site these values as 4 515 and -2.302 (Robeson et al, 1994). Changes in the slope were thought to be due to the use of poly(trimethylsilylpropene) data at higher permeability which may have skewed the resulting correlation (Robeson, 2008). Figure 1 represents the prior and adjusted upper bounds. The upper boundary was found to shift vertically with increasing temperature due to the size and condensability of gas molecules (Rezakazemi et al, 2014).

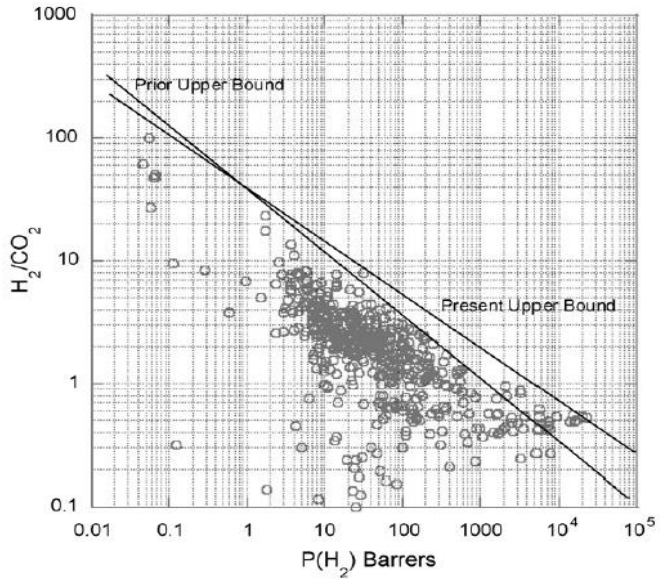


Figure 1: Upper bound correlation for H_2/CO_2 separation (Robeson, 2008)

Copy right permission attained from Elsevier as per Appendix D.1

2.3 Mixed matrix membranes for CO_2/H_2 separation

2.3.1 Types of Mixed Matrix Membranes

This research will focus on solid-polymer mixed matrix membranes for gas separation applications. Liquid/polymer membranes can be fabricated but experience high rates of washout and carrier evaporation leading to poor long-term stability. Solid-liquid-polymer combination are utilized to combat some of the problems associated with liquid-polymer systems but will not be further discussed in this paper.

The most common types of solid-polymer membranes include metal organic frameworks (MOFs), Zeolite imidazolate frameworks (ZIFs), Mesoporous silica spheres (MSSs) and layered sheet-like zeolites.

MOFs are a mixture of organic and inorganic porous materials which are modified by attaching metal complexes to the framework structure with organic linkers. These structures allow tuneable pore geometries, flexible frameworks and large surface areas. ZIFs are a zeolite subclass of MOFs with higher thermal, hydro-thermal and chemical stability than their parent species. ZIFs are formed by using functionalized imidazole linkers to connect Co and Zn groups to produce membranes with small pore diameters and zeolite structures. MSSs form some of the best-known filler materials due to their attractive pore structures, excellent separation performance and ideal polymer compatibility. Nanoporous titanosilicates have the structures of zeolites, forming three dimensional frameworks with interspaced cavities and connected

channels. They also contain a variety of metals forming polyhedral. These layered sheet materials have a higher surface area and the potential of exchanging charge-equalizing ions (Rezakazemi et al, 2014).

Several types of membranes have been evaluated for use in hydrogen and carbon dioxide separation applications. Most notably, Palladium-infused metallic membranes, carbon molecular sieve (CMS) membranes, doped and microporous amorphous silica membranes as well as zeolites.

While palladium based membranes have theoretically infinite H_2 selectivity and desirable permeability at temperatures exceeding 500 °C, they suffer from rapid degradation in the presence of CO and H_2S making them undesirable for industrial applications. CMS membranes are disadvantaged by poor mechanical strength resulting in fragile, brittle membranes and difficulties in fabricating thin films. Amorphous silica membranes have also shown outstanding H_2 selectivity with small molecule gasses at the expense of poor hydro-thermal stability. Other potential membrane containing siliceous microporous zeolites boast good thermal and chemical stability but have poor H_2/CO_2 separation due to zeolitic pores greater than 0.289 and 0.33 nm, the kinetic diameters of H_2 and CO_2 respectively (Li et al, 2010).

2.3.1.1 ZIF based membranes

Zeolitic imidazolate framework membranes form 3D tetrahedral frameworks with large interconnected sodalite cages which closely resemble zeolite structures. These membranes have pore apertures between 0.2 to 1.5 nm and demonstrate excellent thermal, hydro-thermal and chemical stability (Li et al, 2010).

Melgar et al, reviewed zeolitic imidazolate framework (ZIF) based membranes for gas separation applications. ZIF structures form molecular sieves and thus should be chosen based on pore aperture size. Knudsen diffusion was noted as the primary transport mechanism inside the membranes. In order to be desirable for industrial applications the gas separation performance should be greater than the Knudsen selectivity (KS= 4 for H_2/CO_2). Membranes were found to have suitable separation performance for incondensable inorganic gas systems such as binary mixtures of H_2 with CO_2, N_2 and CH_4. The separation factors for H_2/CO_2 were tested with a number of ZIF membranes. The greatest separation factor was achieved using ZIF-95 followed by ZIF-8, ZIF-7 and ZIF-90 exhibiting separation factors of 35, 20.29, 18.3 and 15.3 respectively. These membranes also showed good H_2/N_2 separation performances. The membranes reviewed reportedly overcame the Robeson upper bound by utilizing a molecular sieving mechanism when tested on laboratory scale experiments. This promoted high

separation of incondensable inorganic/ condensable organic gasses, specifically regarding H_2/CO_2 binary mixtures (Melgar et al, 2015).

Diaz et al. investigate the separation performance of ZIF-8 poly (1,4- phenylene ether-ether-sulfone) hybrid membranes and found that increasing the ZIF content increased the permeability with negligible effect on selectivity. Diaz et al. concluded that increasing the filler content improved the gas transport properties of the membrane (Díaz et al, 2011).

Li et al, investigated the mixed gas separation potential of ZIF-7 membranes. Permeation tests for the 1:1 H_2/CO_2 mixture were conducted at 220°C. The selectivity and separation factor were determined to be 13.0 and 13.6 respectively. This supersedes the Knudsen separation factor of approximately 4.7. Equally desirable results were observed for H_2/N_2 and H_2/CH_4 permeation tests. Permeation test were repeated at temperatures between 50- 220 °C. The permeability of H_2 was reported to have increased with increasing temperatures indicating an activated diffusion mechanism, while that of CO_2 remained relatively constant. The selectivity factor was increased from 5.4 to 13.6 with a temperature increase from 50 to 220 °C. Apparent activation energy of 11.9 kJ/mol was calculated for H_2 permeation. This can be used as a measure of membrane quality as high-performance membranes have activation energy greater than 10 kJ/mol. ZIF-7 was also seen to exhibit reversibility upon temperature cycling and displayed good thermal stability. Both H_2 and CO_2 permeability was not temperature dependant, showing no change with increasing pressure (Li et al, 2010).

Etxeberria-Benavides et al. investigated a ZIF-94 filler on a 6FDA-DAM polymer matrix for carbon dioxide and nitrogen separation. Separation performance was evaluated by pure and mixed gas experiments at constant temperature over a range of pressures (Etxeberria-Benavides et al, 2017). The membrane was prepared by a solution-casting method for different ZIF-94 loadings (0-40 wt. %) and analysed on a lab scale as well as up-scaled. The filler/ polymer/ tetrahydrofuran solution was cast to a thickness of 80 µm. Good adhesion between the filler and polymer was evident and even dispersion of the filler on the polymer, without agglomeration was observed through SEM imaging at all filler loading percentages. A lower permeability was expected for mixture separation due to competitive sorption between components. The polymer membrane had a greater affinity for CO_2 and thus, nitrogen permeability was decreased. CO_2/N_2 selectivity increased from 14 for pure gasses to 24 for the gas mixture (15 CO_2: 85 N_2). CO_2 and N_2 permeability was seen to increase with increasing ZIF-94 loading. Increased CO_2 permeability was attributed to disruption of chain packing of the polymer, the porosity of the Filler particles and an increase in polymer free volume. It was determined that the polymer controlled selectivity while the ZIF filler introduced faster

transport pathways. Separation performance at 40 wt. % ZIF-94 was situated on the Robeson-limit and was found to represent the highest permeability at similar selectivity values as compared to literature (Etxeberria-Benavides et al, 2017).

ZIF-8 nanoparticles were synthesized by the rapid room temperature method by Song et al. to produce particles of approximately 60 nm in size. ZIF loadings from 10-40 wt. % were dispersed within a polymer membrane through the solution casting technique. Vacuum annealing of the membrane to remove any residual solvent subsequently improved the membranes permeability. Increasing ZIF-8 loading up to 30 wt. % resulted in improved permeability with negligible effects to selectivity. The composite membrane produced with 40 wt. % nanocrystals was extremely brittle, breaking into small pieces preventing their use in permeation tests. Good correlation between experimental data and the Maxwell model was experienced. Small deviations are attributed to the non-ideal nature of the ZIF dispersion and the changes in polymeric fee volume that the model does not account for (Song et al, 2012).

2.3.1.2 Carbon nanotube membrane

In an attempt to transcend Robeson's upper bound, Kim et al, tested the permeability and selectivity of a mixed matrix membrane consisting of functionalized carbon nanotubes and a polysulfone membrane. Single walled carbon nanotubes (SWNT) were selected as fillers due to their improved transport diffusivities, approximately an order of magnitude faster than zeolites with a similar pore size (Kim et al, 2007).

Weight fractions of 2.5, 5, 10 and 15% SWNT on the PSF membranes were fabricated by solution-casting and the membranes were covered to slow the rate of solvent evaporation thereby creating a uniform thickness without curling. All except the 15 wt. % SWNT displayed even dispersion of the nanotubes, while the 15 wt. % SWNT formed regions of high density nanotubes. The MMMs of various SWNT loadings were evaluated for H_2, O_2, N_2, CH_4 and CO_2 separation. The best absorption was seen in a decreasing order for CO_2, CH_4, O_2 and H_2. Simulations showed greater absorptions than those of experimental isotherms which were attributed to potential blockages formed by impurities, amorphous carbon and residual functional groups. A relative increase in gas absorption was seen between 2.5 and 5 wt. % SWNT loadings but minimal increase was seen between the 5 and 15 wt. % SWNT loadings. The creation of an interfacial zone with re-oriented polymer chains forming different mobility was inferred from DMTA data. The permeability of the pure PSF membrane was reportedly lower than those expressed in literature. Increases in gas permeability for all components were experienced up to 10 wt. % SWNT, from which permeability decreased for all components as the loading was increased from 10 to 15 wt. % SWNT. It was proposed that tortuosity around

high density nanotube regions limited further permeability increases. The membrane was expected to hold a greater affinity for CH_4 which was confirmed by a higher absorption capacity for CH_4 over H_2, O_2 and N_2. The O_2/ N_2 separation ratio remained relatively constant at all SWNT loadings suggesting the absence of unselective regions along the SWNT/PSF interface (Kim et al, 2007).

Kim suggests that nanotube diameters below 10 Å utilized in a polysulfone membrane may transcend the Robeson limit by combining high permeability with size selectivity. While this investigation makes use of carbon nanotubes as opposed to silica sodalite the MMM fabrication technique and SWNT loading results are applicable to the common polysulfone membrane.

2.3.1.3 Halloysite nanotubes for mixed matrix membranes

An asymmetric MMM was fabricated utilizing polyethermide (PEI) and hallyosite nanotubes (Hashemifard et al, 2011).

Dope preparation factors such as ultrasonic sonication, filler wetting and the priming period were analysed for their effects on the membranes separation performance. The addition of the filler reduced the selectivity but increased the permeability of the MMM relative to the neat PEI membrane. Increasing the priming period increased the contact between the filer and polymer, reducing free voids and as a result reducing the permeability. Increasing the sonication period increased the selectivity. This was attributed to the breakage of the nanotubes which increased the surface area. Higher permeability also resulted from an increase in the agglomeration of the nanotube pieces. Increasing the wetting period reduced the agglomeration of the nanotubes leading to an increase in both the selectivity and permeability of the membrane relative to the neat PEI.

The unmodified nanotubes were found to adhere poorly to the polymer as shown by the low selectivity evident in both the binary gas permeation tests for CO_2/CH_4 and O_2/N_2 mixtures. Silylated particles showed improved dispersion but re-agglomerated at increased silane concentrations. Increasing the silane concentration lead to improved filler-polymer adhesion but increased the effects of agglomeration and pore blocking. As a result the permeability of the membrane was reduced while the selectivity increased.

As the loading of silylated hallyosite nanotubes was increased, poor dispersion of the particles within the polymer became evident. The Hallyosite nanotubes are not intrinsically selective however; increasing the loading increases the relative selectivity. This was attributed to tortuosity along the membrane channels, resulting in a greater tendency in difference of diffusivities and greater selectivity (Takahashi & Paul, 2006). Enhancements in the solubility of

CO_2 may also occur due to the presence of silane groups which subsequently increase selectivity and permeability. As the loading is further increased the effects of poor dispersion become prominent thereby reducing the selectivity of the membrane (Hashemifard et al, 2011).

The study done by Hashemifard et al. was then extended to produce a selectivity-permeability morphological diagram for fillers with a large pore size such as hallyosite nanotubes. Five main morphologies were identified; ideal (Case I), void (Case II), rigidified (Case III), pore blocking (Case IV) and a combination of pore blocking and agglomerated (Case V). A selectivity-permeability diagram was created and found to be similar to that proposed by Moore and Koros for small pore size fillers except rotated 45° clockwise for large pore size fillers (Moore & Koros, 2005). As a result Case III and a portion of Case IV morphologies would yield higher selectivity and permeability than an ideal morphology. Hashemifard et al. confirmed that the filler pore size, membrane structure (dense symmetric or asymmetric) and the filler particle size form the key factors in gas separation performance (Hashemifard et al, 2011).

2.3.2 Polymeric Membranes for Mixed Matrix Applications

Polymers have been intensively investigated for both pure gas permeations and mixed gas separations but possess poor transport properties, making enhancements through inorganic fillers highly favourable (Ahn et al, 2008).

The combination of zeolite and polymer membranes results in improved separation performance, making them industrially attractive if synthesis can be made feasible (Chakraborty et al, 2016). Ineffective adhesion between the polymer and the external surface of zeolites serves as a challenge to membrane applications. To improve the membrane internal structure a number of procedures are proposed; surface modification of the zeolite particles, preparation above glass transition temperature and heat treatment. Surface modifications were determined to be the most promising procedure for future applications. This was done by attaching organic chains onto the surface of the inorganic filler but while structural improvements were observed, the permeability was decreased and selectivity remained constant (Duval et al, 1994).

Glassy polymers have strong size-sieving abilities producing high selectivity, they are also stable at high pressures and easy to fabricate and upscale. Polysulfone (PSF) is widely used glassy polymer in membrane preparation. PSF membranes are inexpensive to produce and can be fabricated on a large scale necessary for industrial applications. Additional advantages of PSF include high mechanical strength, good thermal and oxidative stability; solubility in most commonly used solvents and a flame retardant nature (Madaeni & Moradi, 2011).

A key factor influencing the performance of MMM is the compatibility of the filler, the polymer and the solvent. Selection should be based on the desired performance and endurance at the commercial process conditions. The polymer determines the minimum separation performance of the system and relies on the addition of the filler to improve selectivity of the resulting membrane. The shape, size and permeation rates of the gaseous species should form as the first selection criteria, followed by filler-polymer compatibility. A solvent with weak polymer-solvent and filler-solvent interactions should be chosen as to allow for easy desorption from the filler surface. The desired strength of the interactions should be chosen as polymer-filler > polymer-solvent > filler-solvent (Rezakazemi et al, 2014).

2.3.2.1 Review of developments in zeolite fillers

In 2016, Kosinov et al. reviewed the recent advancements in zeolite fabrication and the effects of the membrane structure and composition on gas separation performance. Gas separation begins with absorption onto the membrane pore surface. Adoption selectivity is usually the dominant mechanism at temperatures below 200 °C, meaning that molecules with strong polarizability, dipole or quadruple moments are preferentially absorbed, hindering the transport of the other molecules. At moderate temperatures diffusion though the membrane is controlled by surface diffusion while at high temperatures activated gaseous diffusion becomes the dominant mechanism, these are both reliant on the size of the molecule and the membrane pores. In order for a membrane to form a molecular sieve, defects should form less than 10 ppm (Kosinov et al, 2016).

The silica/aluminium ratio strongly affects the adsorption properties of the membrane. As the aluminium (Al) content of the membrane increases it becomes more polar creating stronger interactions. On the other hand, increasing the silica content greatly improved the quality of the membrane. It is commonly believed that Al rich zeolite crystals lead to increased defect formation and poor crystal intergrowth.

Zeolites with pores of 2.8 Å or less are idea for separation of small gas molecules such as H_2 or water. Low-silica sodalite falls into this category displaying ideal H_2/n-C_4H_{10} selectivity above 1000. These membranes are limited by poor permeability and stability due to high Al content. Industrial application of such membranes would require post-synthesis modifications to make them economically attractive. Grafting can modify the adsorption properties and increase the selectivity of a zeolite membrane. Alternatively the pore size may be altered through the deposition of silica inside the zeolite pores such as through catalytic cracking deposition which has significantly improved the H_2/CO_2 selectivity without reducing permeability. Such modifications may be repeated to drastically improve performance. Other methods such as CVD

reduce pore size with added benefits of improving thermal and hydrothermal stability. It was concluded that super thin, defect free, 3-dimensional pure silica membranes would be highly effective for the separation of small gas molecules such as H_2 (Kosinov et al, 2016).

Shen and Lua compared the experimental and theoretical densities of zeolite 4A and poly(vinylidene fluoride) mixed matrix membranes and found the experimental densities to be much lower than the theoretical values. Single gas permeation tests on He, CO_2, O_2 and H_2 produced permeabilties of 14.65, 6.62, 1.01 and 0.3 barrer respectively at 32 wt. % loading. Desirable selectivities of 105.5, 31.5 and 3.3 were seen for He/N_2, CO_2/N_2 and O_2/N_2 (Shen & Lua, 2012).

Junaidi et al. fabricated SAPO-44 polysulfone membranes through phase inversion using ethanol as the solvent. Before casting the membranes were degassed to remove microbubbles than may affect the membrane structure. Filler loadings from 5-20 wt. % were tested but dispersion was negatively affected by filler loadings above 5 wt. %. The best separation performance was seen at a loading of 5 wt. % for both CO_2/N_2 and CO_2/CH_4 separations. At loadings above 10 wt. % particle agglomeration lead to the formation of large interfacial voids which negatively impacted selectivity. Further modifications to the filler and PSF membrane would be required in order to produce defect free membranes at higher filler loadings to improve the separation performance (Junaidi et al, 2013).

Kim repeated a similar experiment using mesoporous MCM-48 silica in polysulfone membranes. The compatibility of 10 wt. % MCM-48 (before calcination) on the glassy polymer was analysed by conducting permeability measurements utilizing He and O_2. A surfactant was electrostatically bonded to the external surface of the silica to determine the wetting property of the polymer and detect the presence of defects. The high surface coverage of silanol groups provided good interactions with the PSF interface. The continuous pathways present in the matrix at high MCM-48 loading favoured high gas permeation. Increases in solubility and diffusivity were experienced, relating to increased permeability with increasing MCM-48 silica content, while selectivity remained relatively constant (Kim et al, 2007).

Sűer et al. analysed a polyethersulfone (PES) membrane in combination with zeolites 13X or 4A. Different membrane preparation techniques were utilized and the permeability and selectivity of N_2, O_2, Ar, CO_2 and H_2 were tested at various zeolite loadings. The morphology of the PES mixed matrix membranes were examined under a scanning electron microscope (Suer et al, 1994).

The membranes were initially prepared by dissolving the PES and selected percentage of zeolite in dimethyl-formamide and stirring thoroughly. The solution was then cast onto a glass plate forming a 500 μm thick film. Procedure A (solution casting) allowed the films to dry for 24 hours at room temperature followed by annealing for 6-8 hours at 80-100 °C. Procedure B (dry/wet phase inversion) dried the films at barometric pressure with nitrogen circulation for 8-10 hours at 60-80 °C. The films were quenched with water. Annealing was conducted for 16-24 hours at 80-100 °C. Procedure B was repeated allowing drying under partial vacuum pressure to form Procedure C. The membrane preparation procedure was found to strongly affected gas separation. The membranes produced from Procedure A had a paper-like structure, was highly permeable and non-selective. Membranes produced from Procedure B were extremely brittle which prevented the preparation of membranes with a high zeolite loading. The main difference between Procedure B and C was believed to be the drying rate of solvent. In Procedure B the drying rate is initially slow followed by rapid drying which inhibited the relaxation of intersegmental packing and caused a dense matrix to form thereby limiting gas permeation. The opposite occurs in Procedure C forming a less dense and highly permeable matrix.

The permeability of all species initially decreased with increasing zeolite loading but from loadings between 33-42% increases in permeability were seen up to a maximum load of 50 %. Selectivity increased with increasing zeolite loading for both 13X and 4A. Special consideration should be taken for the reaction of different polar gasses with the zeolite and the dispersion of the zeolite within the MMM. It was concluded that molecular sieving was not the sole mechanism responsible for gas separation; zeolite shape-selectivity, gas polarity and membrane micro-structure were also found to play a role in permeability (Suer et al, 1994).

2.3.2.2 Polysulfone membranes

Rafiq et al. developed a polysulfone/polymide blended asymmetric membrane with inorganic silica nanoparticles through phase inversion for the separation of CO_2/CH_4. Overall the membranes showed good thermal stability. The presence of the silica nanoparticles improved the separation performance of the membrane up to a critical agglomeration at a silica loading of 20 wt. %. A maximum selectivity of 61 was observed at a loading of 15 wt. %. Mixed gas permeation tests showed good correlation to the ideal gas selectivity (Rafiq et al, 2012).

Mixed matrix membranes consisting of Polysulfone (PSF) and nonporous, fumed silica nanoparticles were prepared with varying silica volume fractions by Ahn et al. The membrane's density, thermal degradation, glass transition temperature and silica distribution were investigated. Permeability tests were conducted utilizing H_2, He, O_2, N_2, CH_4 and CO_2 (Ahn et al,

2008). PSF-silica membranes were prepared by solution-casting with chloroform to produce membranes of 60-80 μm thick. Silica agglomeration was seen at all silica loadings. Higher silica loadings related to increased agglomerate size however, it should be considered that juxtaposition through the depth of the membrane may lead to the interpretation of poorer dispersion. A positive proportionality was found between gas permeability and silica loading despite agglomeration. This was attributed to increasing free volume due to inefficient chain packing and additional void spaces at the silica-PSF interface. The gas permeability in the both pure and MMM decreased with the increasing molecular size of the gas species, producing the best and worst permeability for H_2 and CH_4, respectively. No improved selectivity/permeability relation was seen when compared to Robeson's upper bound (Ahn et al, 2008).

Moradihamedani et al. developed a titanium dioxide (TiO_2) polysulfone membrane by wet/wet phase inversion and crosslinking to study the effects of titanium loading on membrane morphology and CO_2/CH_4 separation (Moradihamedani et al, 2015). Membranes were prepared with 0, 1, 3, 5 and 7 wt. % TiO_2. Up to 3 wt. % increases in the surface layer thickness and homogeneous TiO_2 distribution were evident. Critical agglomeration was seen above 5 wt. % TiO2, this lead to the formation of macrovoids and defects causing a significant reduction in the selectivity of CO_2/CH_4. Both the CO_2 and CH_4 permeability were proportional to titanium loading at loadings below 3 wt. % and greater than 5 wt. %. At 1 bar and 3 wt. % TiO_2 perfect separation was experienced as CH_4 molecules were unable to diffuse through the membrane. The surface roughnesses of the various TiO_2 membranes were greater than that of the pure PSF membrane. Moradihamedani et al. concluded that an ideal morphology (Case 1) was present in membranes with TiO_2 loadings below 3 wt. % and that interface void morphology (Case 2) was present in TiO_2 loadings above 5 wt. % (Moradihamedani et al, 2015).

2.3.3 Preparation and characterization of MMMs

Complications in the synthesis of MMMs arise due to incompatibility between the two phases (the polymer and the filler) resulting in poor filler dispersion which leads to the formation of membranes with undesired morphologies. Poor interfacial adhesion between the polymer and the external surface of inorganic fillers and the agglomeration of filler particles serve as challenges to membrane applications by reducing the selectivity of the membrane. (Mahajan & Koros, 2002).

Most MMM are produced through the solution-casting technique. This involves the initial priming of the zeolite through sonication which reduces agglomeration of the particles and aids membrane formation. The filler particles are dissolved in the solvent and placed in an ultrasonic bath to form a homogeneous dispersion. The polymer (5 – 10 wt. %) is then added to the

solution and stirred and sonicated repeatedly (Rezakazemi et al, 2014). The membrane is then cast in a petri-dish or by a doctor blade and gradually cooled to allow evaporation of the solvent. The asymmetric membrane is formed through the microphase separation phenomenon in the evaporation stage. This stage causes the greatest stress on the membrane and can potentially form micro-voids which negatively impacts separation performance. Excess solvent is evaporated and the membrane is dried in a vacuum oven to remove any residual solvent (Zornoza et al, 2013).

Another common approach to membrane formation is wet phase inversion. This process involves the immersion of the cast membrane in a non-solvent quench medium. Wet phase inversion is used to fabricate membranes for micro and ultra-filtration, reverse osmosis and gas separation but the selectivity is often hindered by surface pores and defects. This fabrication procedure involves the conversion of a one phase polymer solution to a two phase mixture containing a polymer rich solid phase and a polymer poor liquid phase which produces pores within the membrane. The solution mixture generally contains between 10-30 wt. % of polymer. The polymer is cast into thin films .The homogeneous solution splits when quenched with water or an aqueous solvent to form two distinct layers, forming an asymmetric membrane. This structure is desirable due to the smaller pores in the surface layer which form during very rapid precipitation producing a highly selective, size sieving layer. The secondary layer is thicker determining the transport properties of the membrane and provides mechanical support (Porter, 1990; Ahn et al, 2008).

A third approach, dry-wet phase inversion, involves a microphase separation where the surface undergoes solvent evaporation and the bulk of the membrane experiences solvent/ non-solvent exchange during quenching (Pinnau & Koros, 1991). Pinnau et al, investigated the effect of fabrication method on the gas separation properties of polysulfone utilizing a mixture of methylene chloride, 1,1,2-trichloroethane and 2-methyl-2-butanol as a solvent and methanol as the quench medium. Dry phase inversion (solution casting) produced low flux due to thick skin layers while dry/wet phase inversion method to produce a highly selective ultra-thin skin layer which was absent in wet phase inversion, resulting in greater separation performance (Pinnau & Koros, 1991).

Inhomogeneous phases form during the fabrication of MMMs due to differences in the physical properties of the filler and the polymer. These defects become more pronounced with increasing filler loading. Increasing the polymer concentration to increase the viscosity of the mixture and thus slow particle sedimentation has been proposed as one potential solution. Other proposed solutions were to form the membrane rapidly to prevent particle precipitation

or utilize ultra-fine crystals smaller than 0.5 μm to reduce gravitational effects (Chunga et al, 2007).

2.3.3.1 Surface Modification

Incompatibilities and poor fabrication procedure can lead to the formation of non-ideal morphologies. Sieve-in-a-cage, leaky interfaces, matrix rigidification and plugged sieves result from poor interfacial adhesion, blockage of the dispersed phase and stress cracking. To ensure high performance membranes are produced three main modification techniques; grafting, blending or crosslinking can be applied to mitigate the effects of non-ideologies (Rezakazemi et al, 2014).

Grafting creates a chemical bond between two different polymers that would otherwise not blend well to prevent the microphase separation of the main polymer. Either of the polymers of the dispersed phase can be grafted to improve the filler-polymer compatibility (Bhattacharya & Misra, 2004).

Blending mixes two different polymers without chemically bonding them to produce a mixture with different physical properties. Homogeneous and heterogeneous blends can be made as long as the polymers are partly miscible in each other. The former tend to exhibit better mechanical strength and are thus preferred to heterogeneous blends (Bos et al, 2001). Polysulfone and polymide blending combines two polymers with high and low plasticization tendencies to produce a blend with significantly more resistance (Bos et al, 2001). Other experiments produced PSF-polymide blends with increased critical plasticization pressures and improved thermal and chemical stability (Kapantaidakis et al, 1996). Blending can also positively impact the membranes permeability, selectivity and pressure stability (Visser et al, 2007).

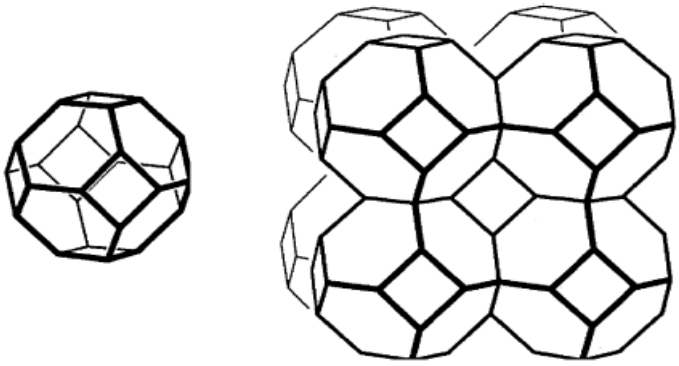
Crosslinking modifies the microstructure of the polymer to increase the selectivity and reduce swelling and plasticization of the membrane. This uses chemical modifications of silane coupling agents to increase chemical bonding between two sections of the framework. A disadvantage of this method is a reduction in mechanical strength with excessive crosslinking. Depending on the polymer, crosslinking can be conducted by chemical reaction, irradiation or physical crosslinking (Berry et al, 2000). The crosslinking of a number of polymers was conducted and found to improve the selectivity of CO_2/CH_4 in 6FDA copolymides with ethylene glycol (Hess & Staudt, 2007); a similar result was seen by when polymide membranes were crosslinked with p-xylenediamine (Tin et al, 2003).

2.4 Sodalite crystals as fillers in MMMs

2.4.1 Hydroxy sodalite and silica sodalite crystals

Layered silicates with frameworks composed of SiO_4 tetrahedra and silanol (SiOH/SiO-) groups have been utilized for various applications such as adsorption, catalysis and catalyst supports, ion exchange and as resin fillers. They contain interlayer cations such as TMA+ cations that are often hydrated. Newly synthesized layered silicates such as RUB-15 contain a unique framework, composed of a segment of the sodalite cage. (Takahashi & Kuroda, 2011)

Hydroxy sodalite (HSOD) is a common zeolites consisting connected 4 and 6 ring cages structures (Figure 2), producing micro pores (of approximately 2.6 Å free diameter) which allow small particles such as helium, ammonia, water and hydrogen to pass through. Guest species such as organic matter, water and anions often become trapped in the cage structure of the zeolites during synthesis, limiting the effectiveness of the sodalite particles (Breck, 1974). In order to affectively apply this to industrial applications such as for H_2/CO_2 separation, higher quality sodalite (SSOD) with the absence of occluded molecules and higher Si/Al ratio needs to be produced.



β cage Sodalite cage structure

Figure 2: Sodalite framework (International Zeolite Association, 2007; Khajavi, et al., 2007)

Copy right permission attained from Elsevier as per Appendix D.2

2.4.2 Synthesis and characterization of sodalite crystals

Various methods have been developed in an attempt to meet the need for the precise synthesis of zeolites.

2.4.2.1 Direct Hydrothermal synthesis

Hydrothermal synthesis forms one of the most common methods. This method utilizes metosilicate precursor gels which are converted through hydrothermal conditions into the desired zeolite structures (Asakura et al, 2014). The removal of occluded water and organic molecules via dehydration leads to the collapse of the cage structure, rendering the sodalite ineffective for absorption and separation applications. The thermal stability of sodalite was studied by Zeng et al, and Khajavi et al, and found to be thermally stable up to 250 ℃ for high quality silica sodalite (Si/Al=5) and up to 500℃ for pure sodalite (Si/Al→∞) (Zheng et al, 2009; Khajavi et al, 2010).

Vaezi and Babaluo investigated the effects of dehydration temperature of the sodalite on the H_2/CO_2 separation performance of a sodalite/ceramic membrane and concluded that increasing the dehydration temperature negatively affected separation performance due to the collapse of the sodalite cages (Vaezi & Babaluo, 2014).

2.4.2.2 Topotactic Conversion

The properties associated with a specific zeolite are reliant on its composition, structure and morphology. A lack of understanding of the zeolite crystallization mechanism makes the prediction and control of fabricated zeolites difficult. Topotactic conversion is a relatively new synthesis method that enables the production of zeolite structures with unique new chemical frameworks, compositions and morphologies (Koike et al, 2017)

Topotactic conversion takes a bottom up approach in utilized existing layered silicates as mother layers. Condensation between the silanol groups on adjacent zeolite layers occur spontaneously during thermal treatment preventing the breakage of layers or the need for additional silicates. This has produced zeolites structurally identical to the mother layers, allowing for precise predictions of the synthesized products (Moteki et al, 2008).

Previous attempts to produce silica sodalite from RUB-15 through topotactic conversion proved unsuccessful as calcination of the silanol groups could not be effectively condensed (Oberhagemann et al, 1996).

Moteki et al. reported a novel silica sodalite without occluded organic matter enabling effective use of micro pores. Such materials could be ideally used for computers (Wang et al, 2001), inert gas adsorption into sodalite cages and fillers for mixed-matrix membranes. RUB-15 was selected for synthesis as the single sheets are identical to those of the (110) plane sodalite. A new synthesis route was developed to shorten synthesis time. The starting material RUB-15 ($[N(HC_3)_4]_8[Si_{24}O_{52}(OH)_4]\cdot 20H_2O$) underwent pseudo-solid-state transformation through

heating in a closed autoclave without additional water. Acid treatment utilizing hydrochloric acid was implemented to convert Si-O^- groups to Si-OH groups. This product was calcined to condense silanol groups but amorphous products resulted. Koike et al. attributes this to the inter-layer alkali-metal ions which remain causing layers to become mismatched (Koike et al, 2017). Moteki et al. found that treatment with acetic acid successfully shortened the interlayer distance; these samples were then heated at 800°C to successfully form silica sodalite. This method produced silica sodalite of a plat-like morphology which is different to naturally occurring and all previously synthesized silicates. The thermogravimetric (TG) weight was analysed and elemental analysis confirmed the absence of occluded organic species. Hydrogen absorption of 0.13 wt. % was observed at 303 K and 10 MPa (Moteki et al, 2008).

2.4.2.3 Stepwise Topotactic Conversion

Koike et al. (2017) developed a stepwise process for the synthesis of pure silica sodalite with minimal defects and plate-like morphology. This method claims to expand the potential layered silicates for zeolites production to include those which cannot be directly calcined. Defects result from incomplete and irregular interlayer condensation, intralayer condensation and stacking disorders due to variations in interlayer environments. As a result zeolites with low-crystallinity or amorphous material are formed. The proposed process utilizes interlayer condensation and elimination of organic guest species to produce a higher quality silicate with fewer defects (Koike et al, 2017).

Koike et al. investigated the control of the stacking sequence through acetic acid treatment and subsequent interlayer condensation by refluxing in NMF before calcination. They attempted to produce silica sodalite through a stepwise process treating three sample variants (See

Table 1). RUB-15 samples were produced and intercalated with acetic acid (Ac-RUB-15) or hydrochloric acid (H-RUB-15). A portion of the Ac-RUB-15 underwent subsequent intercalation of N-Methylformamide (NMF) to produce NMF(rt)-Ac-RUB-15. The remaining Ac-RUB-15 and the H-RUB-15 samples were refluxed with NMF. All samples produced underwent calcination; heated at a rate of 10°C/min and calcined at 800°C for 5 hours in dry air.

Powder x-ray diffraction, CHN elemental analysis, Solid-state Si and C CP/ MAS NMR spectra and thermogravimetric measurements were utilized to determine the state of samples produced (See

Table 1).

Table 1: Summary of sample preparation methods and results (Koike et al, 2017)

Samples Used	Production Method	Results After Calcination
RUB-15	Hydrothermal treatment of the precursor gel; heated in a sealed Teflon vessel at 140 °C for 7days. Centrifugation was used to separate off a white solid which was washed and dried at 70°C overnight	Amorphous. 60.9 % of the sample remained after TG-DTA analysis up to 900 °C and a 14 % weight loss of interlayer water was seen
H-RUB-15	RUB-15 was diluted in HCl (1M) for 1 day at room temperature; the sample was removed through centrifugation, washed and dried overnight at 70 °C	Amorphous. Reduced basal spacing. Virtual removal of TMA cations. reduced nitrogen content
Ac-RUB-15	RUB-15 (0.1 g) was treated with acetic acid (6 M, 30 mı) for 3 hours at room temperature. The sample was filtered, washed and dried at 60°C	Reduced basal spacing. Partial guest exchange of TMA cations with hydrated protons and acetic acid (60% of sodalite cages) reduced nitrogen content Amorphous
NMF(rt)-Ac-RUB-15 Variant 1	Ac-RUB-15 (0.1 g) diluted in NMF (40 mı) for 1 day at room temperature. The desired product was separated through centrifugation, washed and dried at 60°C	Strong Q^3 and Q^4 signals indicating defects and/or an amorphous phase
NMF(180rt)-Ac-RUB-15 Variant 2	Ac-RUB-15 (0.1 g) was refluxed in NMF (40 mı) for 1 hour at 180 °C. Sample was filtered and dried under reduced pressure.	All Si-OH groups condensed, small amount of amorphous phase. Formed sodalite without organic guest species
NMF(180rt)-H-RUB-15 Variant 3	Same procedure as above utilizing H-RUB-15	Incomplete layer condensation. Did not produce sodalite framework.

Koike et al. concluded that NMF critically influenced the degree of interlayer condensation. Carbon and nitrogen contents below 0.2 wt. % indicated effective removal of organic guest species. NMF reflux was advantageous for producing a silica sodalite framework with a plate-like morphology and fewer defects than direct topotactic conversion (Koike et al, 2017).

2.4.2.4 Layer Reassembly

Zhao et al. (2013) investigated the production of FER-type zeolites from RUB-36 by layer reassembly. They determined that stricter control of the layer stacking sequence and closer interaction between silanol groups is vital to successful topotactic conversion. This method of layer reassembly was studied due to the presence of strong hydrogen bonds between the layers, specifically considering local interactions between inorganic molecules and organic moieties (Marler & Gies, 2012). Successful topotactic conversion from layered RUB-36 to a pure silica FER-type zeolite was achieved in the presence of cetyl-trimethyl-ammonium hydroxide. No significant structural degradation was present as the zeolite ZSM-35 produced depicted the same structural features as the mother silicate layers. The transformation mechanism consisted

of swelling and the intercalation of CTA+ cations followed by the de-swelling and removal of CTA+ cations leaving surfactant molecules in the void spaces between layers. The CTA+ cations act as the structure directing agents for FER-layer formation (Zhao et al, 2013). While this method does not make use of RUB-15, layer reassembly may be extended to the formation of other layered zeolites

2.4.3 Factors affecting synthesis of high-quality silica sodalite

Moteki et al, (2011) concluded that acid pre-treatment was a crucial step for topotactic conversion. They extended their work to investigate the effects of the length of the alkyl chain of the acid, treatment time and concentration on sodalite crystallinity (Moteki et al, 2011). Formic acid, acetic acid, propionic acid and butyric acid were tested at concentrations from 1 M to 9 M. The same synthesis procedure was followed as per their 2008 study. High crystallinity sodalite was formed utilizing propionic acid followed by acetic acid at concentrations of 3-9 M, formic and butyric acid produced amorphous products. Low crystallinity was observed at low acid concentration which was attributed to a low degree of ion exchange. Optimum acid concentration of 6 M was determined to produce the highest crystallinity. Sodalite crystallinity was increased with increasing acid treatment time from 10 seconds to 10 minutes after which no improvement was seen for sodalite treated for 3 hours. However, residual TMA^+ cations were still present in samples treated for 10 minutes indicating the presence of occluded organic matter. While silica sodalite with plate-like morphology was successfully synthesized through topotactic conversion, occluded matter from structural directing agents was still present within the sodalite cages.

While this study serves as a good introduction, improvements and further investigation into the effect of synthesis parameters on sodalite quality are still required to produce silica sodalite without occluded matter.

2.4.4 Sodalite crystals in membrane applications

Hydroxy sodalite has been utilized in membranes for a number of applications including the dewatering of alcohols, seawater desalination (Khajavi et al, 2010), organic acid dehydration as well as in the separation of azeotropic mixtures and gas separation (Daramola et al, 2015).

General fabrication of HSOD membranes involves the growth of the zeolite, through hydrothermal synthesis, on a porous support structure. HSOD membranes have been formed through microwave heating and secondary growth formation but these methods are defective as the inhomogeneous temperature profile of the solution and support during in microwave

heating forms excess amounts of loose HSOD powder and the orientation of crystal growth in secondary growth is difficult to control leading to the formation of thick membranes with low flux. Kajavi et al, reported an in situ method for the formation of thin, defect free membranes supported on asymmetric α-alumina disks (Khajavi et al, 2007). Nitrogen and helium permeations were conducted on the HSOD membranes without dehydration and found to be impermeable to nitrogen; such a membrane has potential in water purification but is inapplicable in gas separations.

Daramola et al, investigated HSOD/PES mixed matrix membranes for acid mine drainage and found the membranes to be of an asymmetric nature, with good tensile strength, that increased with increasing SSOD loading, and high flux (Daramola et al, 2015).

HSOD on tubular ceramic supports were fabricated by Vaezi et al. by hydrothermal synthesis. HSOD dehydrated at 100°C produced the best H_2/CO_2 separation with a separation factor of 21 and H_2 and CO_2 permeance of 3.8×10^{-8} and 1.8×10^{-8} mol/m^2.s.Pa, respectively. Membranes dehydrated above 150°C displayed poor selectivity and defects (Vaezi & Babaluo, 2014). Daramola et al, also fabricated HSOD ceramic membranes but utilized a pore plugging synthesis protocol. The membranes were found to have greater mechanical strength and thermal stability than those synthesized via hydrothermal synthesis (Daramola et al, 2017).

Zheng et al reported a number of investigations conducted on low-silica sodalite which observed high H_2 permeance of 1.14×10^{-7} mol/m^2.s.Pa and decent He/N_2 permselecivity (Xu et al, 2004). Zheng studied the thermal stability, template removal and hydrogen accessibility of varying framework Si/Al rations and found thermal stability for low, high and pure-silica sodalite to be 380, 550 and 480 °C, respectively (Zheng et al, 2009). However, no investigations into high and pure silica sodalite membrane separations were found.

2.5 Membrane properties and operating conditions

2.5.1 Thermal and Hydro-thermal Stability

Current industrial large scale hydrogen production occurs through the water-gas shift reactions. This reaction takes place at high temperatures, ranging between 200- 500 °C. This reaction produces large amounts of hydrogen, carbon dioxide and steam due to the exothermic, reversible nature of the reaction (Smith et al, 2010). Subsequently, membranes designed to purify the hydrogen need to be thermally and hydro-thermally stable.

A ZIF-69 membrane was studied for its chemical and thermal stability by Liu et al. and was found to have good stability in boiling methanol, benzene and supercritical CO_2 (Liu et al, 2010).

The ZIF-90 membrane synthesized by Huang et al. performed excellently in gas mixtures of H_2, CH_4 and steam at a temperature of 200 °C (Huang et al, 2010). Further studies into this membrane revealed exceptional thermal and hydro-thermal stability without sacrificing separation performance. ZIF membranes were tested up to 325 °C in an attempt to simulate industrial conditions associated with the treatment of flue and exhaust gasses to ensure the reliability and reproducibility of the separation performance (Melgar et al, 2015).

ZIF-7 Polyethyleneimine (PEI) membranes were tested for hydrothermal stability by analysing the permeability and separation factor for an equimolar H_2/CO_2 mixture with an additional 3 mol % steam. The test was conducted over a period of 60 hours and stable permeability for both H_2 and CO_2 were observed (Li et al, 2010).

The thermal stability of polysulfone-silica mixed matrix membranes was investigated. The full procedure was published by Ahn et al. The sample decomposition was observed from 520 °C. The glass transition temperature of the PSF membrane is reported at around 188°C but is highly dependent on the thermal, mechanical and processing procedures used in fabrication (Ahn et al, 2008).

2.5.2 Mechanical Strength

Polymer-zeolite membranes are more flexible than alumina-based zeolite membranes and their mechanical properties can be analysed by considering their elastic constants. Polymer-zeolite membranes can be formed in two ways; where the zeolite is grown on top of the polymer surface (Type 1) or where the zeolite is grown within the pores of the polymer (Type 2). Chakraborty et al. investigated the elastic properties of zeolite- PES membranes for both Type 1 and Type 2 variations in an attempt to compare separation performance of CO_2/N_2 and mechanical strength. Type 1 showed a greater selectivity but reduced permeability for both CO_2 and N_2 as compared to Type 2. Poor reproducibility and sensitivity to handling has also been noted with Type 1 zeolite membranes. Type 2 membranes were observed to withstand greater tensile and compressive strain only failing at a bending radius curvature of 0.5" as opposed to 2". The cracks present in Type 1 membranes penetrated the zeolite and PES layers with lengths exceeding 250 nm. In Type 2, the cracks were limited to the brittle zeolite zones reaching 75 nm on average as the cracks were arrested by the polymer. Type 2 membranes showed greater ductility and the flexibility failing at strains greater than 1.14 %. (Chakraborty et al, 2016)

This experiment shows the importance of the membrane fabrication procedure and the advantages of interspersed zeolites in the polymer membrane. Mixed matrix membranes should further extend this hypothesis producing membranes with high mechanical strength.

2.5.3 Operating Conditions

Peivasti et al. previously noted that the feed concentration, temperature and downstream pressure were the key operating conditions affecting membrane separation in liquid mixtures (Peivasti, et al., 2008). The effects of these conditions on the pervaporation separation of toluene from n-heptane were then investigated by Iravaninia et al (Iravaniniaa et al, 2011). Feed compositions between 10-40 wt. %, temperatures ranging from 25-85 °C and downstream pressures of 2-32 mBar were tested on a MSE- modified acrylonitrile composite polymeric membrane. The membrane was determined to have a greater selectivity for toluene. Increases in both the temperature and feed composition positively affected the permeation flux while decreased the selectivity, while a decrease in downstream pressure positively influenced both the permeability and selectivity. Due to the permeability-selectivity trade-off the best separation results were obtained by decreasing the downstream pressure to a strong vacuum and increasing the temperature at a low feed concentration (Iravaniniaa et al, 2011).

2.5.4 Economic Feasibility

Moparthi et al. studied the economic feasibility of silica and palladium MMM reactors for the dehydrogenation of ethylbenzene and propane. A conceptual design based methodology was simulated to account for the non-linear nature and the combination effect of reactor volume, membrane surface area, membrane thickness, pressure and gas flowrate. The inclusion of the membrane and auxiliary equipment was found to account for approximately 20 % of total costs. Both membrane types were found to have similar performance results. Membrane reactors were compared to conventional reactor systems and determined to produce 60-70 % greater profit for the production of propylene from propane. When the simulations were applied to the case of the production of styrene from ethylbenzene, negligible profit increases were experienced. A significant improvement in conversion was seen in both reactions and determined to be economically favourable for dehydrogenation reactions. Moparthi et al. concluded that further research should be applied to the production of cheaper inorganic composite membranes that are able to undergo temperature cycling, fouling and deactivation for industrial application in dehydrogenation reactions (Moparthi et al, 2010).

The economic feasibility of a number of binary gas mixtures was simulated by Hinchliffe and Porter. The costs of membrane separation were compared to that of the standard commercial distillation processes for oxygen/nitrogen, hydrogen/carbon monoxide and propane/butane separation. The hydrogen/carbon monoxide system was the only system found to be economically feasible with membrane separation producing a total cost 20% less than that of distillation. This came at the cost of reducing the carbon monoxide purity from 97 to 95 % using

a cellulose acetate membrane. Simulations with a TRIS (3-trimethyl-siloxy-γ-methacyloxypropylsilane) membrane produced a 40 % cost reduction as compared to distillation. The conventional distillation systems for O_2/N_2 and propane/butane were determined to be 6 and 100 times more cost effective than membrane systems. Hinchliffe and Porter concluded that polymeric membrane systems are unlikely to be favourable for the separation of mixtures already utilizing commercial distillation. However, molecular sieve membranes would likely replace commercial distillation should high permeability, high selectivity membranes become available on an industrial scale (Hinchliffe & Porter, 2000).

2.6 Concluding remarks

This chapter serves as background into the need for carbon capture and storage, currently employed technologies and advances in membrane developments. While membranes have been utilized for H_2/CO_2 separation the body of work is limited and no investigations into the use of pure-silica sodalite have been reported for H_2/CO_2 separation. Furthermore, the current synthesis of sodalite produces sodalite cages with occluded organic matter and anions, limiting its application in gas separation technologies. Topotactic conversation is a promising process for the production of high silica sodalite without the presence of occluded matter although better understanding of the effect of synthesis parameters on the sodalite quality is required.

Chapter 3: Methodology

3.1 Introduction

This chapter outlines the research methods used to investigate the three research objectives; the synthesis of silica sodalite produced by topotactic conversion and the optimization of synthesis parameters, the fabrication of silica sodalite filled polysulfone mixed matrix membranes of various loadings and their gas separation performance (Chapter 1). The materials and instrumentation utilized are listed and the analysis methods used are described. The methods of data collection and experimental design were designed are also mentioned. Lastly, the ethical considerations of this research are declared.

3.2 Equipment and devices

The following equipment was used in the synthesis of the SSOD and HSOD crystals as well as fabrication of the membranes following the method presented in Chapter 3.3:

1. Teflon lined autoclave (60 ml): Parr Instrument Company (276AC2 T304 053013), USA
2. Magnetic stirrer: Lasec, Benchmark Scientific Inc. (H400-HSE), Korea
3. Centrifuge: Hettich zentrifugen (Rotofix 32 A), Germany
4. Oven: Therm-O-Mat
5. Ultra-sonicator: Scientech Ultrasonic cleaner (703), South Africa
6. Furnace: Lenton, South Africa
7. Doctor blade: Sheen (1117/ 300mm), UK
8. Membrane module: Millipore corporation high pressure filter holder (XX4504700)
9. Various glassware and measuring apparatus were used on loan from the School of chemical and Metallurgical engineering

3.3 Synthesis of sodalite crystals and membrane fabrication

3.3.1 Silica sodalite

For the synthesis of silica sodalite crystals (SSOD): Tetra-ethoxysilane (TEOS, reagent grade 98 %, Sigma-Aldrich, South Africa), tetrametyl ammonium hydroxide (TMAOH, 25 wt. % in water, Sigma-Aldrich, South Africa) and acetone (Sigma-Aldrich, South Africa) were used as received for the synthesis of RUB-15. Propionic acid (>99.5 wt. %, Sigma-Aldrich, South Africa) was used without purification for the production of sodalite.

The modified procedure of Moteki et al. was used for the synthesis of RUB-15 and silica sodalite (Moteki et al, 2008). TEOS and TMAOH were combined in a 1:1 molar ratio and stirred for 24 hours to homogenize. The solution was then placed in a Teflon autoclave and heated at 413 K for 7 days. RUB 15 was recovered as a white waxy substance, which was washed with acetone, separated by centrifugation and dried overnight at 333 K in a convection oven to yield a white powder.

The obtained RUB-15 (0.1 g) was dispersed in propionic acid (30 ml) of varying concentrations (1-5 M) as this was considered to play a role in the quality of sodalite produced (Moteki et al, 2011). The suspension was stirred at 900 rpm for various treatment periods (10-180 minutes) as again investigated with inconclusive results by Moteki et al (2008). The solution was separated by centrifugation, washed repeatedly with deionized water and dried in a convection oven overnight at 333 K. The samples were then calcined for 1-5 hours at temperatures between 873 and 1173 K. This temperature range was initially investigated in an unpublished study by the school of chemical and metallurgical engineering.

3.3.2 Hydroxy Sodalite

For the synthesis of hydroxy sodalite crystals (HSOD): Sodium metasilicate (Sigma-Aldrich, South Africa), sodium hydroxide pellets (Sigma-Aldrich, South Africa) and anhydrous sodium aluminate (Sigma-Aldrich, South Africa) were used.

HSOD crystals were synthesized by hydrothermal synthesis using sodium metasilicate, sodium hydroxide pellets, anhydrous sodium aluminate, deionized water of 5 SiO_2: Al_2O_3: 50 Na_2O: 1005 H_2O molar composition. The solution was thoroughly stirred in a PTFE cup and thermally treated in a Teflon lined autoclave as described by Daramola et al. (Khajavi et al, 2010; Daramola et al, 2015).

3.3.3 Mixed matrix membranes

For membrane fabrication: Polysulfone (beads (transparent), Sigma-Aldrich, South Africa) and N,N-Dimethylacetamide (>99.9 %, Sigma-Aldrich, South Africa) were used.

The PSF (5 g) was degassed and dried at 100 °C in a vacuum oven overnight. The mixed matrix membranes were formed through a wet inversion process (Ahn et al, 2008; Pinnau & Koros, 1991).

Measured amounts of the synthesized silica particles (0, 5, 10, 15 wt. %) were mixed with N,N-Dimethylacetamide (20 ml) and stirred using a magnetic stirrer for 3 hours before the PSF

was dissolved and mixed for a further 24 hours. The mixture was repeatedly ultra-sonicated for 30 minutes and stirred to ensure an even dispersion of particles. Finally, the mixture was stirred at low speed and left to stand for 5 minutes before casting to reduce the presence of small air bubbles. The solution was cast on a glass plate using a doctor blade and submersed in a bath of deionized water. The membrane was then removed from the plate and soaked for a further 24 hours to ensure maximum solvent removal. The membranes were then oven dried at 60 ℃ for 2 hours.

3.4 Analysis and characterization

Single and multi-point Brunauer-Emmett-Teller (BET) analysis was conducted by the school of chemistry from the results of Nitrogen Physisorption at 77 K, to determine the surface area and pore volume of the sodalite samples. Sodalite particles assessed in the preliminary and extended investigations were tested using single-point analysis due to financial limitations, while the sodalite samples optimized from regression analysis were tested using multi-point analysis to study the adsorption isotherms.

Powder X-ray diffraction (XRD) patterns were performed on both the precursor RUB-15 layers as well as the calcined sodalite using a Bruker D2 XRD with CuKα radiation (λ=1.54184 Å) to analyze the crystalline and amorphous nature of the sodalite. Due to the low yield of silica sodalite synthesized and limitations on chemical and financial resources, only the best sample runs from BET analysis in the extended investigation were synthesized in sufficient quantity for XRD analysis. Scanning electron microscopy (SEM) was conducted on a Carl Zeiss sigma field emission scanning electron microscope equipped with Oxford X-act EDS detector to examine the surface morphology and elemental composition of the particle and membrane samples. Fourier-transmission infrared spectroscopy (FTIR) was conducted on a PerkinElmer UATR two FT-IR spectrum two spectrometer to identify functional groups and the presence of occluded water. Thermogravimetric (TG) analysis was performed using AS Advanced laboratory solutions (Q600 SDT) with air as the carrier gas at a temperature ramp of 20 ℃/min up to a temperature of 900 ℃. Particle size analysis was conducted on a Malvern Mastersizer 2000 wet dispersion unit. Tensile strength analysis was conducted using a Stable Micro Systems texture analyser (TA-XT Plus) and Young's modulus (E) calculations (Equation 24) in order to assess the mechanical strength of the fabricated membranes. This utilized the applied force (F), the cross-sectional area (A) and the initial (L_0) and final lengths (L) (McNaught & Wilkinson, 1997).

$$E = \frac{tensile\ stress}{tensile\ strain} = \frac{F\ L_0}{A\ (L - L_0)} \qquad \text{Equation 24}$$

A rig was constructed with a membrane module by past students and utilized for membrane gas separations together with gas chromatography conducted on a Bruker (430-GC). Membrane thickness was measured by an InSize digital outside micrometer (3109-25A) and utilized in gas permeability calculations.

3.5 Model formulation and explanation

Design expert v.11 Software (Stat-ease, USA, 2018) and Matlab Software (2016) were utilized to analyse the experimental data and statistically analyse a number of candidate model equations to determine regression models.

3.5.1 Preliminary Investigation

Response surface methodology (RSM) was employed to investigate the effect of process variables on sodalite quality. Surface area and pore volume were used as critical responses to characterize sodalite quality.

The quality of silica sodalite synthesized was initially tested by varying three independent process factors (acid strength, acid treatment time and calcination temperature) using a 2^3 full factorial experimental design (with a centre). This method considers three factors at two levels with an additional centre point to produce nine experimental runs. It was chosen over traditional design methods to analyse the interactive effects of design variables while reducing the number of experimental runs. The centre point was included in the design to improve the statistical significance and assist in the exploration of curvature within the design space (Fischer, 1935). The coded values and experimental design can be seen in Table 2 and Table 3. These factors were identified as crucial points in studies done by Moteki et al (2008; 2011) and Koike et al (2017). Figure 3 shows a graphical representation of the design space consisting of the extreme points and the centre.

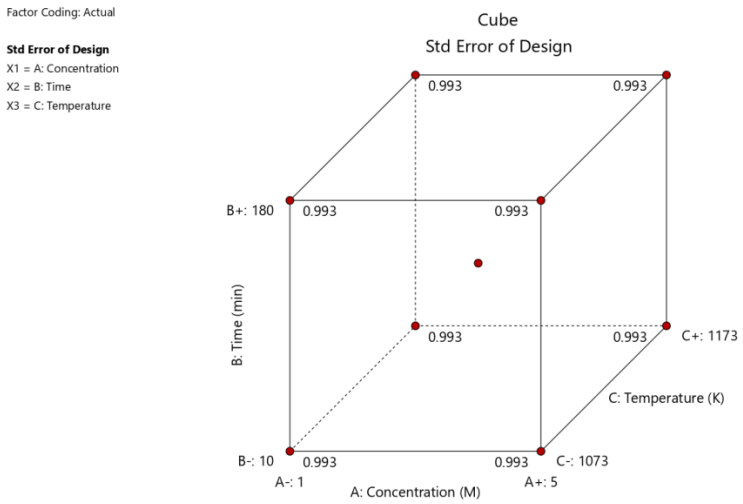


Figure 3: Design space for preliminary investigation

Table 2: Synthesis variables for factorial design

Variables	**Factor**	**Range and Level**		
		-1	0	1
Acid Concentration (M)	A	1	3	5
Acid Treatment Time (minutes)	B	10	95	180
Calcination Temperature (K)	C	1073	1123	1173

Table 3: Experimental design for factorial design

Run	**Coded Values**			**Actual values**		
	a	b	c	A	B	C
				M	minutes	K
SSOD 1	1	1	-1	5	180	1073
SSOD 2	-1	1	-1	1	180	1073
SSOD 3	1	-1	1	5	10	1073
SSOD 4	-1	-1	1	1	10	1073
SSOD 5	1	1	-1	5	180	1173
SSOD 6	-1	1	-1	1	180	1173
SSOD 7	1	-1	1	5	10	1173
SSOD 8	-1	-1	1	1	10	1173
SSOD 9	0	0	0	3	95	1123

3.5.2 Extended Investigation

As results from the preliminary investigation were unsatisfactory for high quality silica sodalite production this experiment was altered to investigate the effect of calcination time rather than

acid treatment time. A lower calcination time would be desirable to lower the overall energy consumption of the synthesis process.

A Box-Behnken design was used based on a three-level incomplete factorial design for the multivariate optimization. This design consists of a centre point and the medians of the extreme points as shown in Figure 4. This design was chosen for its robust and rotatable nature and increased efficiency over central composite and 3-level full factorial designs (Ferreira et al, 2007). The absence of the extreme points initially investigated in the preliminary investigation was also advantageous to this study.

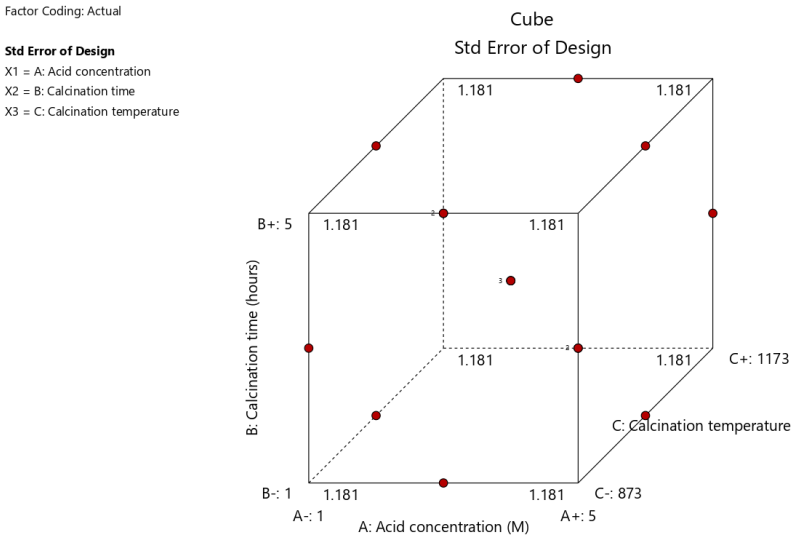


Figure 4: Design space for extended investigation

This design utilized thirteen experimental runs with the centre point in triplicate to produce a total of fifteen runs. Due to the increased number of experimental runs and duplicated synthesis to improve the accuracy and reliability of the data, only small quantities ($\pm$ 0.3 mg) of each were synthesized for BET analysis. The coded values and experimental design can be seen in Table 4 and Table 5. These factors were identified for further investigation following the regression model from the preliminary study.

Table 4: Synthesis variables for BBH design

Variables	**Factor**	**Range and Level**		
		-1	0	1
Acid Concentration (M)	A	1	3	5
Calcination Time (hours)	B	1	3	5
Calcination Temperature (K)	C	873	1023	1173

Table 5: BBH experimental design

Run	**Coded Values**			**Actual values**		
	a	b	c	A	B	C
				M	hours	K
SSOD 1	-1	-1	0	1	1	1023
SSOD 2	1	-1	0	5	1	1023
SSOD 3	-1	1	0	1	5	1023
SSOD 4	1	1	0	5	5	1023
SSOD 5	-1	0	-1	1	3	873
SSOD 6	1	0	-1	5	3	873
SSOD 7	-1	0	1	1	3	1173
SSOD 8	1	0	1	5	3	1173
SSOD 9	0	-1	-1	3	1	873
SSOD 10	0	1	-1	3	5	873
SSOD 11	0	-1	1	3	1	1173
SSOD 12	0	1	1	3	5	1173
SSOD 13	0	0	0	3	3	1023
SSOD 14	0	0	0	3	3	1023
SSOD 15	0	0	0	3	3	1023

3.5.3 Regression model

The general regression model was combined with experimental data to develop a mathematical model with the best fit to the response (Equation 25). Design Expert v.11 Software (Stat-Ease, USA, 2018) and Matlab Software (2016) were used to investigate ten candidate models, ensuring all models maintained hierarchy.

$$y = \beta_0 + \beta a\, A + \beta b\, B + \beta c\, C + \beta ab\, AB + \beta bc\, BC + \beta ac\, AC + \beta abc\, ABC + \beta a_2\, A^2 + \beta b_2\, B^2 + \beta c_2\, C^2 \pm \epsilon$$

Equation 25

In Equation 25, y represents the system response (surface area), βo the intercept of the regression line, βa,b,c the regression coefficients for the respective synthesis variables A (acid concentration), B (acid treatment time/ calcination time) and C (calcination temperature), with ϵ being the mean square error.

An ANOVA test was performed on each candidate model and the P values (within 95 % confidence interval) for each model term and the model as a whole were assessed to determine significance. Lacks of fit tests of the suggested model were also calculated within a 95 % confidence interval, the coefficient of determination (R^2), the adjusted R^2 as well as the mean square error were evaluated to produce the suggested model. The produced model was then utilized to define optimum synthesis factors in order to maximize the response in each investigation.

3.5.4 Gas transport experiments

Nitrogen, hydrogen, carbon dioxide and H_2/CO_2 (60:40) mixture gas cylinders were purchased from Afrox, South Africa with the corresponding gas regulators and used in the experiments. A pure Polysulfone membrane was used as the control experiment. To investigate the effect of sodalite with improved surface area and porosity (SSOD), the 5wt. % SSOD/PSF MMM was compared to the equivalent weighted HSOD/PSF MMM. To investigate the effect of membrane loading SSOD/PSF MMM at 10 and 15 wt. % were also fabricated.

All membranes were tested utilizing the membrane gas separation system utilizing H_2, N_2 and CO_2 pure gasses (Afrox, >99.9 %), see Appendix D1 for operation details, from four separate castings of the same solution and the average used to determine performance of pure gas separations at ambient temperature and 1-5 Bar upstream pressure. The permeate gas flow rate and pressure were recorded and used to calculate the permeability and selectivity of the pure gas permeations following Equations 6 and 7 (detailed in Chapter 2.2.2.1).

$$P = \frac{l\,Q}{A\,\Delta p}\,\frac{273.15}{T} \qquad \text{Equation 6}$$

$$\alpha_{a/b} = \frac{Pa}{Pb} \qquad \text{Equation 7}$$

The best individual casting in each category was utilized in the mixed gas separations and analysed over pressures from 1-5 Bar. For the mixed gas separation a 60 H_2: 40 CO_2 gas mixture from Afrox Analytical Services (>99.99 %, allowing the assumption of a purely binary mixture enabling mass balance calculations) was utilized. A sample of the inlet gas was tested on the GC (Bruker 430-GC) using Haysep 5 as a method (operation as in appendix D.2) to determine the response factor at the known concentration. The membrane gas separation system was then conducted following Appendix D1. The flow rate, pressures and temperatures of the system were noted and a sample drawn from the permeate stream and tested on the GC utilizing the response factor and the area of the peak to determine the mole fraction of the component. This data was applied to Equations 8 and 9 to calculate the component permeability and selectivity (detailed in Chapter 2.2.2.2).

$$P_a = \frac{X_{perm}\,l\,Q}{A\,(p_{feed}\,X_{feed} - p_{perm}\,X_{perm})} \qquad \text{Equation 8}$$

$$\alpha_{a/b} = \frac{X_{perm,a}\left(p_{feed}\,X_{feed} - p_{perm}\,X_{perm}\right)b}{X_{perm,b}\left(p_{feed}\,X_{feed} - p_{perm}\,X_{perm}\right)a} \qquad \text{Equation 9}$$

3.6 Ethics

The research undertaken did not involve animal experimentation or human participants as defined in section A.4 of the Senate Standing Orders on Higher degrees. Waiver letter number HRECNMW19/09/02.

3.7 Waste

The chemical used in this study were hazardous to human and aquatic life, corrosive, flammable and carcinogenic. Synthesized sample quantities were therefore, minimized where possible to reduce the acid and zeolite waste produced; such as by limiting sample quantities in the preliminary investigation. All waste solutions were categorized into classes A, B, C or D, and correctly disposed in line with the procedures of the School of chemical and metallurgical engineering.

3.8 Concluding remarks

This chapter discussed the methodology utilized in this research. Details about materials, equipment and procedure for synthesis, fabrication, and analysis are given. The limitations of the study are discussed relevant to their impact on the results of this work. Design of experiments and regression models utilized in data analysis are explained and calculations of concern are stated.

Chapter 4: Development of silica sodalite with enhanced porosity via topotactic conversion

4.1 Introduction

This chapter focuses on the results and discussion of both the textural and physical characterization as well as modeling the synthesis variables of topotactic conversion of RUB-15 to sodalite. A preliminary study was conducted to analyze the effect of synthesis variables; acid concentration, acid treatment time and calcination temperature, which was extended to further understand the effects of calcination time and a wider range of calcination temperatures on the quality of silica sodalite synthesized in the detailed investigation.

4.2 Experimental

4.2.1 Synthesis and characterization

Silica sodalite was synthesized in accordance with Chapter 3.3.1 varying the propionic acid concentration (1-5 M), the acid treatment time (10-180 minutes) and the calcination temperature (1073-1173 K) for 5 hours following the experimental design set out in Chapter 3.5.1. Hydroxy sodalite was synthesized via hydrothermal synthesis according to Chapter 3.4.2. The crystals were characterized in terms of textural and physio-chemical properties as previously discussed in Chapter 3.4.

The investigation was extended to synthesize SSOD in accordance with the design of experiment in Chapter 3.5.2 varying the propionic acid concentration (1-5 M) for a treatment period of 180 minutes, the calcination time (1-5 hours) and the calcination temperature (873-1173 K). The crystals were characterized in terms of textural and physio-chemical properties as previously discussed in Chapter 3.4.

SSOD was synthesized in triplicate following the optimum conditions specified. The quality and morphology of this sodalite was analysed to confirm the models developed in the Chapter 4.3.2 according to the methods described in Chapter 3.4. To ensure reproducibility a new batch of RUB-15 was synthesized and treated under the same conditions to form the SSOD utilized in the mixed matrix membranes in the next stage of the study ($SSOD_m$).

4.2.2 Investigating the effect of synthesis variables using response surface methodology (RSM)

A 2^3 factorial experimental design was utilized to investigate the effect of synthesis parameters; acid strength, acid treatment time and calcination temperature, on the quality of silica sodalite produced by topotactic conversion. This design method produced 8 experimental runs with the addition of a center point to make a total of 9 runs. The sodalite quality was quantified using BET analysis, and the surface area and pore volume were used as responses to model the synthesis parameters as detailed in Chapter 3.5.1. The effect of synthesis variables was determined utilizing RSM. The design of the experiment was changed from a 2^3 full factorial design to a 3 factor Box-Behnken design to incorporate more experimental points and omit the extreme points in the corners of the design space an extended investigation. The surface area and pore volume from BET analysis were used as responses to model the synthesis parameters as detailed in Chapter 3.5.3.

4.3 Results and discussion

4.3.1 Analysis and characterization: preliminary and extended investigation

4.3.1.1 Textural properties

The surface area (SA) and pore volume (PV) from Brunauer-Emmett-Teller (BET) analysis are displayed in Table 6. HSOD was synthesized to form a baseline for comparison of the SSOD quality. The HSOD surface area and pore volume were determined to be 2.35 m^2/g and 0.012 cm^3/g, respectively. Increasing the surface area and pore volume of the sodalite particles are beneficial for increasing the diffusion and absorption of gasses (Reible & Shair, 1982). While all samples show significant improvements over HSOD results, SSOD 2 and 3 displayed the highest surface area and pore volume reaching values of SA and PV up to 33.9 and 6.8 X that of HSOD. The SA and PV values for SSOD 2 were 79.44 m^2/g and 0.081 cm^3/g while those of SSOD 3 were 70.54 m^2/g and 0.072 cm^3/g, respectively. Both SSOD 2 and 3 were synthesized at low calcination temperature but at opposite levels of acid strength and treatment time. This suggests a crucial role of calcination temperature on the quality of SSOD produced.

The synthesized SSOD is characterized as mesoporous with pore diameters between 2-50 nm. At least a 50 % reduction in pore size of the SSOD was produced leading to greater potential in separation applications.

Table 6: BET results for preliminary investigation

Run	BET results			Relative to HSOD		
	Surface area	Pore volume	pore size	Surface area	Pore volume	pore size
	m^2/g	cm^3/g	nm	m^2/g	cm^3/g	nm
SSOD 1	42.9	0.0653	6.09	18.3	5.5	0.3
SSOD 2	79.4	0.0810	4.08	33.9	6.8	0.2
SSOD 3	70.5	0.0718	4.08	30.1	6.0	0.2
SSOD 4	43.6	0.0640	5.87	18.6	5.4	0.3
SSOD 5	18.8	0.0462	9.81	8.0	3.9	0.5
SSOD 6	26.0	0.0518	7.96	11.1	4.4	0.4
SSOD 7	23.4	0.0512	8.76	10.0	4.3	0.4
SSOD 8	42.3	0.0641	6.06	18.0	5.4	0.3
SSOD 9	21.7	0.0488	8.97	9.3	4.1	0.4
HSOD	2.3	0.0119	20.29	1.0	1.0	1.0

The BET surface area and pore volume results for the Box-Behnken experimental design are shown in Table 7. To improve the accuracy of the model, the synthesis of each experimental runs was duplicated, tested and averaged. No statistical difference was seen between the replicate data, all showing P values > 0.05. Once again the SSOD outperformed the HSOD in terms of surface area (SA), pore volume (PV) and pore size (PS) (Figure 5). The best SA and PV were produced by SSOD 6 (160.9 m^2/g and 0.109 m^3/g) and by SSOD 9 (117.5 m^2/g and 0.115 m^3/g). SSOD 6 produced a surface area approximately 50× that of the HSOD and a pore volume 7.7× larger (Figure 5), while SSOD 9 saw improvements of 44× and 8.6× that of the HSOD SA and PV, respectively. Notably these experimental runs were both conducted at low calcination temperature of 873 K.

Substantial reductions in pore size accompanied the increased SA and PV. The smallest PS was attributed to SSOD 2 which showed an average of 2.52 nm. The improved quality of the SSOD samples support the increased potential of SSOD in separation and absorption application such as the separation of small molecules such as H_2, H_2O and NH_3 from larger compounds.

Table 7: BET results for extended investigation

Trial	Rep 1			Rep 2			Average		
	SA	PV	PS	SA	PV	PS	SA	PV	PS
	m^2/g	cm^3/g	nm	m^2/g	cm^3/g	nm	m^2/g	cm^3/g	nm
SSOD 1	28.9	0.0489	6.77	18.7	0.0349	7.44	23.82	0.0419	7.11
SSOD 2	82.7	0.0479	2.32	115.8	0.0791	2.73	99.25	0.0635	2.52
SSOD 3	87.6	0.0848	3.87	77.1	0.0933	4.84	82.36	0.0891	4.36
SSOD 4	26.7	0.0622	9.33	55.1	0.0778	5.65	40.90	0.0700	7.49
SSOD 5	79.6	0.0880	4.42	4.2	0.0254	23.92	41.93	0.0567	14.17
SSOD 6	160.9	0.1085	2.70	74.3	0.0749	4.03	117.60	0.0917	3.36
SSOD 7	5.7	0.0216	15.16	61.6	0.0642	4.17	33.64	0.0429	9.67
SSOD 8	91.9	0.0723	3.15	34.9	0.0499	5.71	63.42	0.0611	4.43
SSOD 9	117.5	0.1147	3.90	92.0	0.0965	4.20	104.74	0.1056	4.05
SSOD 10	28.9	0.0589	8.16	98.8	0.1038	4.20	63.84	0.0814	6.18
SSOD 11	53.9	0.0653	4.84	98.3	0.0750	3.05	76.14	0.0702	3.95
SSOD 12	13.1	0.0302	9.18	5.6	0.0192	13.72	9.37	0.0247	11.45
SSOD 13	65.6	0.0765	4.66	53.9	0.0391	2.90	59.74	0.0578	3.78
SSOD 14	67.3	0.0876	5.20	67.4	0.0679	4.03	67.35	0.0777	4.62
SSOD 15	56.2	0.0783	5.57	132.7	0.1085	3.27	94.44	0.0934	4.42
HSOD	2.35	0.0119	20.29	-	-	-	2.35	0.0119	20.29

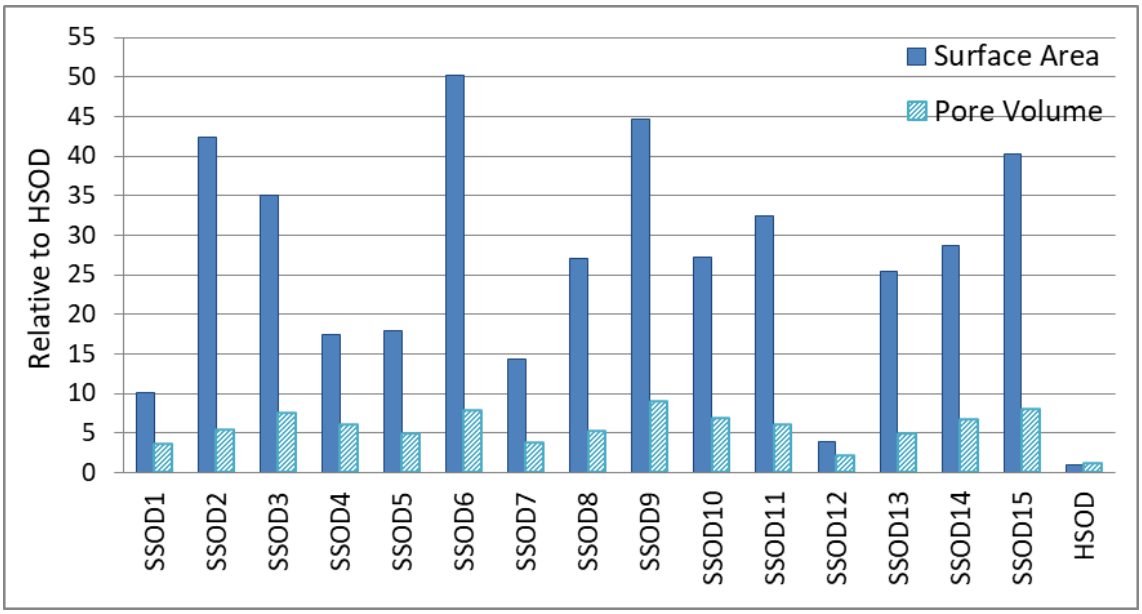


Figure 5: BET surface rea and pore volume of SSOD relative to HSOD results

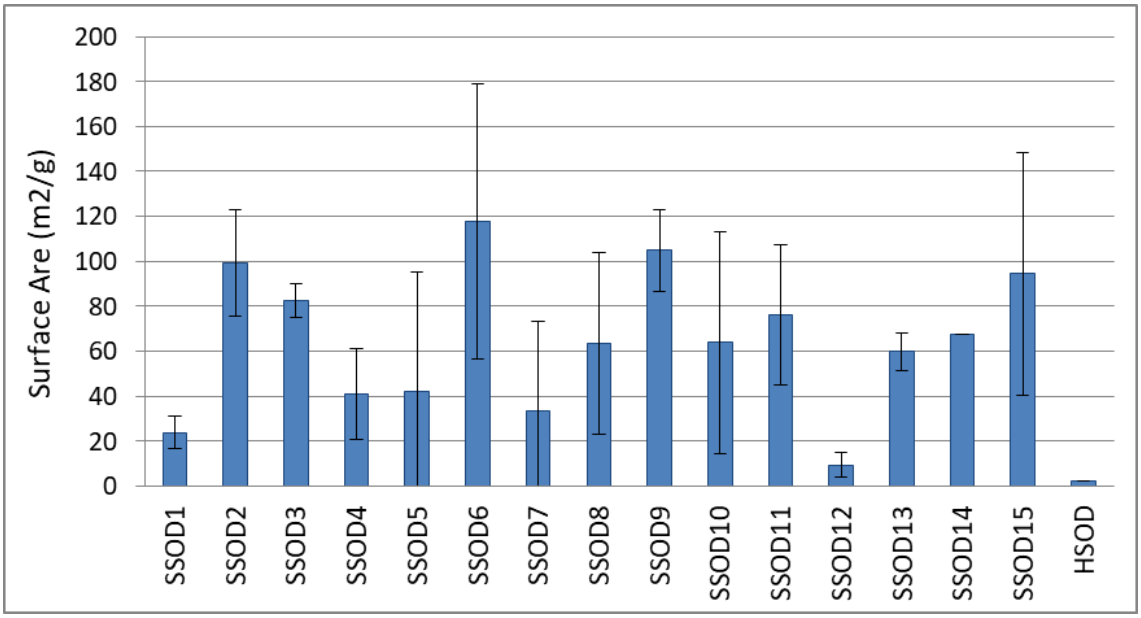


Figure 6: Surface area graph for extended investigation

Important to note is the large deviation between the BET results of replicate experimental runs as can be seen in Figure 6. The experiment was run in duplicate due to limited chemical and financial resources but an increased number of replicates would reduce the standard deviation and improve the accuracy of the model to follow. Some error may also be attributed to human error in the nitrogen phyisorption testing conducted at a laboratory independent from this research.

4.3.1.2 Physio-chemical characterization

Powder X-ray diffraction (XRD)

XRD analysis of the RUB-15 precursor and synthesized sodalite samples were conducted and compared to hydrothermally synthesized hydroxy sodalite and the international zeolite association's characteristic simulated standard peaks for sodalite (International Zeolite Association, 2007).

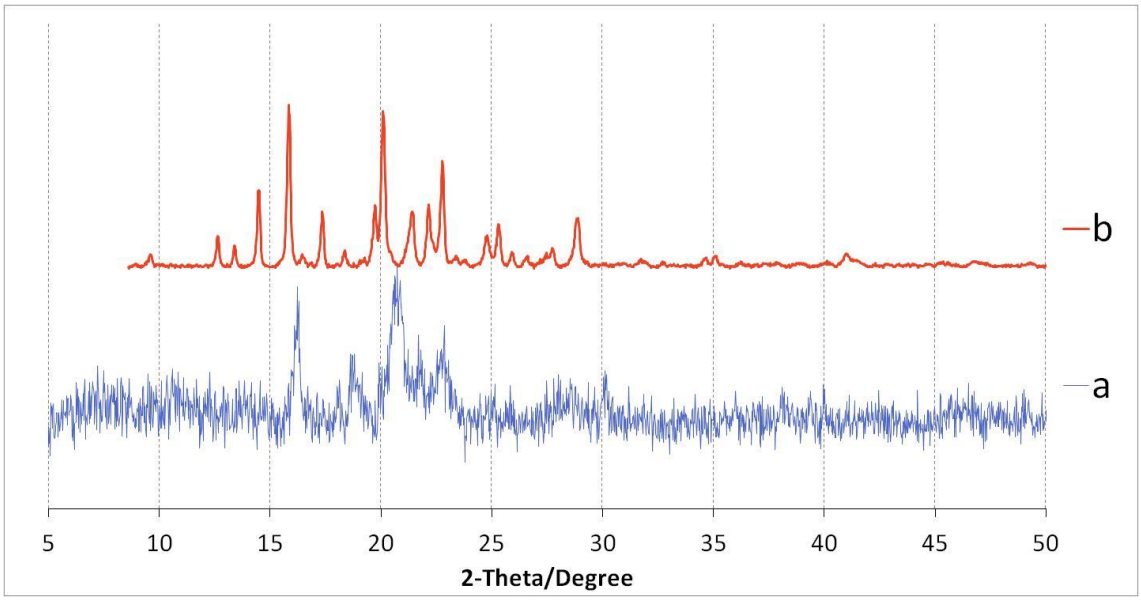


Figure 7: Powder X-ray diffraction patterns for RUB-15 synthesized in a) the preliminary study and b) the extended investigation

Although low density crystalline silicates often form microcrystalline powders of poor crystallinity (Oberhagemann, et al., 1996), the RUB-15 synthesized in the preliminary study (Figure 7a) was exceptionally poor. The pattern holds two of the characteristic peaks displayed by Moteki, et al (2008), Kooli, et al (2016) and Oberhagemann, et al (1996), such as peaks at 2θ= 15° and 22° (see reference graph in Appendix A.4). Notably absent is the strongest intensity peak at 2θ= 6.3°. In addition to the high volume of noise, the presence of an amorphous hump and the low crystallinity, suggest a high volume of intercalated TMA^+ cations (Moteki et al, 2011). The RUB-15 synthesized in the extended study was found to be of a higher crystallinity than that synthesized in the preliminary investigation (Figure 7b). In comparison, the XRD pattern for the second synthesis displays more characteristic peaks and less noise. This suggests an increased potential for the formation of higher crystallinity SSOD. The improved crystallinity may be attributed to the rapid sorption of the TMA^+ cations which stabilize the phase boundary and act as nucleation seeds for new layers. The pattern displayed in Figure 7b closely resembles that produced by Oberhagemann et al (1996), with a number of identical peaks.

The synthesized hydroxy sodalite displayed good crystallinity and alignment of peaks to the IZA simulated standard (International Zeolite Association, 2007) and works conducted by Daramola, et al (2015). A large amount of noise is seen in all sodalite samples (Figure 8) likely due to the poor crystallinity of the RUB-15 precursor. The characteristic peaks at 2θ= 12° shows good intensity but the peak at 2θ= 21° is over shadowed by the amorphous hump between 15-21°. The amorphous nature of the samples may be attributed to the formation of intra-layer Si-O-Si bridges resulting in the incomplete transformation of the crystalline phase (Marler &

Gies, 2012) and the miss-alignment of silicate layers during condensation (Moteki, et al., 2011). Inferior patterns were produced for SSOD 4 and SSOD 8, both utilizing low acid strength and treatment time suggesting that this combination is unsatisfactory for high crystalline SSOD formation, resulting in incorrect layer translation. This agrees with conclusions by (Moteki, et al., 2011) that low acid strength correlates to a low degree of ion exchange and fails to maintain well-ordered structures of the silicate layers resulting in poor crystallinity. In relation to the HSOD the SSOD samples depict much poorer crystallinity and only 2/8 of the characteristic peaks.

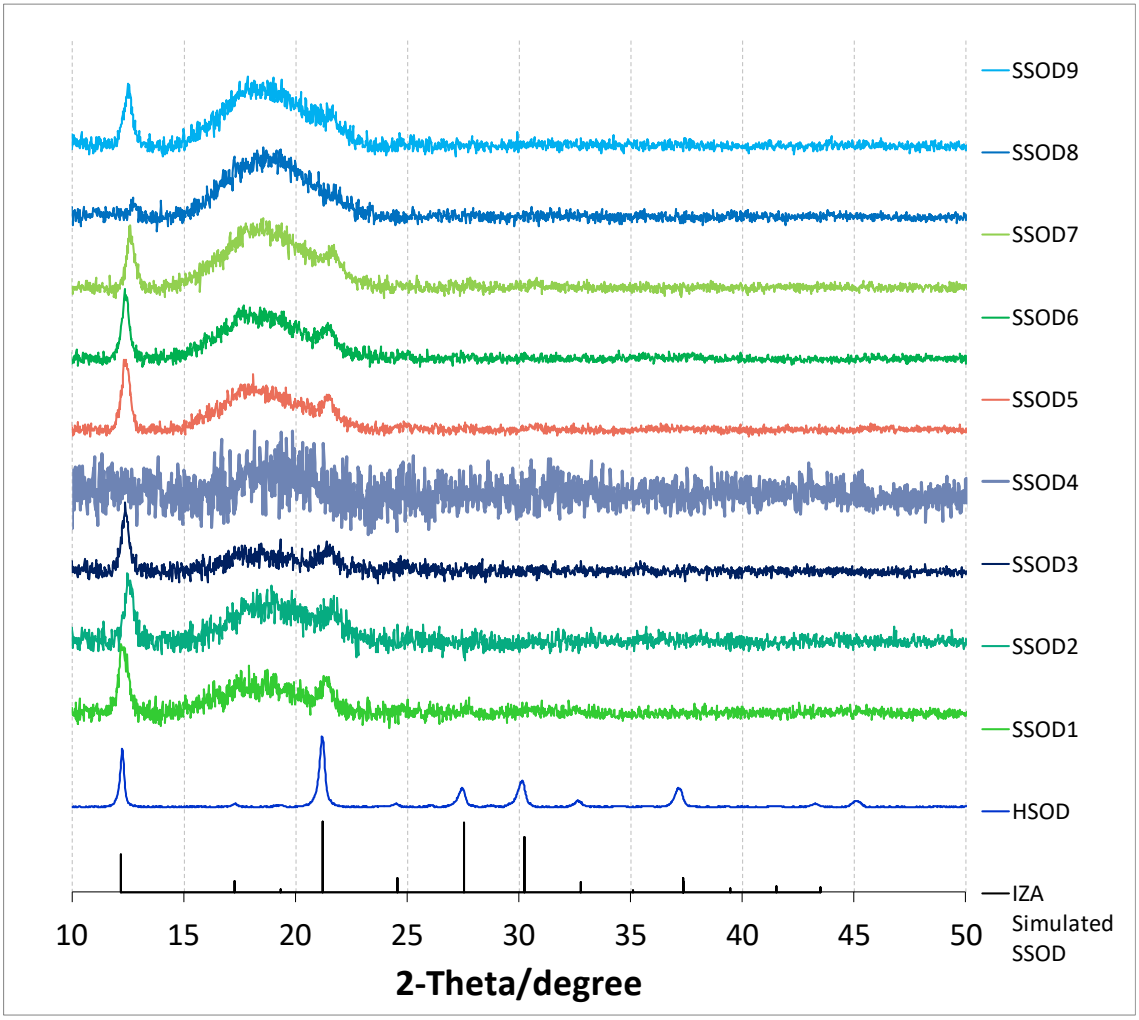


Figure 8: XRD patterns for sodalite samples synthesized in the preliminary investigation

Due to limitations on financial and chemical resource as well as the low yield of SSOD produced (approximately 10:1 RUB-15: SSOD) only the two experimental runs with the greatest BET SA were reproduced in sufficient quantities for XRD analysis. The XRD patterns for sodalite synthesized in the extended investigation, SSOD 6 and SSOD 9 can be seen in Figure 9. These patterns show two large, defined diffraction peaks and up to an additional four with low

intensities, adequately matching the characteristic peaks stipulated by the IZA simulated sodalite standard (International Zeolite Association, 2007).

In comparison the best quality SSOD synthesized in the preliminary investigation (SSOD 2, Figure 9b); those synthesized via the Box-Behnken experimental design show improved crystallinity, less noise and the absence of the amorphous hump. This confirms the hypothesis that improving the crystallinity of the RUB-15 may lead to higher crystallinity SSOD as well as suggests the larger effect of the synthesis variables investigated.

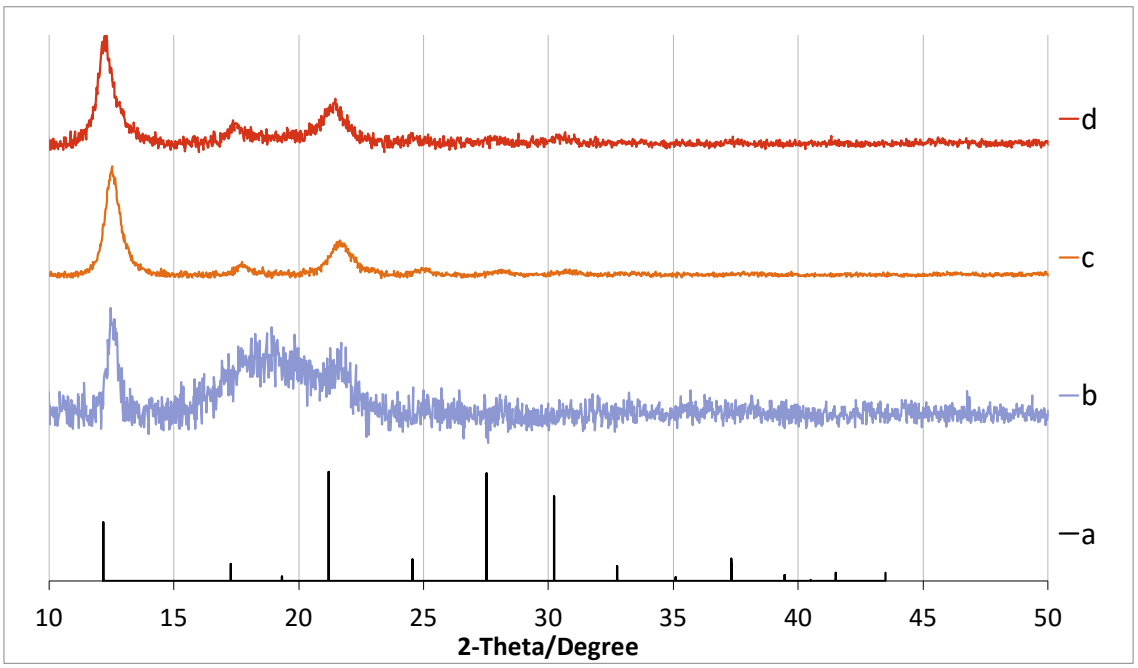


Figure 9: XRD pattern for a) simulated IZA standard; b) Preliminary investigation SSOD 2; c) SSOD 6; d) SSOD 9

Scanning electron microscopy (SEM)

The SEM image of the HSOD supports work by Daramola, et al (2015) showing a thread ball morphology (Figure 10b) consisting of agglomerated rod-like structures, this is significantly different to that of the RUB-15 and SSOD which depict a plate-like morphology.

SEM imaging of the RUB-15 sample shows the plate/sheet-like morphology of similarly sized plates, layered onto one another. The RUB-15 in the preliminary investigation produced irregularly edged oval plates, while those produced by Moteki, et al (2011) displayed a sharper rectangular shape. Oberhangemann, et al (1996) explained this to be due to fast crystal growth along the edge of the silicate layer with slower growth in perpendicular directions i.e. the rate of nucleation is much slower than the rate of growth of existing layers. An indicator of successful topotactic conversion is the correlation of the morphology between the RUB-15 mother layers and the synthesized SSOD. In this case, the small irregularly shaped stacked sheets of the

RUB-15 (Figure 10a) are somewhat similar, but not identical to that of the SSOD. The SEM images of SSOD 1, 2 and 3 were of greater interest as these samples were determined to have the highest BET surface area and pore volume. However, SSOD 8 appears to be the closest morphology to the RUB-15 followed by SSOD 3 with larger, rectangular shaped plates (Figure 10f and 10e, respectively). The remaining samples do depict a plate like morphology some containing larger flatter sheets of varying size, wavy, curled edges and agglomerates. The remaining SEM images can be seen in Appendix A.1.

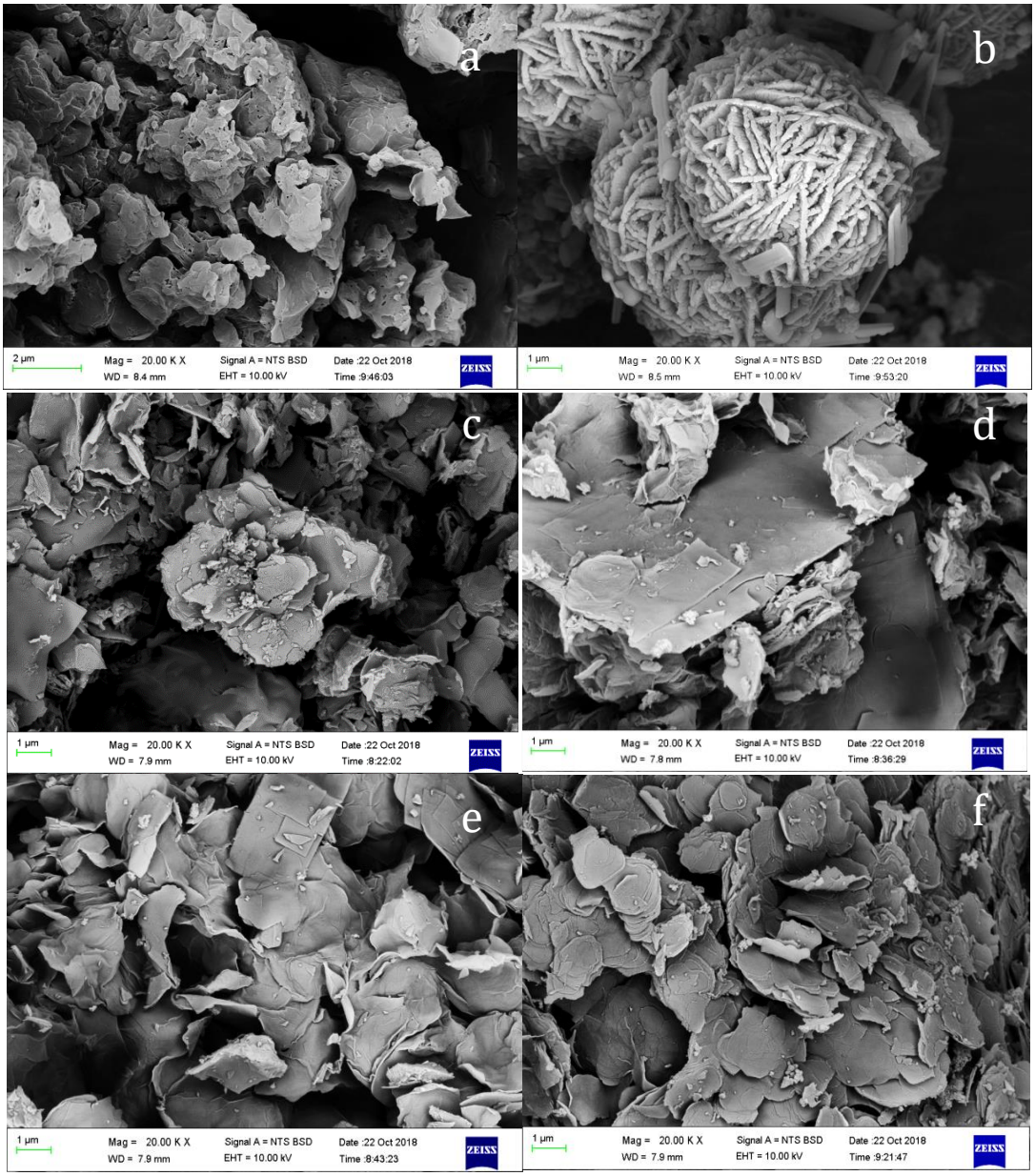


Figure 10: SEM imaging for synthesized samples a) RUB-15; b) HSOD; c) SSOD1; d) SSOD2; e) SSOD3; f) SSOD8

SEM images of the RUB-15 from the second synthesis used for SSOD production in the extended investigation shows plate-like morphology of smooth rectangular plates very similar to that

produced by Moteki et al (2008, 2011). This image confirms the good crystallinity seen in the XRD pattern. The same plate morphology can be seen in SSOD 6 (Figure 11b), where large flat plates are visible under clusters of amorphous phase. SSOD 9 (Figure 11c and 11d) shows a number of partially formed flakes with irregular, ragged edges clustered on larger shattered sheets forming a bark-like texture. This morphology is possibly due to a slow rate of crystal formation due to a lack of energy at low calcination time and temperature (Belviso et al, 2018).

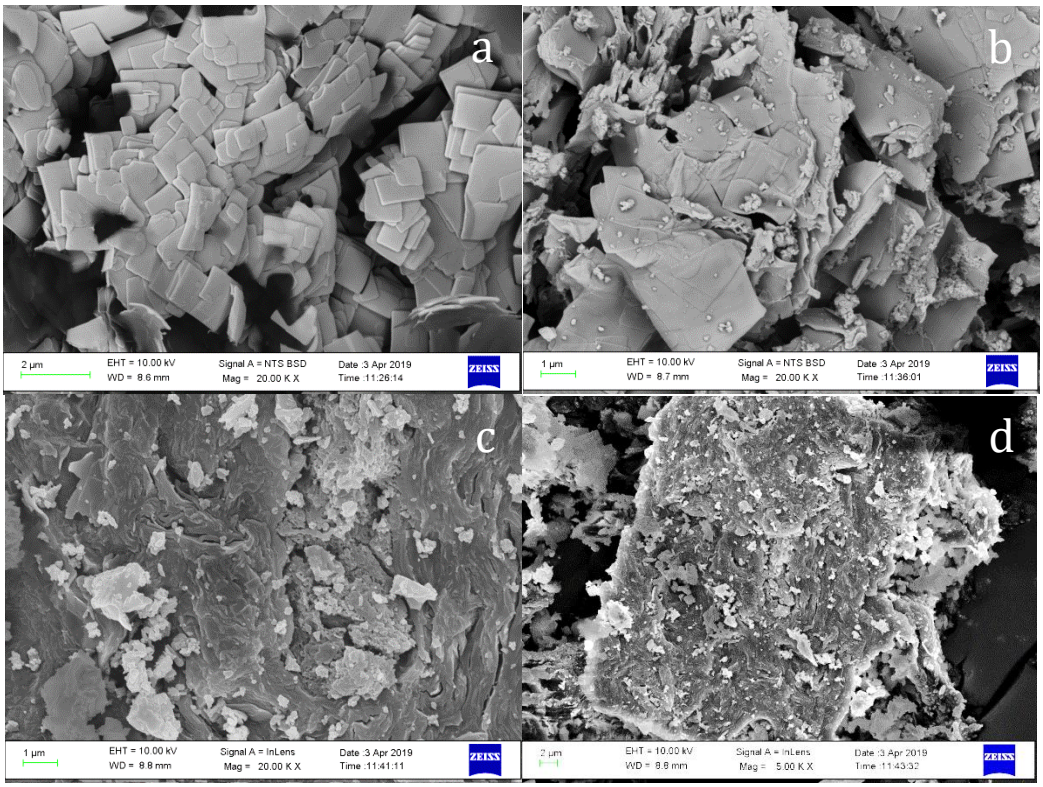


Figure 11: SEM imaging of synthesized samples; a) RUB-15; b) SSOD6; c) SSOD 9 (20kX) and d) SSOD 9 (5kX)

Fourier Transform Infrared Spectroscopy (FTIR)

The FTIR spectrum (Figure 12) of the RUB-15 is very similar to that shown by Koike et al (2017), showing the absorption due to CH_3 deformation at 1488 cm^{-1} as well as the CH_3 asymmetric and symmetric stretching vibrations between 3000 and 3200 cm^{-1}, respectively indicating the presence of tetramethyl ammonium (TMA^+) cations. Of interest in the SSOD absorption spectra is the absence of TMA+ cations at 1488 cm^{-1} confirming the removal of occluded organics from within the cage structures. The absence of an internally bonded OH peak between 3550 and 3570 cm^{-1} confirms the production of silica sodalite without occluded water molecules (Coates, 2006). In relation work done by Koike et al (2017) the silica sodalite

synthesized with propionic acid does not contain any residue molecules or ions interacting with the silanol groups as shown with acetic acid synthesis.

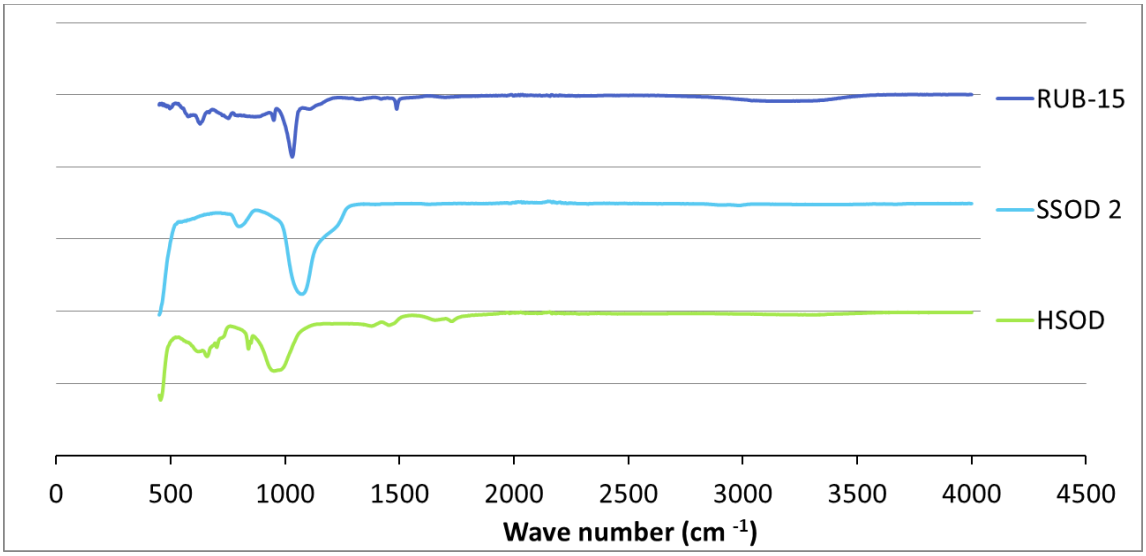


Figure 12: FTIR absorbance spectrum (a.u.) for synthesized samples (preliminary investigation)

The FTIR spectra for the extended investigation are represented in Figure 13. The intensity of the silicate absorption vibrations at 1077 cm^{-1} (900-1100 cm^{-1}) is relatively strong for most samples as compared to that of HSOD, supporting the higher Si/Al ratio. Small peak absorption vibrations at 1096 cm^{-1} indicate the presence of propionic acid adsorbed onto the layers of the sodalite (Coates, 2006) however, the absence of vibrations between 1733-1799 show the lack of interactions such as hydrogen bonding between the acid and the silicate framework (Koike et al, 2017). The presence of a non-hydrogen bonded OH group (3550-3670 cm^{-1}) in some experimental samples shows the presence of small amounts of occluded water within the lattice structure, despite the absence of this in the HSOD sample (Coates, 2006).

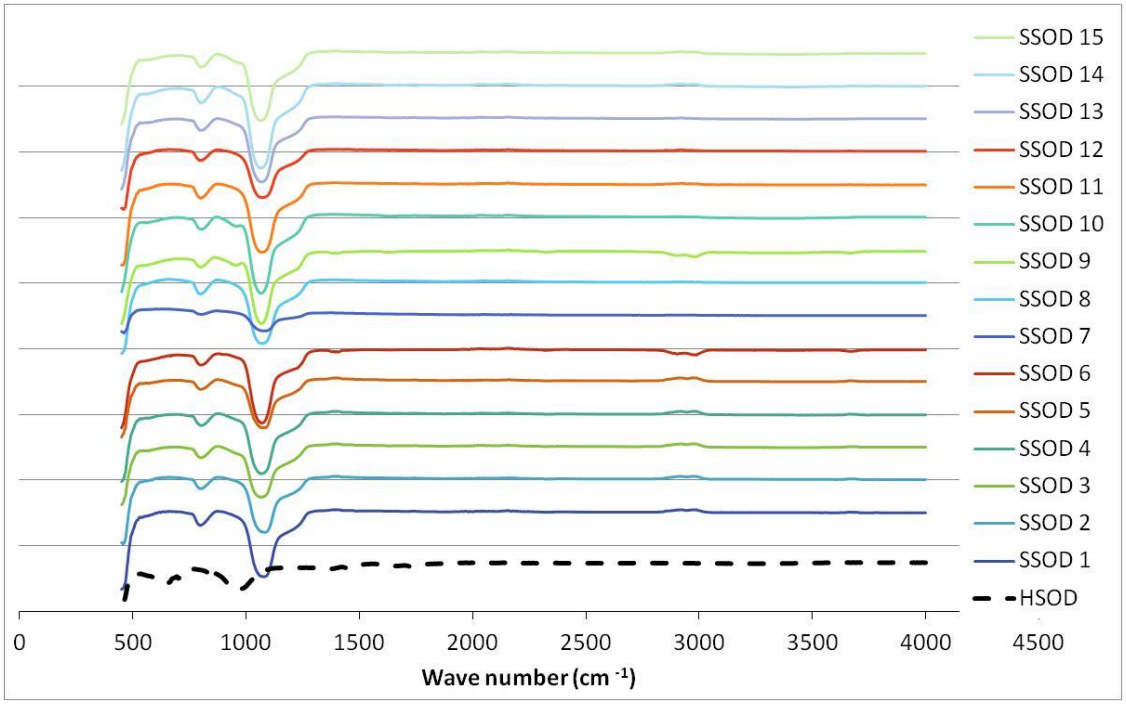


Figure 13: FTIR absorbance spectrum (a.u.) of synthesized sodalite (extended investigation)

4.3.2 Effect of synthesis variables using RSM

Response surface methodology (RSM) was employed to analyse the main and interactive effects of the chosen topotactic synthesis variables on the quality of SSOD produced.

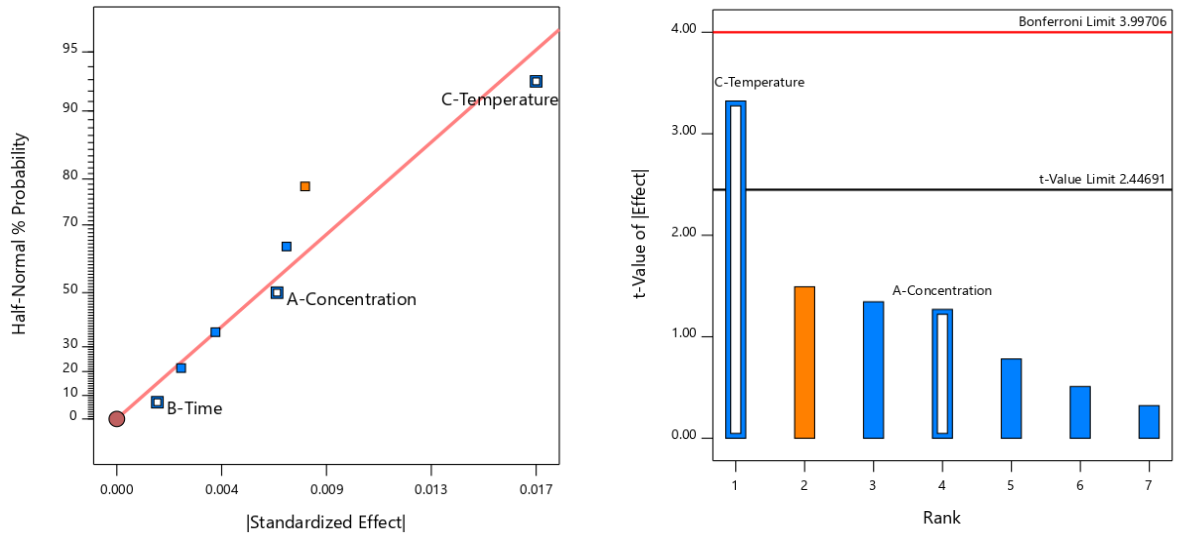
The surface area and pore volume produced from BET analysis results were used as the model responses. Various candidate models (Cubic, Quadratic, 2 Factor-interactive, linear and reduced models) were then developed from the experimental data, and chosen for the best fit using regression analysis and ANOVA tests utilizing design Expert software (Stat-Ease, v11) . Many of these models displayed good regression coefficients and low error but a high model probability (P) value rendering the model insignificant.

4.3.2.1 Preliminary investigation

Pore volume regression model

The half-normal and Pareto charts were examined to determine the significant model factors (Figure 14). Calcination temperature (Factor C) and acid concentration (factor A) fall to the right of the half-normal plot and are likely critical factors. Of these factors, only calcination temperature (C) has a large standardized effect and is likely to be a significant model term. In all the candidate models analysed, acid treatment time (Factor B) had a considerably high P value and close to no effect on the response. It was therefore, determined to be an insignificant factor and removed from the model equation. This is supported by Moteki et al (2011) who showed no

change in the crystallinity of sodalite samples treated for 10 minutes as opposed to those treated for 3 hours with propionic acid (Moteki et al, 2011).



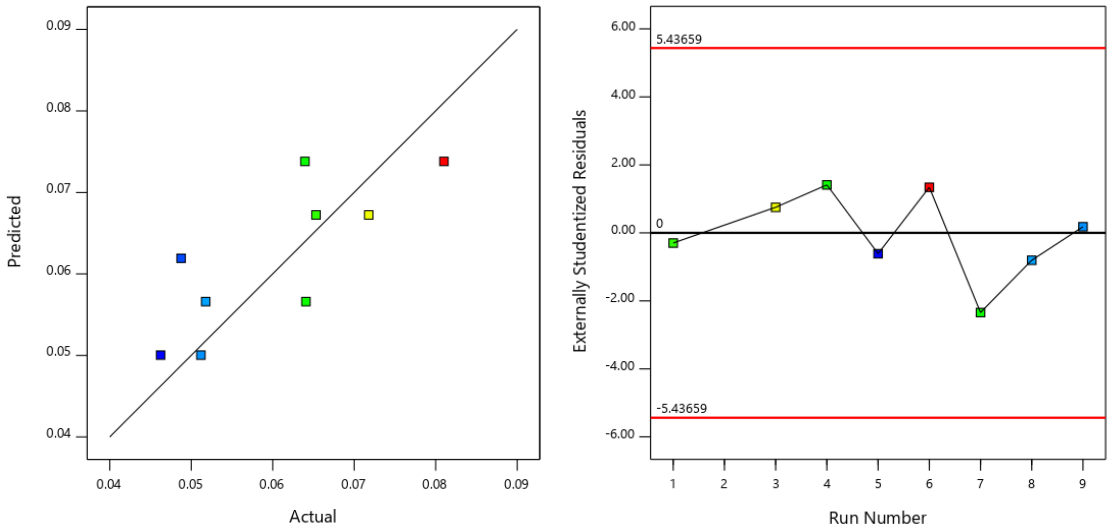
(a) (b)

Figure 14: a) Half-Normal and b) Pareto chart for PV model (factorial design)

A model consisting of factors A and C was chosen as the best fit to experimental data as detailed in Chapter 3.6.3. The empirical model developed to relate pore volume to topotactic synthesis variable is expressed in Equation 26:

$$PV = 0.2599 - 1.64X10^{-3}A - 1.72X10^{-4}C \pm 2.98X10^{-5} \quad \text{Equation 26}$$

Using ANOVA (Table 8) this model was calculated to be significant with a sufficiently low P value of 0.043 ($P < 0.05$, within a 95% confidence interval). A suitable coefficient of determination (R^2) of 0.72 was produced for the model which suggests good correlation between the predicted and experimental data although this is not as close to 1 as desired. 28.36% of the total variation was left unexplained by the model as shown by the spread of points from the 45° line in the plot of predicted vs. actual plot (Figure 15a). The remainder of the model plots show random scatter and good model prediction such as the plot of externally studentized residuals which confirms the independence assumption and depict random scatter. All points fall within the limits and the absence of clustered data confirms the satisfactory fit of the proposed model (Figure 15b).



(a) (b)

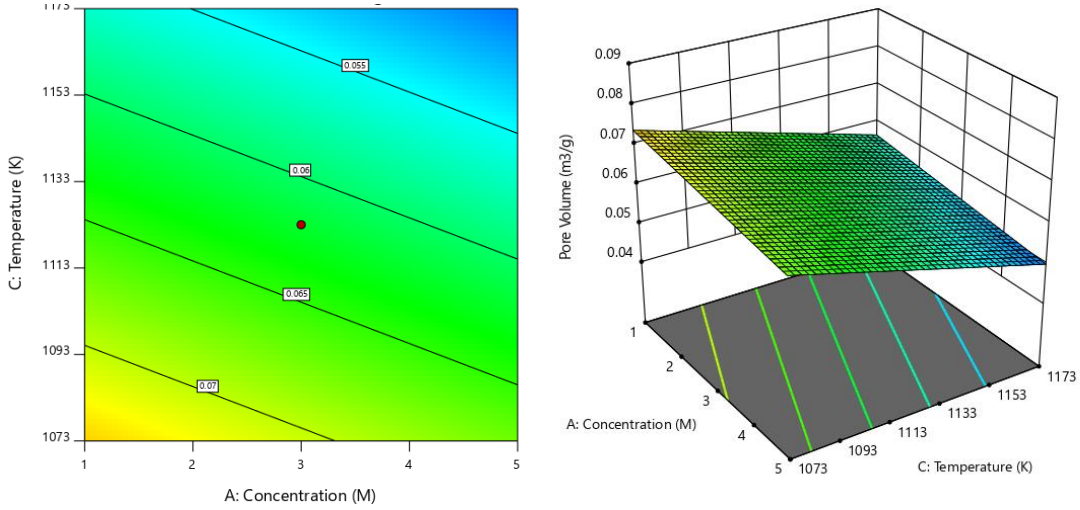
Figure 15: a) Predicted vs. actual plot; b) residual vs. run plot (factorial design)

Table 8: Analysis of variance for PV response (factorial design)

Source	**Sum of squares**	**df**	**Mean**	**F-value**	**P-value**
Model	67.8×10^5	2	33.9×10^5	6.3146	0.0428
A-Concentration	8.63×10^5	1	8.63×10^5	1.6089	0.2605
C-Temperature	59.1×10^5	1	59.1×10^5	11.0203	0.0210
Curvature	0.000154	1	1.54×10^5	2.8687	0.1511
Residual	0.000268	5	5.36×10^5		
Cor Total	0.0011	8			

The greater the F-value for each factor, the greater the effect of that variable on the response (Chitsiga, et al., 2018). Factor C yielded a P-value of 0.021 and F-value of 11.02 indicating a significant contribution to the model. An adequate precision value of 5.127 was calculated, representing the signal to noise ratio, a value greater than 4 suggests a signal of adequate strength to navigate the design space. A low coefficient of variance (C.V.%) such as the 12.12 % of the suggested model, indicates the good reliability and high precision in the suggested model.

The 2D contour plots (Figure 16a) and 3D response surfaces (Figure 16b) show the relation between independent synthesis factors and their interactions on the response. The contour plots and response surface shows a flat plane and linear lines due to the insignificance of the curvature term and absence of interactive effects. Lower aid strength and calcination temperature are suggested to produce higher pore volume of the SSOD samples.

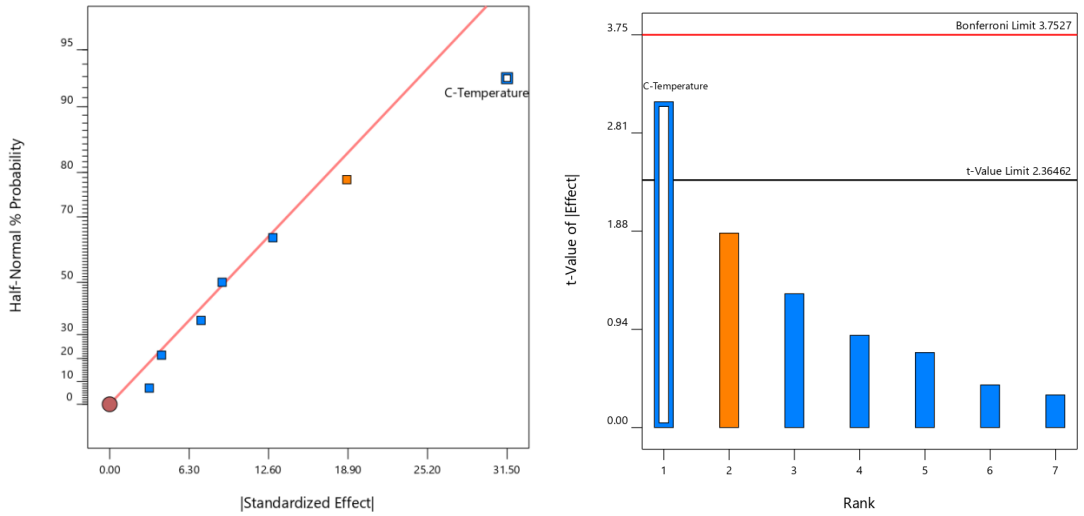


(a) (b)

Figure 16: a) contour and b) response surface plot for acid strength (A) and calcination temperature (C) at B= 95 min

Surface area regression model

Considering the half-normal and Pareto charts, only factor C was determined to be a potentially significant factor, falling to the right of the 45° linear line (Figure 17a) and below the Bonferroni limit with the remaining factors below the t-value limit (Figure 17b). No significant candidate models were produced utilizing factors A and B as both of these had high P values close to 1, both terms were removed from the model equation as having no significant effect on the SA response.

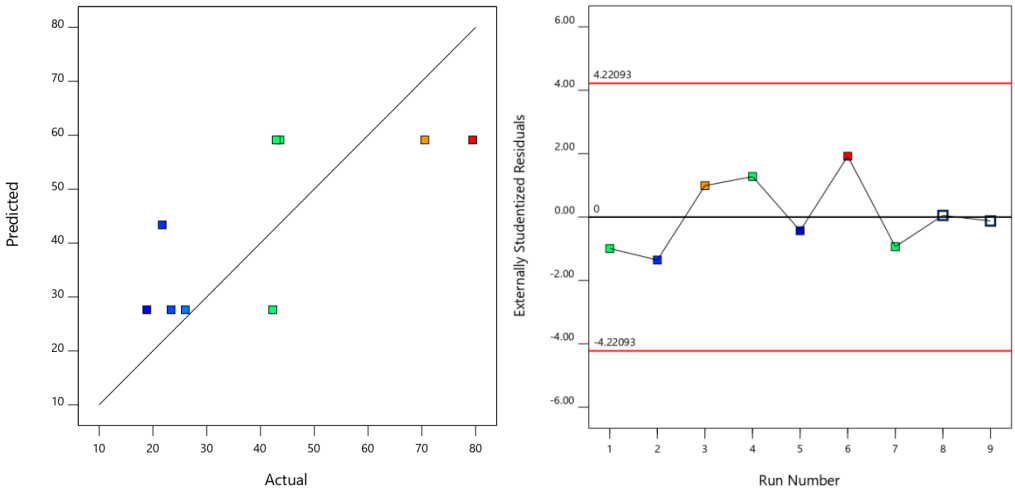


(a) (b)

Figure 17: a) half-normal; b) Pareto plots for SA model

The best empirical model suggested relating surface area to the topotactic synthesis variables is expressed in Equation 27. Although ANOVA results revealed this model to be significant with a P value = 0.0266 (P < 0.05, within a 95% confidence limit) and a sufficiently large F value, poor correlation was experienced between the predicted and experimental values (Figure 18a). This was quantified by an unsatisfactory R^2 = 0.53 indicating poor precision and reliability of the model. This is further confirmed by a large mean square error of 197.22 and a high coefficient of variance (C.V.%) of 38.9%. The plot of studentized residuals vs. run (Figure 18b) shows a lack of random scatter, failing to adequately confirm the independence assumption further indicating the unsatisfactory nature of this model in accurately predicting the sodalite surface area.

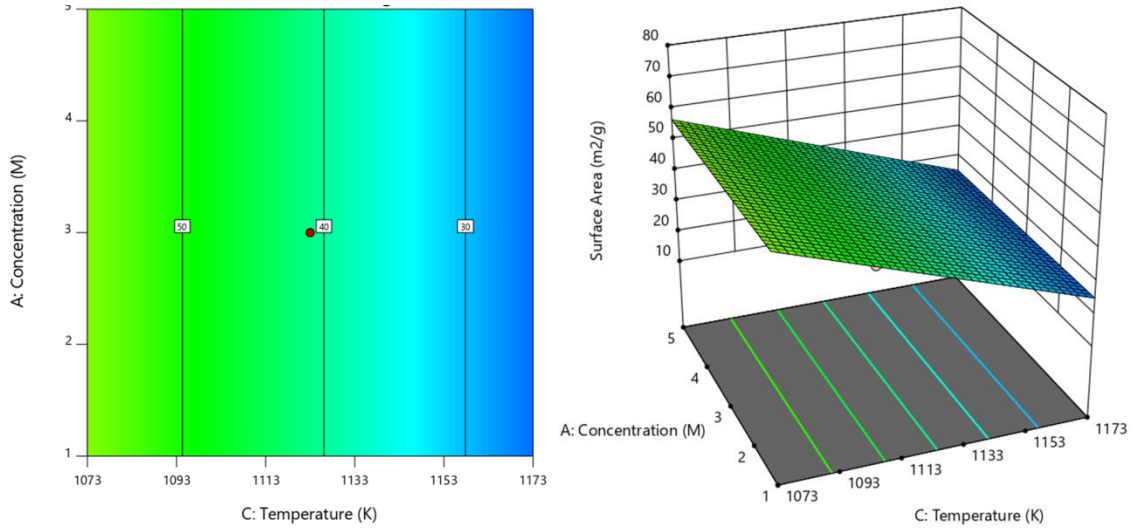
$$SA = 40.971 - 15.75C \pm 197.22 \qquad \text{Equation 27}$$



(a) (b)

Figure 18: a) Predicted vs. run plot and b) Residual vs. run plot for SA model (factorial design)

As only one factor (C) is utilized in the model (Equation 27) the RSM plots of the factors consist of vertical contours with respect to calcination temperature and linear 3D planes. Higher surface area is predicted at lower calcination temperature although the limits investigated do not extend to the maximum attainable surface area of approximately 79 m^2/g. This suggests that lowering the calcination temperature would be advantageous for higher quality SSOD production. This is potentially due to the further interlayer condensation and removal of organic matter that continues with increasing temperature, collapsing the sodalite cages and reducing the surface area of the particles (Moteki, 2011).



(a) (b)

Figure 19: a) Contour and b) response surface plot for acid strength (A) and calcination temperature (C) at B= 95 min

Optimization

Optimization was conducted utilizing the models expressed in Equations 26 and 27, keeping all factors within the specified limits and maximizing both the surface area and pore volume responses. The results obtained are shown in Table 9.

Table 9: Solutions for optimum design variables for preliminary investigation

Number	Acid Concentration (M)	Time (min)	Temperature (K)	Surface Area (m^2/g)	Pore Volume (cm^3/g)	Desirability
1	1.000	95	1073	56.719	0.074	0.704
2	1.016	95	1073	56.719	0.074	0.703
3	1.000	95	1074	56.535	0.074	0.701
4	1.000	95	1074	56.431	0.074	0.699
5	1.402	95	1073	56.719	0.073	0.695
6	1.000	95	1075	56.163	0.073	0.695
7	1.786	95	1073	56.719	0.073	0.687
8	2.011	95	1073	56.719	0.072	0.682
9	3.188	95	1073	56.719	0.070	0.656
10	3.700	95	1073	56.719	0.069	0.645

Modelling the BET surface area and pore volume results proved challenging as a precise, reliable model could not be produced for the surface area and pore volume responses utilizing all of the synthesis factors. Factor B- acid treatment time was identified as an insignificant

model factor in both preliminary models and was suggested to be removed from future investigations. Consequently, the investigation was extended to replace the acid treatment time with calcination time and extend the range of calcination temperatures investigated to potentially produce higher quality SSOD.

4.3.2.2 Extended investigation

RSM was used to explain the main and interactive effects of the process variables; propionic acid strength (A), calcination time (B) and calcination temperature (C).

Pore volume regression model

Linear, factor-interaction, quadratic and cubic models were developed and analysed to determine the model with the best fit to experimental data, a summary of these result is tabulated in Table 10. The cubic model was aliased with an inadequate number of experimental runs and the remaining models were insignificant (P-value > 0.05). A linear model was suggested and the model equation (Equation 25) was adapted to produce a significant model (Equation 28) by removing factor B- calcination time. In all candidate models this factor held a high P-value (0.1> P> 0.05) and was determined to not have a significant effect on the response.

Table 10: Model summary statistics for PV response

Source	SOS	df	Mean square	R^2	F-value	P-value
Linear [a]	0.0034	9	0.00038	0.402	1.2010	0.5342
2FI	0.0028	6	0.00047	0.490	1.4891	0.4545
Quadratic	0.0025	3	0.00084	0.539	2.6252	0.2878
Cubic [b]	0	0		0.907		
Pure Error	0.0006	2	0.00032			

[a] Suggested, [b] aliased

$$PV = 0.1744 + 0.0035A - 1 \times 10^{-4}C \pm 0.003 \qquad \text{Equation 28}$$

A one-way ANOVA test was performed to analyse the statistical significance of the model on the pore volume of silica sodalite. A model P-value of 0.048 was produced (P < 0.05) within a 95% confidence interval, indicating the statistical significance of the model while the lack of fit was calculated to be insignificant relative to the pure error with an F-value of 1.09 (Table 11). Factor C- calcination temperature is shown to be a significant model term as per the preliminary investigation with a P-value of 0.023 and a sufficiently large F-value of 6.79.

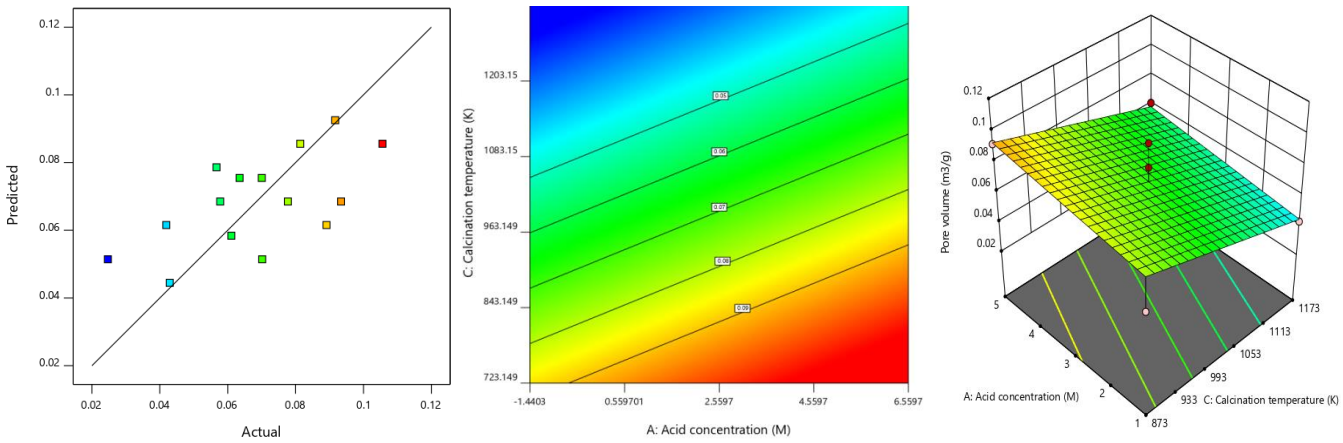
An R^2 value of 0.398 was produced. This value does not support good correlation between the experimental and predicted values. Consequently, 60.2 % of the total variation was left

unexplained by the model as can be seen by the large spread of data around the regression line in Figure 18a. The large standard deviation of 0.019 and C.V% of 27.02 % further indicate the poor precision of the model.

Table 11: Analysis of variance for PV response (BBH design)

Source	SOS	df	Mean square	F-value	P-value
Model	0.0027	2	0.0014	3.96	0.048
A-Acid concentration	0.0004	1	0.0004	1.13	0.309
C-Calcination temperature	0.0023	1	0.0023	6.79	0.023
Residual	0.0041	12	0.0003		
Lack of Fit	0.0035	10	0.0003	1.09	0.569
Pure Error	0.0006	2	0.0003		
Cor Total	0.0068	14			

The 2D contour plot in Figure 20b shows the relationship between model factors A and C and the pore volume response. Lower calcination temperature and higher acid strength are favourable for high porosity sodalite production. This corroborates results by Moteki et al (2011) who concluded higher acid strength up to 6 M propionic acid to be favourable for the synthesis of SSOD without the presence of occluded matter. This can also be seen by the inclined linear plane of the 3D response surface (Figure 20c). A lack of curvature can be seen in the design space. As factor B was not included in the model this term has no effect on the model graphs and plots including factor B contain vertical contours and linear response surfaces.



(a) (b) (c)

Figure 20: Model graphs a) Predicted vs actual results; b) 2D Contour plot of model terms A and C at B= 3h; c) 3D response surface for model terms A and C at B=3h

Surface area regression model

As per the pore volume model above, multiple candidate models were assessed to determine the model with the best fit to experimental data. Table 12 summarises the results from the lack of fit tests conducted. The cubic model was aliased while the quadratic model was insignificant with many insignificant terms. A 2 factor-interaction (2FI) model was suggested and identified to have three significant model terms; A- acid strength, C- calcination temperature and the interaction AB- acid strength and calcination time. Equation 29 was developed as a suitable model equation from Equation 25.

Table 12: Model summary statistics for SA response

Source	**SOS**	**df**	**Mean square**	**R^2**	**F-value**	**P-value**
Linear	6548	9	728	0.475	2.187	0.353
2FI [a]	2438	6	406	0.774	1.222	0.515
Quadratic	2146	3	715	0.795	2.151	0.333
Cubic [b]	0	0		0.952		
Pure Error	665	2	333			

[a] Suggested, [b] aliased

$$SA = -65.95 + 69.75A + 37.25B + 0.058C - 7.31AB - 0.038AC - 0.022BC \pm 206.9$$

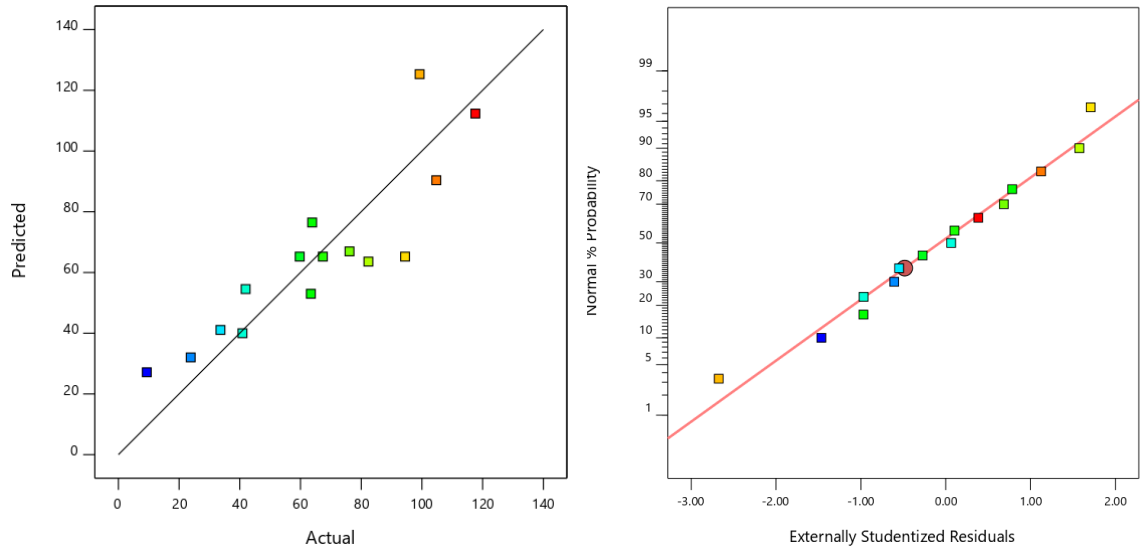
Equation 29

An ANOVA analysis was conducted on the suggested model. The 2FI model suggested produced a significant model with a P-value of 0.0263 (Table 13) and an F-value of 4.57, leaving only a 2.63 % chance this may be attributed to noise. None of the model terms were identified as in-significant. An R^2 value of 0.77 was calculated, indicating a good correlation between the model and experimental data. In addition, the lack of fit value was found to be insignificant relative to the pure error, suggesting the model adequately represents the design space. The cluster of point around the regression line can be seen in Figure 21a, 22.6 % of the total variation was left unexplained by the model. The normal plot of residuals (Figure 21b) indicates a normal distribution with minor deviations from the linear line thus, supporting the normality assumption. The C.V.% was surprisingly high reaching 30.2 % (C.V.% > 30%) indicating possible issues with precision and reliability of the data however, an adequate precision value representing the signal to noise ratio of 7.3 was observed. As the value is greater than 4 the signal was determined to be of acceptable strength to navigate the design space.

Table 13: Analysis of variance for SA response (BBH design)

Source	SOS	df	Mean square	F-value	P-value
Model	10 631	6	1 772	4.57	0.026
A-Acid concentration	2 430	1	2 430	6.26	0.037
B-Calcination time	1 444	1	1 444	3.72	0.090
C-Calcination temperature	2 648	1	2 648	6.83	0.031
AB	3 416	1	3 416	8.80	0.018
AC	526	1	526	1.36	0.278
BC	167	1	167	0.43	0.530
Residual	3 104	8	388		
Lack of Fit	2 438	6	406	1.22	0.515
Pure Error	665	2	333		
Cor Total	13 735	14			

The remaining diagnostic graphs can be seen in Appendix C, where all the residual plots fall within the specified limits. SSOD 2 approaches the limit for Cook's distance and may be considered an outlier as its difference in Beta and difference in fit falls below the minimum level for the intercept.



(a) (b)

Figure 21: a) Predicted vs actual values; b) Normal plot of residuals

The 2D contour plots and corresponding 3D response surfaces for the suggested model are shown in Figure 22. All of the graphs show a hyperbolic paraboloid (saddle) shape which can be seen more clearly in the AB graph as opposed to the AC or BC graphs due to the location of the experimental points included. This shape displays increasing surface area on two opposing ends

of the plane while the other two are shown to decrease. Curvature due to the interaction of model terms can be seen in the contour plots of AB, AC and BC.

Factors A, C and AB were identified as significant model terms and the effect of this can be seen in the graphs. Graphs of AB show the strong interaction between the factors. Surface area is seen to increase at low acid strength with high calcination time as well as at high acid strength and low calcination time. The later of the two shows greater surface area as factor A is significant and has a dominant effect over factor B. In the AC graphs, higher SA is again produced at increased acid concentrations, with lower calcination temperatures being favourable. This result is supported by the BC graph with Factor B having little effect on the response as shown by small change in SA in the horizontal direction at low calcination temperature.

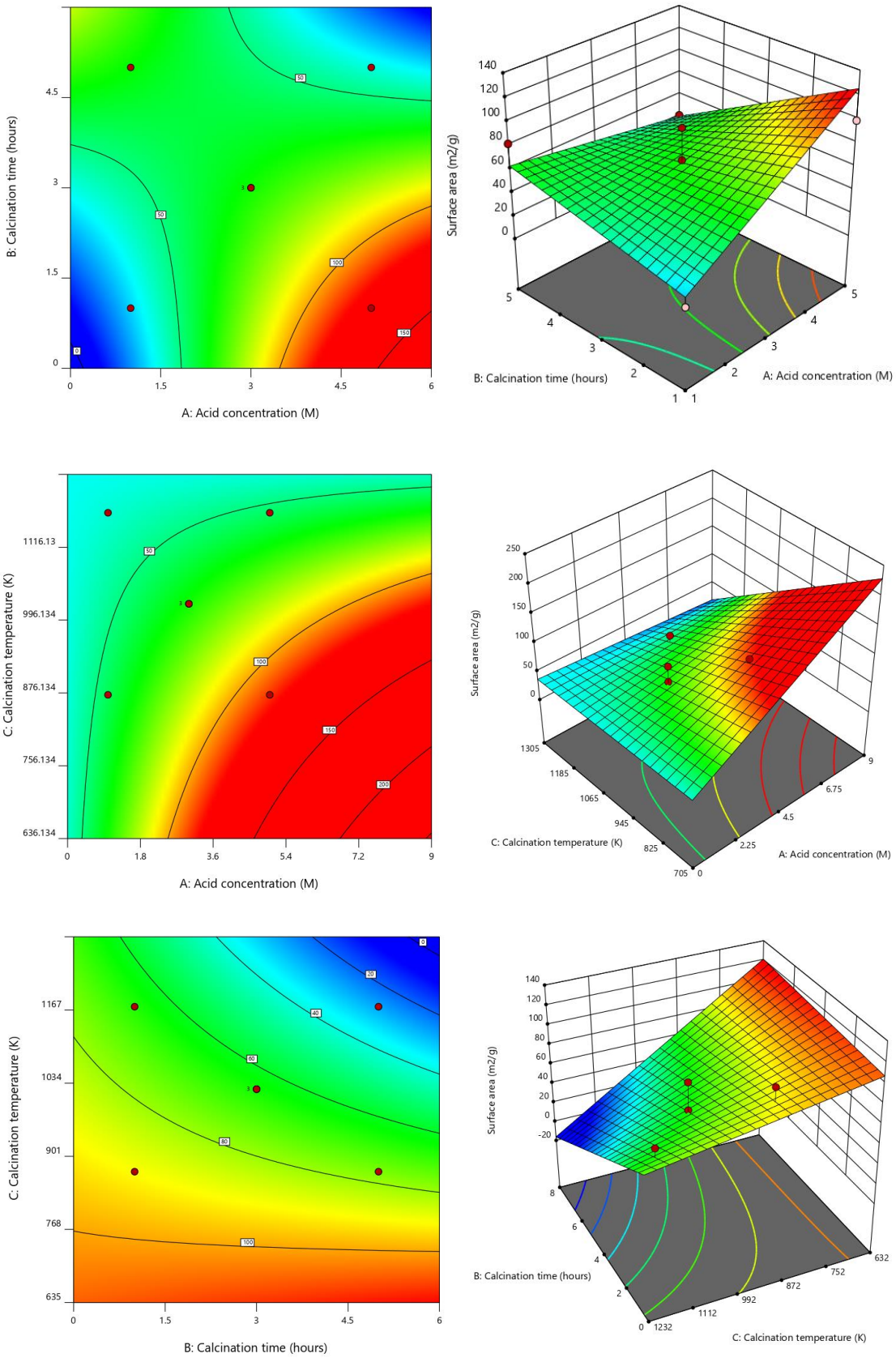


Figure 22: 2D contour plots and 3D response surfaces for model factors A, B and C (third factor not shown is at an intermediate level in each case).

Optimization

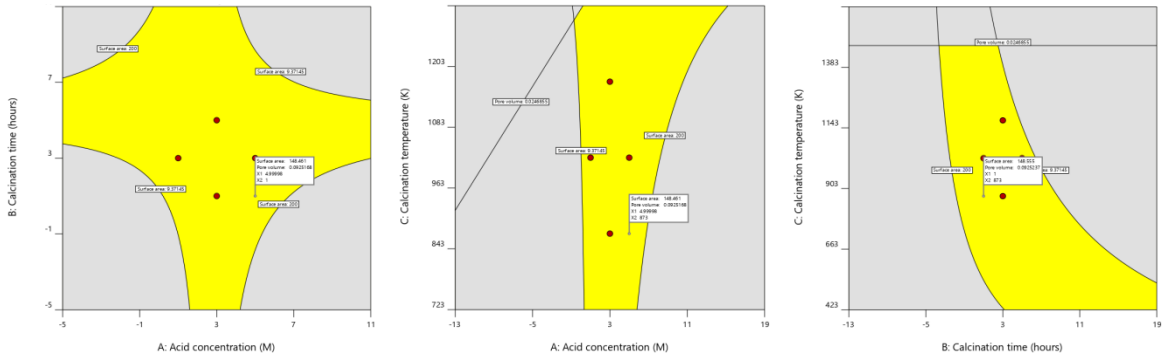
Optimization was conducted using the PV and SA models developed under the extended investigation using Design Expert v11 (Stat-Ease, USA). Factor A was kept within the limits; B and C were minimized to reduce the energy demands of the synthesis while the SA and PV responses were maximized. A total of 57 results were produced of varying desirability and the first 10 are presented in Table 14. Solution number 1 (5 M, 1 h and 873 K) was selected as this could potentially produce the greatest SA and PV at the low limits of calcination time and temperature, thereby reducing the energy requirements of the synthesis process.

Table 14: Solutions for optimum design variables for extended investigation

Number	Acid concentration (M)	Calcination time (hours)	Calcination temperature (K)	Surface area (m^2/g)	Pore volume (cm^3/g)	Desirability
1*	5	1	873	148.518	0.0930	0.957
2	4.98	1	873	147.944	0.0920	0.957
3	4.967	1	873	147.55	0.0920	0.956
4	5	1.015	873	148.241	0.0930	0.956
5	4.917	1.001	873	146.096	0.0920	0.956
6	5	1	874	148.331	0.0920	0.955
7	4.867	1	873	144.64	0.0920	0.955
8	4.847	1	873	144.083	0.0920	0.955
9	5	1.04	873	147.796	0.0930	0.955
10	4.797	1	873	142.624	0.0920	0.954

* chosen optimization values

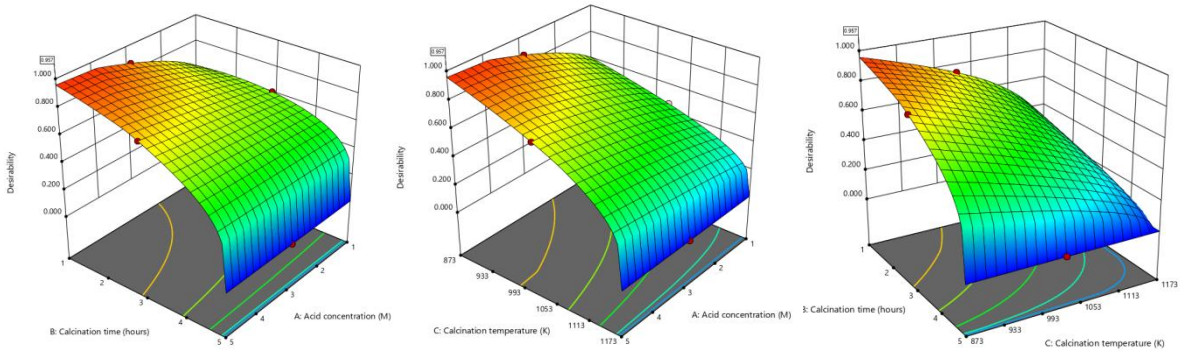
The overlay plots of factors A, B and C at optimized conditions, show large feasible regions but focuses on the desired solution to maximize SA and PV (Figure 23). Further increasing the acid strength may be beneficial however further investigation would need to be conducted as Moteki et al (2011) found amorphous layers due to the miss-alignment of silicate layers when treated with 6M propionic acid. There is also potential to further decrease the calcination temperature but the effects of this on the crystallinity of the samples would need to be studied.



(a) (b) (c)

Figure 23: Overlay plots for model factors; a) A&B, b) A&C and c) B&C at optimum conditions

The 3D desirability responses are shown in Figure 24. The graphs reach a sharp drop at high calcination time and temperature where the effects of changing acid concentration and calcination temperature are diminished. The desirability plateaus at 0.957 where the highest potential SA and PV are reached. Due to the poor precision and reliability of the models produced, synthesis at the optimum conditions is unlikely to produce the predicted values, but synthesis at these conditions should improves the efficiency of the process with reasonable increases in SSOD quality.



(a) (b) (c)

Figure 24: 3D desirability responses for optimization of factors; a) A&B, b) A&C and c) B&C

4.3.3 Validation an analysis of optimized sodalite

4.3.3.1 Textural properties

SSOD was synthesized in triplicate according to the optimum conditions specified in Chapter 4.3.2 (5 M, 1 h and 873 K). Multipoint BET analysis was conducted on the optimized sodalite samples and the summarized results are displayed in Table 15. The average SA and PV produced through synthesis at the optimum conditions was 27.43 m^2/g and 0.084 cm^3/g. This equates to an 81.5% and 9.5% error between the experimental and predicted values for SA and

PV, respectively. Despite the poor accuracy of the model in predicting the SA of the optimized sample, this SSOD still displays improvements of 12X that of the standard hydrothermally synthesized HSOD.

Table 15: BET results of optimized SSOD

	BET results			Relative to HSOD		
	Surface area	Pore volume	pore size	Surface area	Pore volume	pore size
	m^2/g	cm^3/g	nm	m^2/g	cm^3/g	nm
OPT 1	28.80	0.0888	12.04	12.3	7.46	1.7
OPT 2	28.51	0.0899	8.89	12.2	7.56	2.3
OPT 3	26.82	0.0629	9.21	11.4	5.28	2.2
St. dev	0.94	0.0189	1.64	-	-	-
Average	27.43	0.0842	11.38	12.0	6.77	2.1
SSOD m	56.56	0.1810	12.63	24.1	15.21	1.6

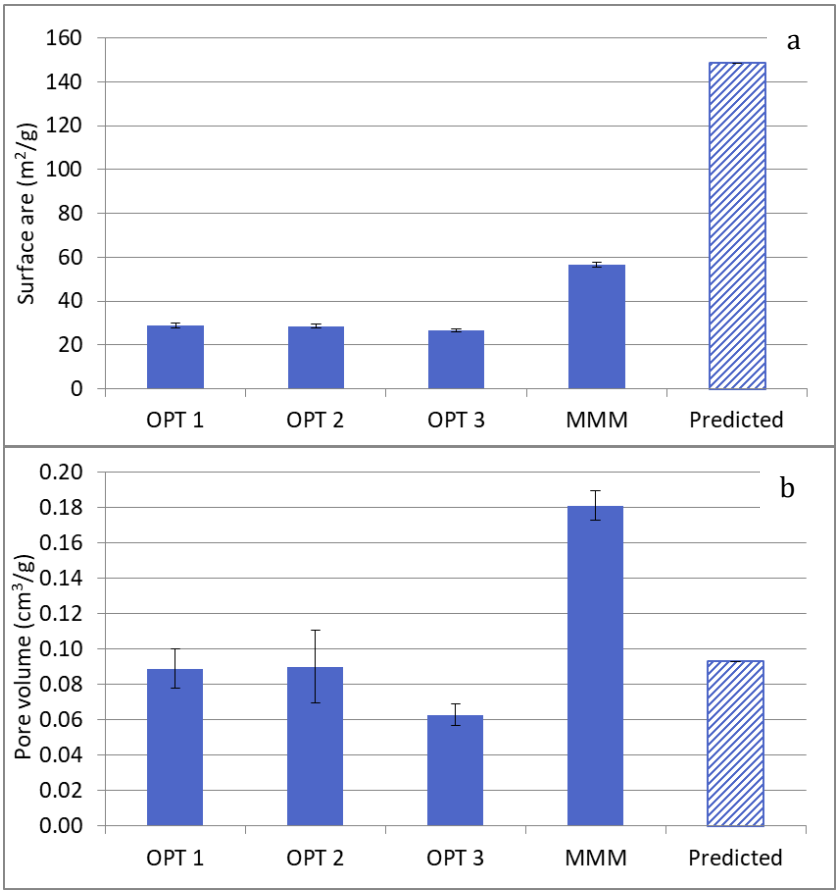


Figure 25: a) SA and b) PV results for optimized SSOD

The adsorption isotherms for these SSOD samples are characteristic of type 4 isotherms of mesoporous solids (5-50 nm) (Figure 26). The graphs depict multi-layer adsorption at low relative pressures followed by capillary condensation limiting the uptake at high pressures. This is due to high interactions between the adsorbate molecules and weak interactions between the

adsorbate and the surface. A hysteresis loop (H4) is clearly seen in OPT1 and OPT3, these isotherms are typical of plate-like particles which form narrow slit like pores with internal voids of various size and shape, where the walls consist of ordered mesoporous silica (Sing, 1985; Zhang, 2016). OPT2 does not show complete desorption of nitrogen potentially due to the pore network effect as indicated by the slight bump at a relative pressure between 0.4 and 0.6. Blocked or encapsulated mesopores which should desorb through capillary evaporation at lower pressures remain occupied in this sample. This may be due to the reduced pore size of OPT2 as compared to OPT1 and OPT3, where large interconnected voids within the sample connect to a smaller external pores limiting the desorption of gas (Groen et al, 2003).

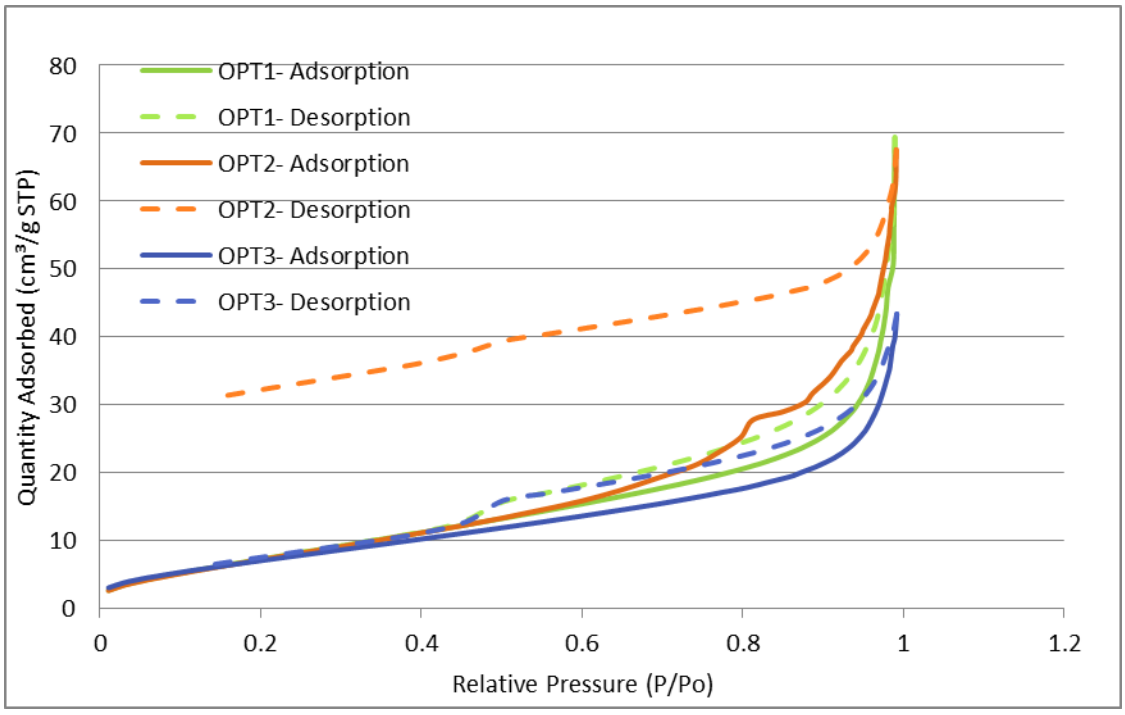


Figure 26: Adsorption isotherms for optimized SSOD

The synthesized RUB-15 has a considerable impact on the resulting quality of SSOD produced as shown in earlier investigations. The SSOD synthesized from the third batch of RUB-15 and treated under optimal conditions for later use in mixed matrix membranes ($SSOD_m$), held a SA and PV approximately twice that of the optimum samples. While the SA of 55.77 m^2/g falls below the predicted model value of 148.5m^2/g, the PV of 0.181cm^3/g is approximately double the 0.093 cm^3/g of the predicted optimized results (Figure 25). The adsorption isotherm shows the same type 4 isotherms as the optimized SSOD with the same hysteresis loop (H4) common to mesoporous plate-like particles with elongated slit pores (Figure 27).

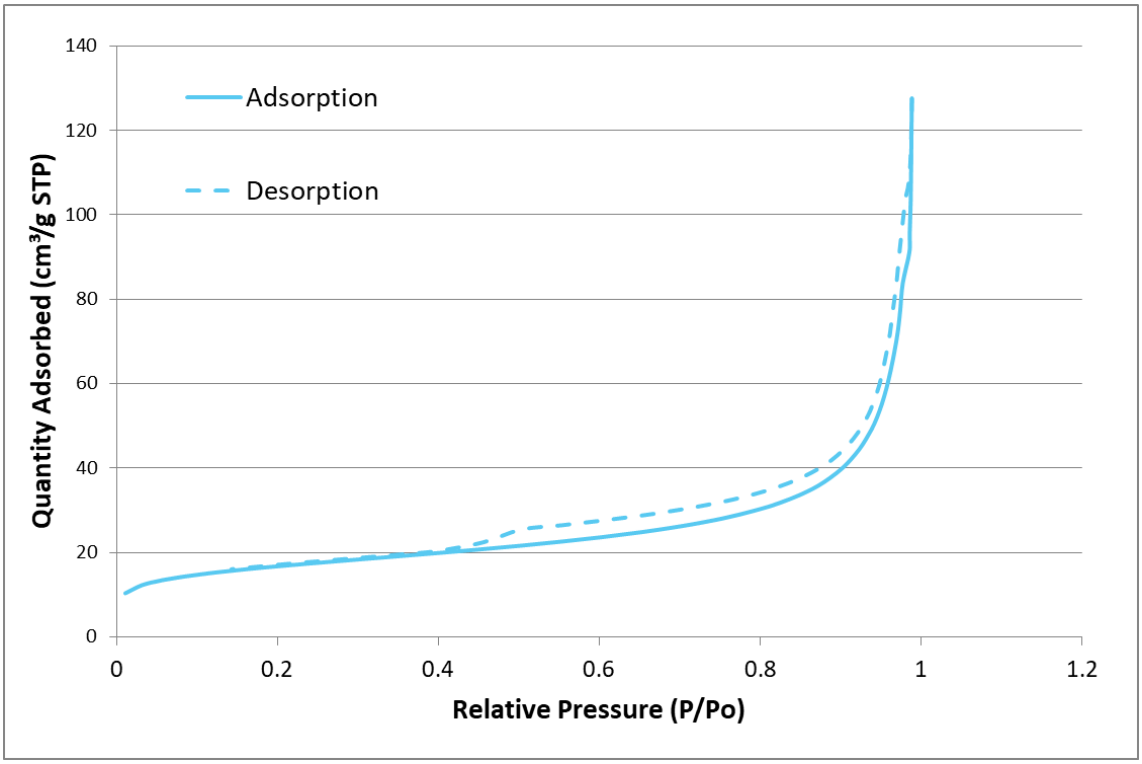


Figure 27: Adsorption isotherm for $SSOD_m$

4.3.3.2 Physio-chemical characterization

Powder X-ray diffraction (XRD)

The XRD patterns for the optimized sodalite OPT2 and OPT3 (Figure 28e and f) show good crystallinity and the presence of the characteristic diffractions peaks (International Zeolite Association, 2007), three with reasonable intensity. The patterns are smooth and show an absence of noise. The pattern for OPT1 shows an increase in noise and the presence of an amorphous phase as indicated by the hump between 17° and 22°. Notably, these patterns are similar to those produced in the extended investigation, with OPT 2 and OPT 3 showing similar crystallinity to SSOD 6 (in the extended investigation).

The RUB-15 synthesized for $SSOD_m$ shows superior crystallinity with an initial peak of high intensity followed by the majority of the peaks displayed by Oberhagemann et al. (1996) and Kooli et al (2016), see Appendix A.4 for reference graphs. The resulting sodalite mirrors the high crystalinity of the precursor displaying the IZA characteristic diffraction peaks and minimal noise. This suggests a suitable degree of ion exchange and the stabilization of intermediate structures during the synthesis process through the intercalation of TMA^+ cations and propionic acid (Moteki et al, 2011).

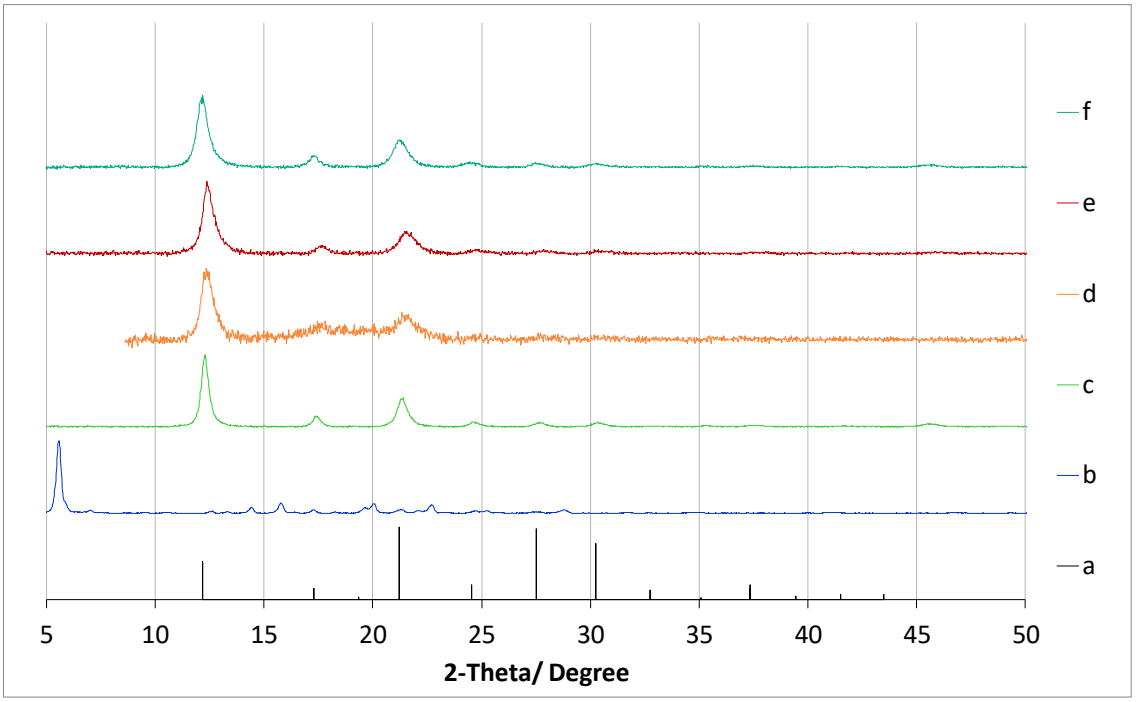


Figure 28: XRD patterns for a) simulated IZA standard; b) RUB-15 (MMM); c) SSOD m; d) OPT 1; e) OPT 2; f) OPT 3

Scanning electron microscopy (SEM)

The SEM images for the optimized sodalite samples can be seen in Figure 29. OPT1 and OPT2 show a plate-like morphology with sharp rectangular layers. Clusters of the amorphous phase can be seen throughout the images with a greater presence in OPT1 which relates to the lower crystallinity displayed in the XRD. OPT3 in Figure 28c, displays the same morphology as SSOD9 (Figure 11c), with small irregular flakes scattered on to thin layered sheets producing a bark like morphology. $SSOD_m$ (Figure 29d) shows the more common plate-like morphology produced in this study, with irregular sized plates of ragged edges layered on top of one another.

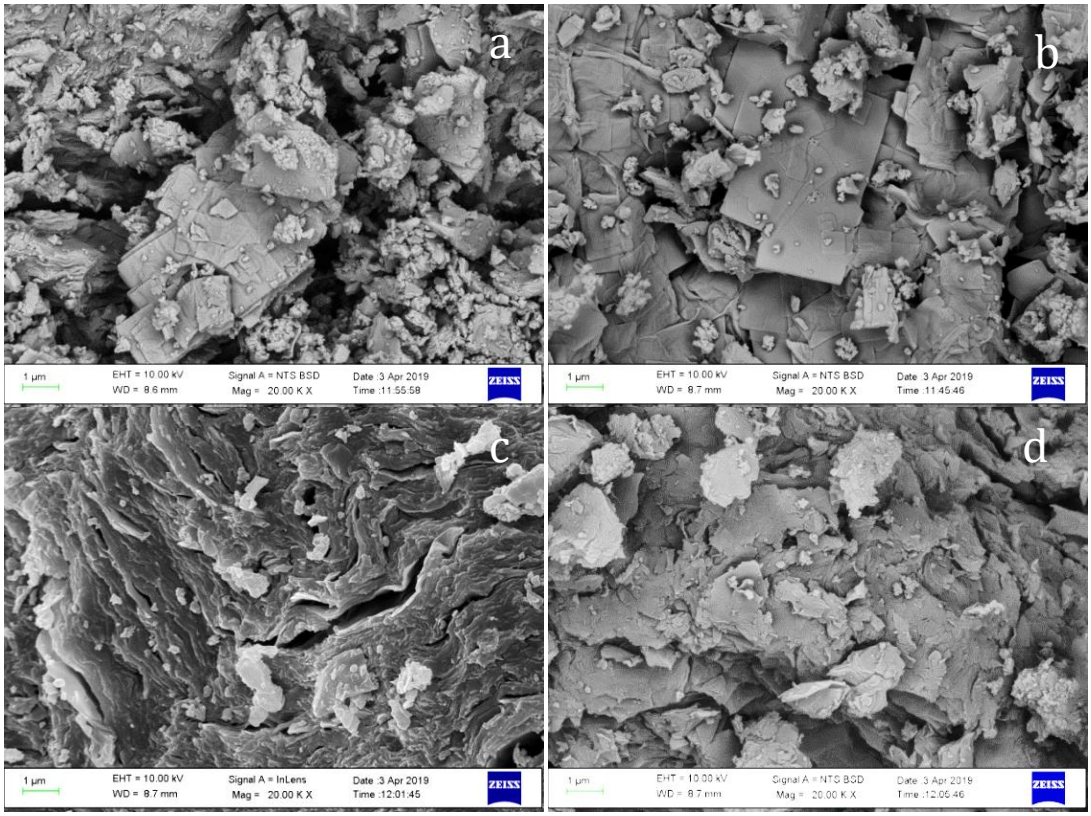


Figure 29: SEM imaging for optimized SSOD; a)OPT1; b)OPT2; c)OPT3 and d)SSODm

Fourier Transform Infrared Spectroscopy (FTIR)

The optimized silica sodalite reproduction to be used in the mixed matrix membranes ($SSOD_m$) shows the absence of both occluded TMA^+ cations as well as water molecules (Figure 30) increasing the potential of this material to improve the separation performance of the polysulfone mixed matrix membranes by allowing small molecules such as H_2 to pass through the cage structure. The optimized samples (OPT 1-3) show a notable intensity for the absorption band due to C-H deformation vibrations (Coates, 2006).

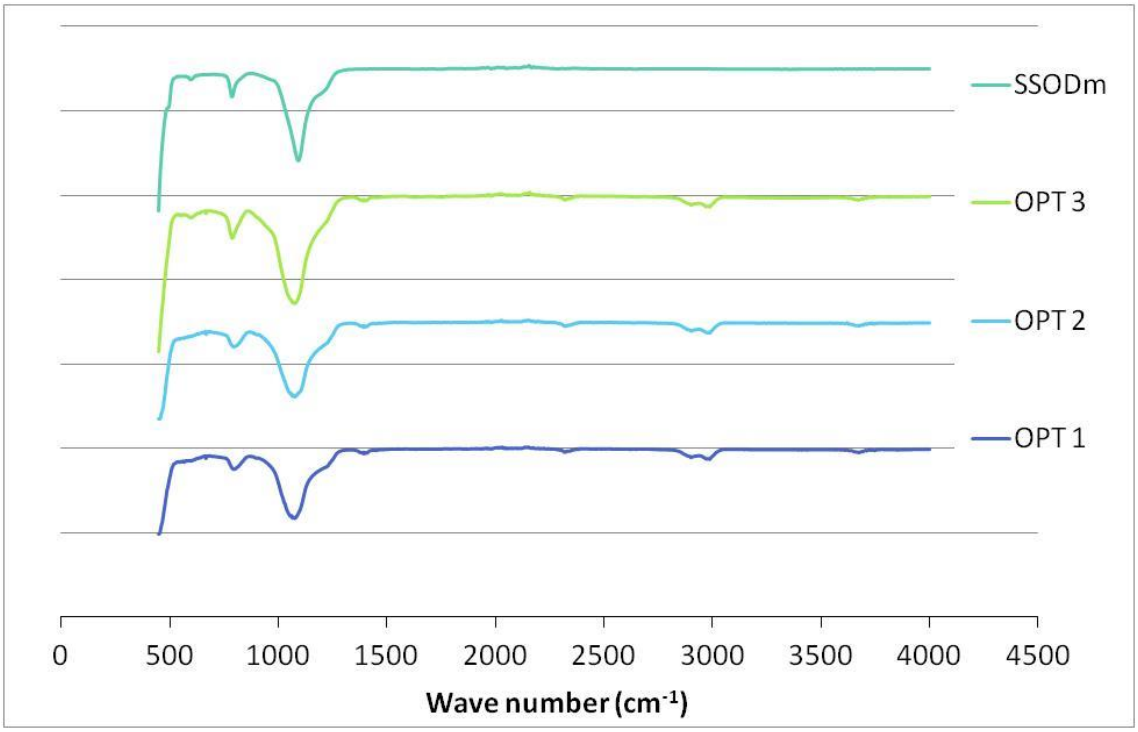


Figure 30: FTIR absorption spectrum for optimized silica sodalite

Thermogravimetric analysis

Thermogravimetric analysis (TGA) of $SSOD_m$ after calcination at 873K for 1 hour shows relatively good thermal and oxidative stability with a total weight loss of only 5.46 % up to a temperature of 900 °C (Figure 31). The onset of desorption of physically absorbed moisture can be seen around 30 °C, highlighted by the endothermic derivative weight loss peak. The removal of small amounts of occluded water molecules is known to occur between 140 and 180 °C and is shown by a gentle weight loss slope indicating minimal weight change and the absence of occluded water (Moteki et al, 2011). A steady weight loss is seen between 147 and 245 °C, indicating minimal condensation of the silanol groups on adjacent layers (Moteki, et al., 2008). Further increasing the temperature above 245 °C initiates the decomposition of interlayer propionic acid. The removal of occluded organic matter results in the collapse or transformation of the cage structures due to the small aperture of the sodalite cages (Münzer, et al., 2008). Moteki et al (2011) noted that uncondensed sited remained until all organic matter was completely removed from the interlayer spaces (up to approximately 800 °C). In this study minimal weight loss of 3.62 % is experienced up to 570 °C. This suggests the absence of large volumes of occluded organic matter after calcination of the SSOD. Sharper weight loss was experienced above 570 °C likely due to the collapse and/or transformation of cage structures by the removal of propionic acid and the formation of CO_2. As the material was calcined 600 °C it is consistent to think that additional decomposition of organic material would continue at a faster

rate beyond this point. The derivative weight loss curve shows a sharp endothermic peak at 570 °C, suggesting the onset of thermal decomposition of organic material. These particles would be suitable for use in high temperature applications up to approximately 550 °C, such as adsorption and separation in pre-combustion carbon capture as minimal weight loss and change in structure can be seen up to this point. The TGA data of the synthesized silica sodalite is comparable to that of pure silica sodalite Si/Al→∞ (Zheng et al, 2009; Vaezi & Babaluo, 2014).

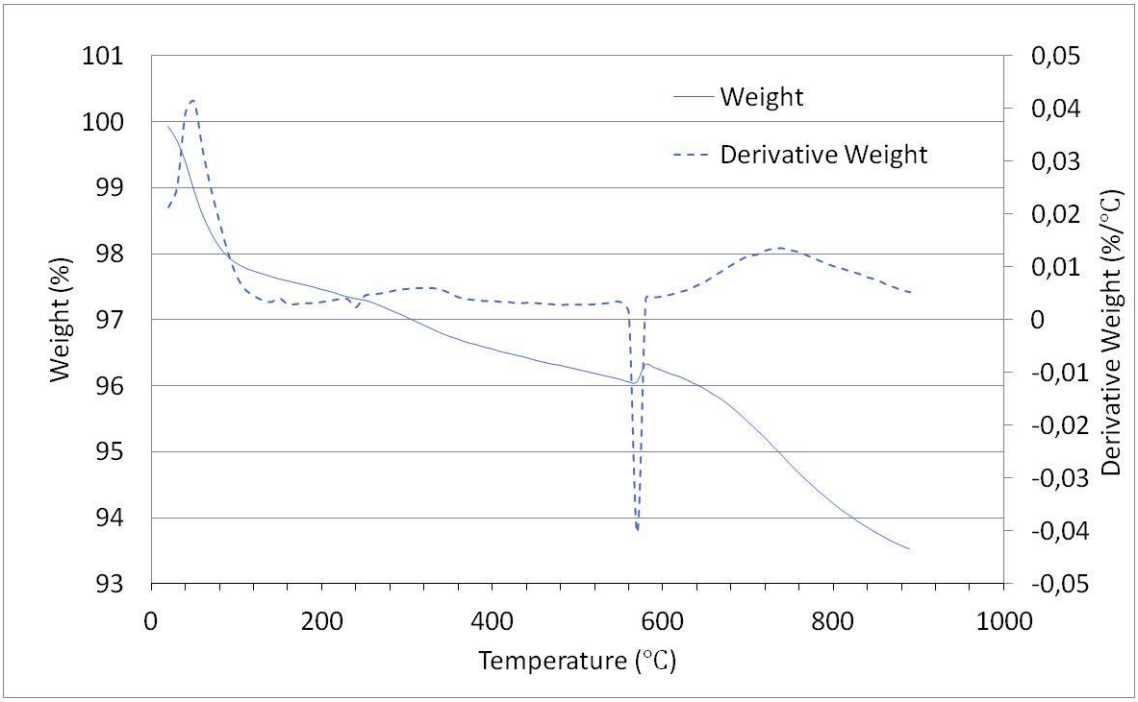


Figure 31: TGA results for SSODm

Particle Size Analysis

Particle size analysis was conducted on the sodalite particles and found to be mostly microparticles with 60% volume of particles falling between 5.7 and 17.3 µm (Figure 32). An average distribution size (d50) of approximately 10.25 µm was determined through interpolation of the nearest values. The distribution possessed a maximum particle size of 53 µm.

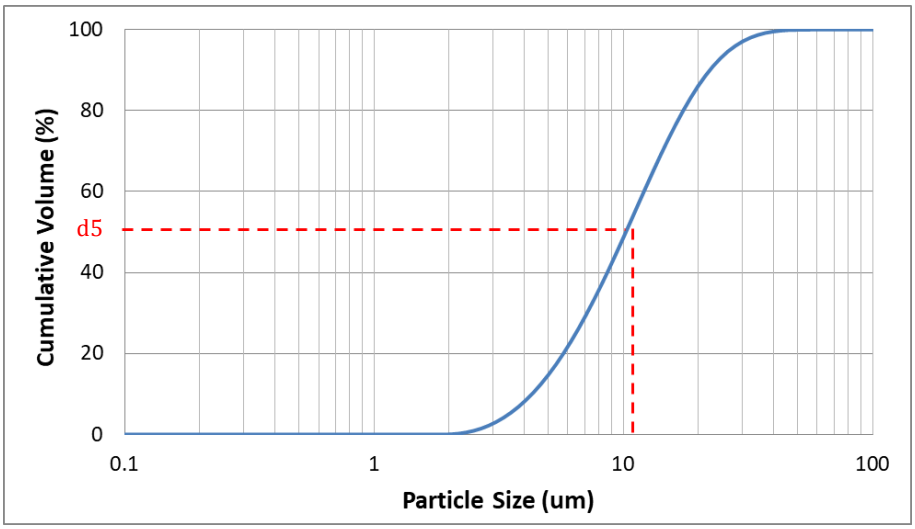


Figure 32: Particle size distribution curve

4.4 Concluding remarks

The investigation documented in this chapter was undertaken to investigate three crucial topotactic synthesis parameters as identified by previous researchers; acid strength, acid treatment time and calcination temperature. Due to the unsatisfactory nature of the experimental data obtained, this study was reduced to a preliminary investigation. The experiment was extended to investigate the effect of synthesis parameters; acid strength, calcination time and calcination temperature which were identified during the preliminary investigation.

The surface area and pore volume of the synthesized SSOD far exceeded that of the hydrothermally synthesized HSOD of 2.3 m^2/g and 0.012 cm^3/g.. The SSOD produced a high surface area and pore volume reaching a maximum SA and PV of 160.9 m^2/g and 0.115 m^3/g, respectively. SEM imaging showed a plate like morphology confirming the successful topotactic synthesis with the absence of occluded matter.

The regression model for the 2^3 factorial design from the preliminary investigation reveals Factor B- acid treatment time to be an insignificant model factor in both SA and PV models and

suggested to be removed from future investigations. From the suggested pore volume model, low calcination temperature was favourable to produce high porosity SSOD. Utilizing Box-behnken design to produce more experimental points the SA and PV responses were modelled in the extended investigation. The pore volume response was best described by a linear model where calcination time (B) was removed as an insignificant model factor. For the surface area response, a factor-interaction model was chosen as the best fit to experimental data. These models showed regression coefficients (R^2) of 0.40 and 0.77, respectively. Calcination temperature was always seen to be a significant variable, favouring higher surface area and pore volume at lower calcination temperatures. Optimization, maximizing both the surface area and pore volume was conducted to produce optimum synthesis variables at 5 M propionic acid, 1 h calcination time and 873 K.

While the models developed and optimized in the extended investigation are a useful tool in understanding the impact of the synthesis factors investigated, this model cannot successfully be used as a predictive tool due to the two stage synthesis process. Large deviation in the quality of the RUB-15 synthesized means that a model considering only factors in the second stage is prone to errors and cannot be used to comprehensively understand the synthesis of the sodalite. However, high quality silica sodalite was able to be reproduced without the presence of occluded matter following the optimized parameters of 5 M propionic acid and 1 h calcination at 873 K. This silica sodalite will be further investigated in PSF mixed matrix membranes for H_2/CO_2 separation.

Chapter 5: The fabrication of silica sodalite/polysulfone mixed matrix membranes and evaluation in H_2/CO_2 separation

5.1 Introduction

This chapter focuses on the application of sodalite in mixed matrix membranes. Characterization of the SSOD/PSF mixed matrix membranes and the single and mixed gas permeation tests are discussed and compared to the results of HSOD/PSF membranes as well as mixed matrix membranes from literature.

5.2 Experimental

5.2.1 Synthesis and characterization

Silica sodalite and hydroxy sodalite synthesized in Chapter 4 were added as fillers to the fabrication of polysulfone mixed matrix membranes as described in Chapter 3.3.3 and characterized according to Chapter 3.4. The higher surface area and porosity of the SSOD were expected to equate to higher separation performance (Reible & Shair, 1982) with the small cage aperture forming a size selective separation.

5.2.2 Separation performance of fabricated membranes

The HSOD (5 wt. %) and SSOD (0, 5, 10, 15 wt. %) mixed matrix membranes were characterized according to Chapter 3.4 and utilized for pure and mixed gas separations as detailed in Chapter 3.5.4, utilizing a gas separation rig as describes in Appendix D.1, to investigate the effect of the higher porosity sodalite on the membranes H_2/CO_2 separation performance as well as the effect of increased silica sodalite loading on gas separation.

5.3 Results and discussion

5.3.1 Membrane Morphology

Scanning electron microscopy (SEM) imaging for the fabricated polysulfone mixed matrix membranes (PSF MMM) containing 5 wt. % HSOD and SSOD are shown in Figure 33 as compared to the pure PSF MMM. No particles were incorporated in the fabrication of the pure PSF MMM, small specs on the surface of the membrane are attributed to dust under the Au/Pd

coating. This membrane also displays light surface defects formed during the casting and drying process, however these are shallow and do not appear penetrate the selective layer of the membrane. Some explanation for these defects could be due to insufficient sonication and/or resting period to fully remove all miniscule air bubbles from the casting solution. The small indentations partly visible were a result of drying the membranes on the oven grid. Surface particles are visible on the surface of the 5wt. % SSOD/PSF and HSOD/PSF MMM's while no pores were visible under any magnification.

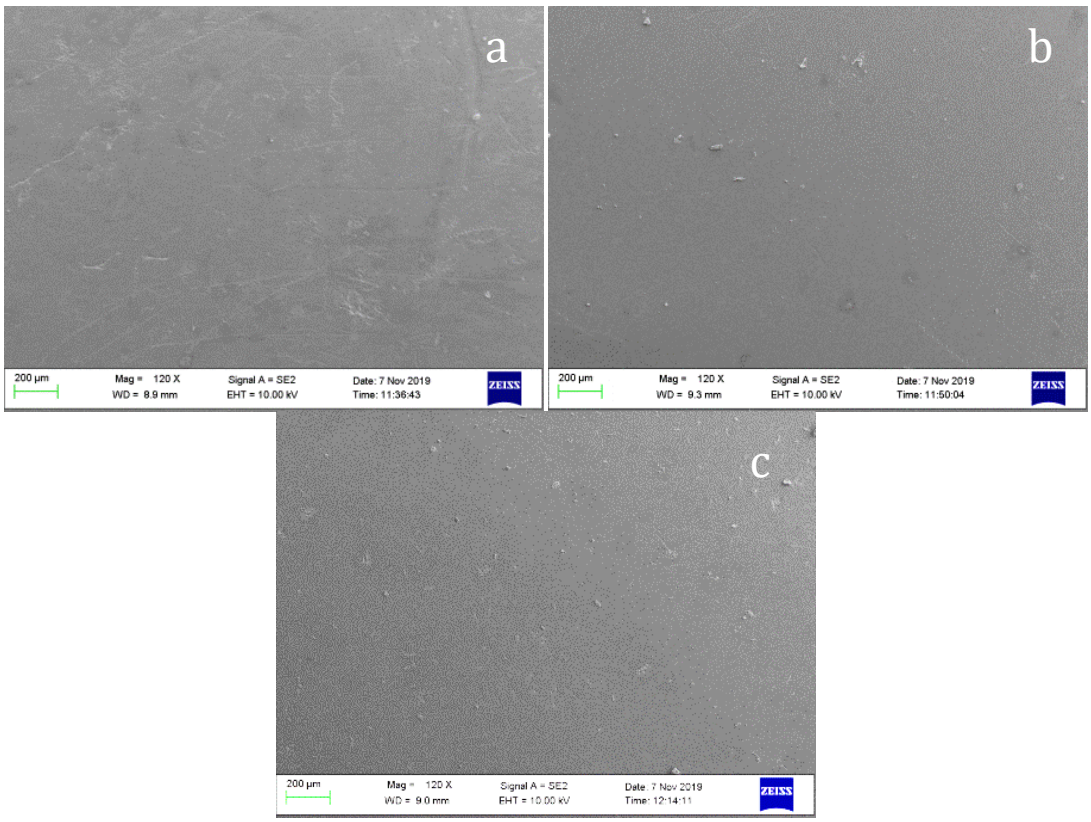


Figure 33: SEM images of membranes surface for a) purely PSF; b)5wt. % HSOD/PSF ; c) 5wt. % SSOD/PSF MMM's (Mag =120 X)

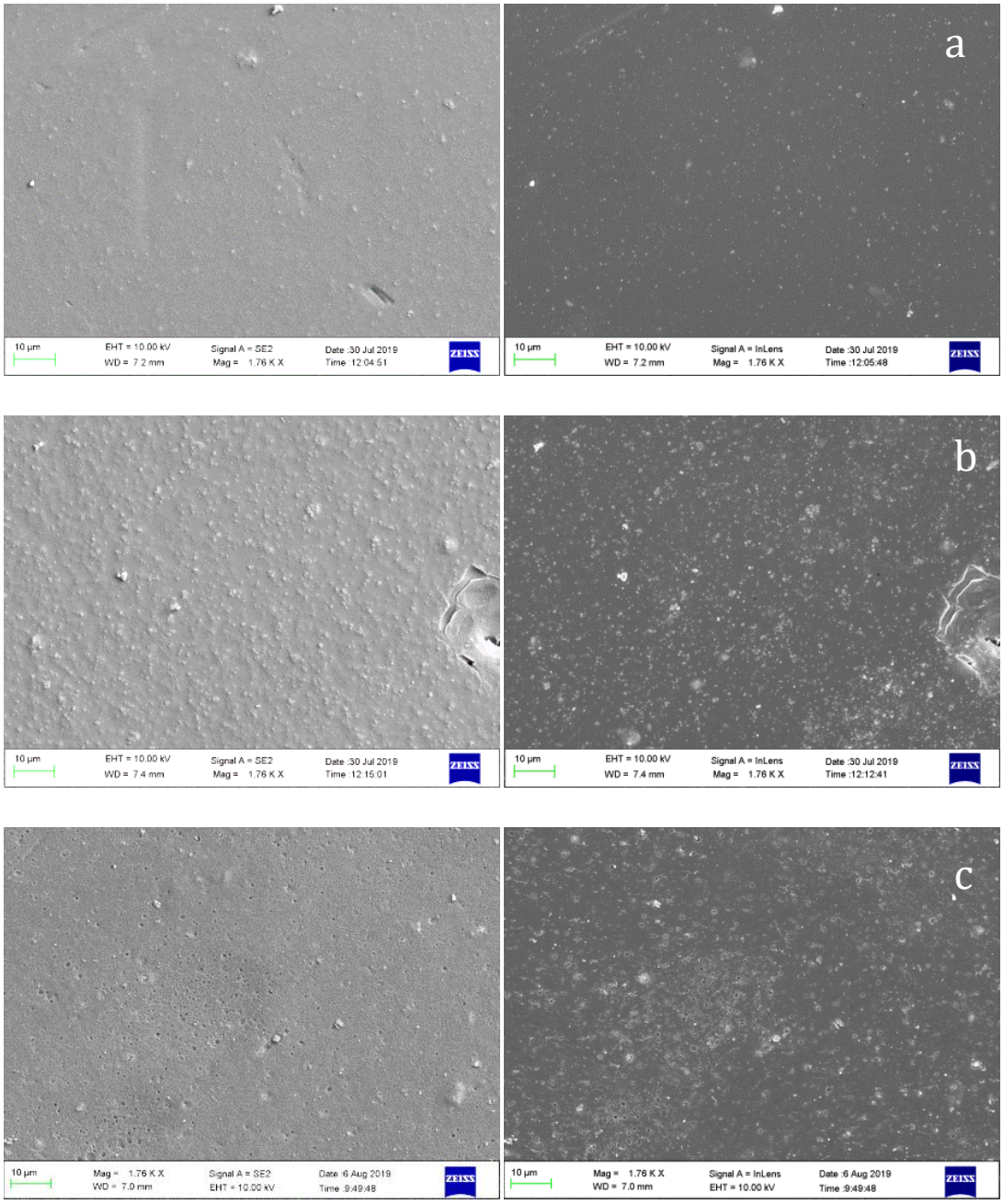


Figure 34: SEM images of membranes surface for SSOD/PSF MMM a)5 wt. %; b)10 wt. %; c)15 wt. % (Mag=1.76 kX) under SE2 (left) and InLense (right) detection.

A significant increase in the number of particles can be seen on the surface of the membrane as the SSOD loading is increased from 5 to 10 wt. % (Figure 34 a and b, respectively). These images show large surface defects while the 15 wt. % membrane displays a greater number of surface pores. The density of particles increased in the 15 wt. % SSOD MMM with relatively even dispersion (Figure 34c). Additional images show the presence of large surface defects on the 15wt. % SSOD/PSF MMM, possible due to the presence of large particle agglomerations. Another explanation lies in the wet phase inversion fabrication process which has often resulted

in defective skin layers and the presence of pores due to stress-induced rupture of the surface layer by the intrusion of the quench medium (Pinnau & Koros, 1991).

Cross-sectional SEM images show an asymmetric membrane consisting of a dense layer of vertically aligned finger-like canals (1-5 μm diameter) and a layer of sponge-like segments of a greater diameter (30-45 μm). These images are similar to membranes produced by wet phase inversion showing a sponge like structure of smaller macro-voids beneath the membrane surface and larger macro-voids in the bulk region. Variation exists around the morphology of polysulfone reported in literature likely due to the use of different solvents and fabrication processes. All asymmetric membranes show a dense region and a larger sponge-like macro void region however, the size and density of these regions is varied which is likely to affect membrane separation performance (Pinnau & Koros, 1991; Madaeni & Moradi, 2011; Tsai et al, 2001; Chen et al, 2009). The torn segments of the PSF show a porous, fibrous web-like morphology. The larger HSOD spherical particles were dispersed within the cavities as well as on the surface layers of the PSF (Figure 35b). Due to the plate-like angular shape of the SSOD particles, these were better integrated into the walls of the PSF (Figure 34c). Greater agglomeration of particles was seen in the SSOD membrane as opposed to the HSOD, likely due to the spherical shape of the HSOD which limits surface contact between particles (Bastani et al, 2013). Due to a large particle size distribution; smaller particles (200-300 nm) were seen to collect on the inner surface layers (Figure 35c) and between the wall fibres while larger particles were spread through the cavities where some agglomeration can be seen (Figure 35b).

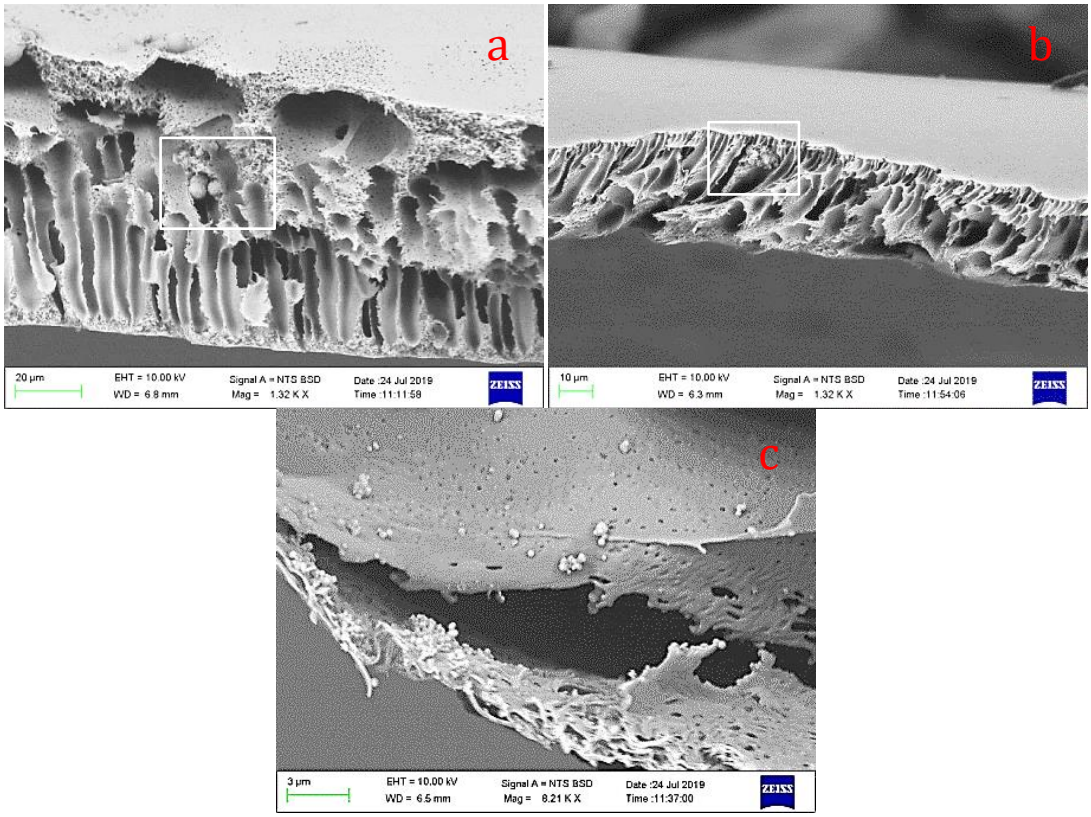


Figure 35: Cross-sectional SEM images of a) 5 wt. % HSOD; b) 5wt % SSOD MMM's (Mag= 800 X) and c) surface layer of 5wt % SSOD MMM's (Mag= 8.21 kX)

Increasing the SSOD loading from 5-15 wt. % (Figure 36) resulted in an increase size of agglomerated particles which is commonly seen in literature (Ahn et al, 2008), resulting in an increase in the formation of larger defects within the dense region leading to more continuous pathways through the membrane, potentially increasing gas permeability but negatively impacting the selectivity of the membrane. An increased volume of particles situated between the fibres of the walls with good dispersion was also observed with increased loading, this suggests good wettability of the particles which is likely due to the presence of silanol groups and the slightly acidic nature of SSOD (Kim et al, 2007).

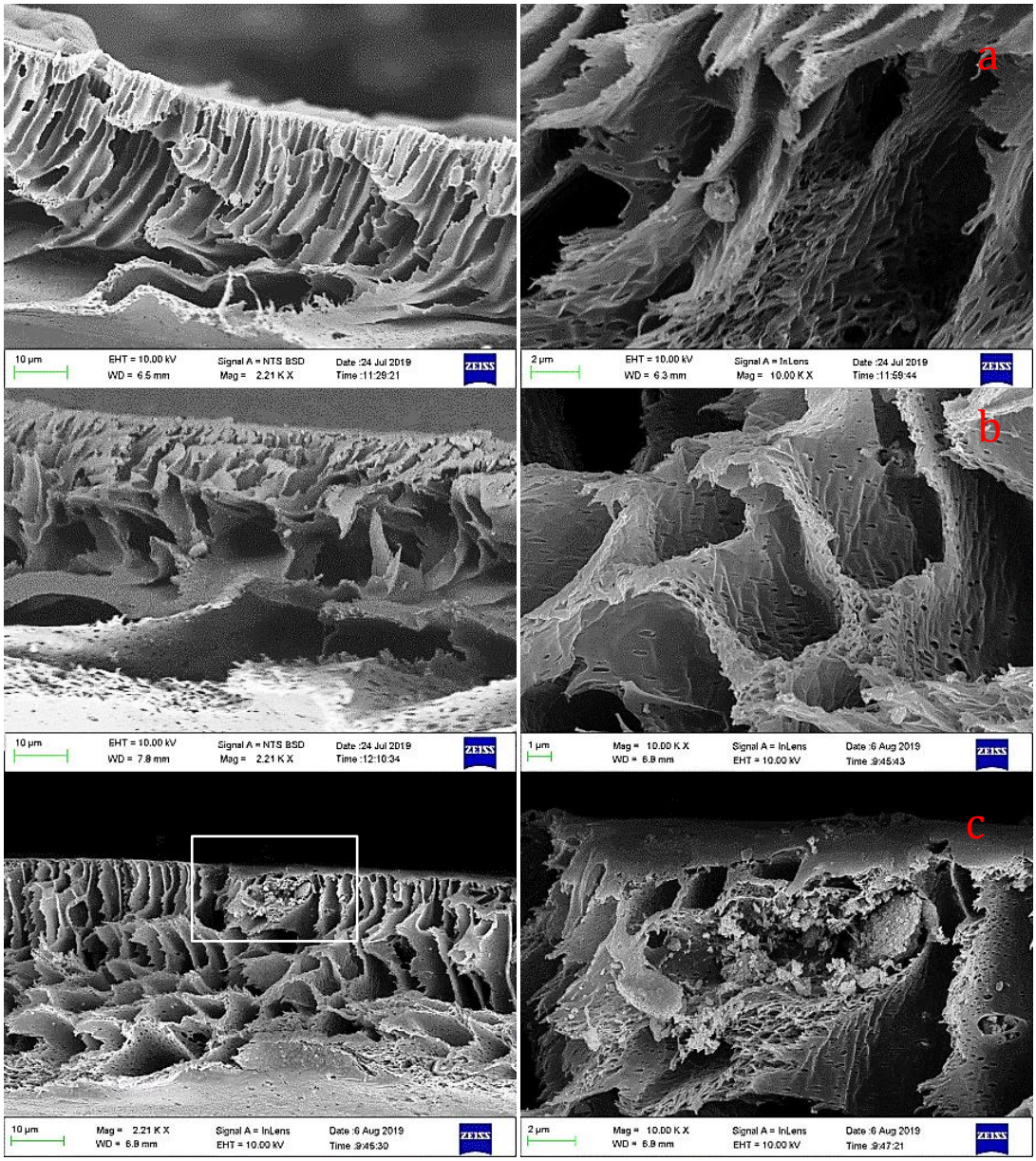


Figure 36: Cross-sectional view of SEM images for SSOD/PSF MMMs at a) 5wt. %; b) 10wt. %; c) 15wt. % at magnifications of 2.21 kX (left) and 10 kX (right), respectively.

5.3.2 Mechanical properties

The membranes tested in this study ranged between 0.039 mm to 0.11 mm with an average thickness of 0.059 mm and variance of 1.9×10^{-5}. This variation is due to the inaccuracy of the doctor blade. In an attempt to improve scientific reliability 4 replicate castings were used for gas permeation and separation experiments and the average permeability and selectivity calculated.

5.3.2.1 Tensile strength

Tensile strength of the mixed matrix membranes was analysed utilizing Young's Modulus (Equation 25). The largest modulus value was found for the pure PSF membrane at 57 MPa, which is considered a mechanically strong material. In comparison, the addition of the filler particles reduced the Young's modulus of the membranes below that of the PSF by 48 % and 53 % for HSOD and SSOD (5wt. %), respectively (Figure 37). Notably the young's modulus calculated in this study for all membranes displayed greater values than that produced for Polysulfone-sodalite MMM's by Daramola et al. (2015) of approximately 0.6 MPa. Young's modulus increased with increased SSOD loading from 5- 15 wt. % (Figure 37) which is consistent with reports of Daramola et al. (2015) and Shen and Lua (2012).

Contradictory to these results the tensile strength of the 5wt. % SSOD/ PSF MMM was greater than that of the HSOD, 10 wt. % and 15wt. % SSOD membranes at 6.8 MPa. These variations required both a greater force and distance before breaking. In this study, the addition of the fillers did not increase the mechanical strength of the membrane as reported in literature (Shen & Lua, 2012; Daramola et al, 2015). One explanation for this is the restriction of the movement of the polymer chains by the formation of hydrogen bonds between the sodalite and PSF (Bastani et al, 2013). Increasing the SSOD loading would increase this interaction, considering the large agglomerate size and poor SSOD dispersion.

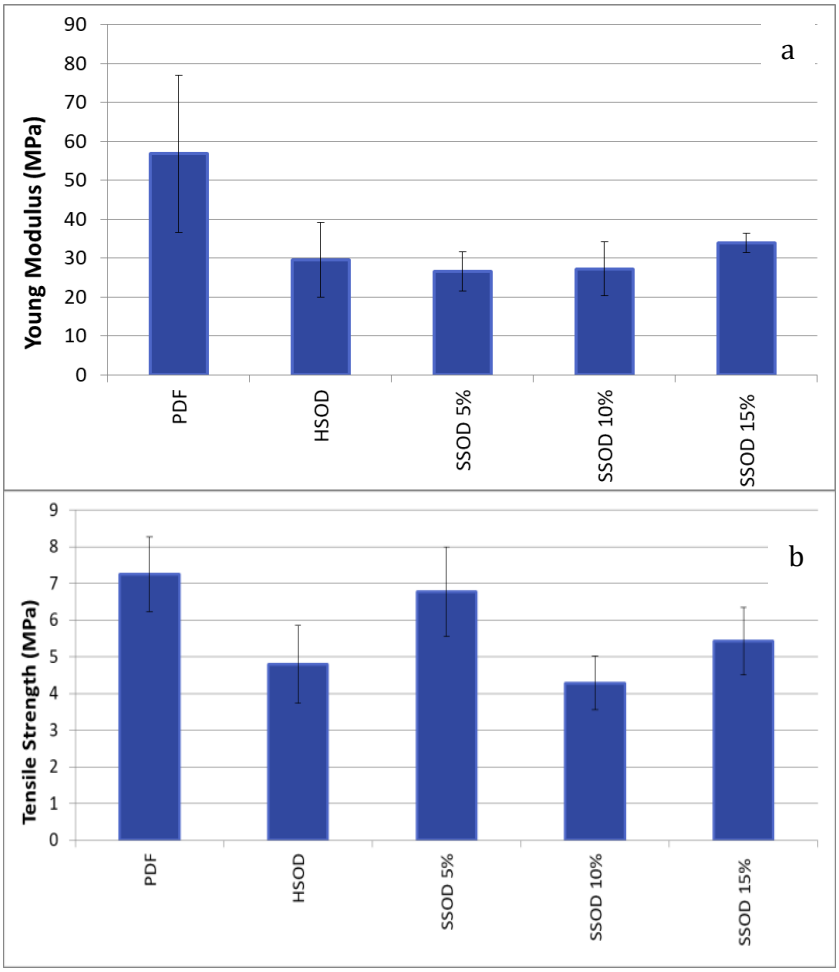


Figure 37: a) Young's Modulus and b) tensile strength for MMMs

5.3.2.2 Thermal stability

In order to investigate the effect of silica sodalite on the thermal and oxidative stability of the Polysulfone membranes, Thermogravimetric analysis (TGA) was performed (Figure 38). Initially there is minimal change in the weight of the samples up to approximately 160 °C; this is attributed to the absence of absorbed moisture due to the hydrophobic nature of the membranes. Three major weight losses can be seen on the TGA curve with peaks at ±520, ±570 and ±620 °C. The PSF, HSOD and SSOD 15wt. % membranes show similar profiles between 150 °C and 490 °C with slight decomposition possibly due to glass transition (190-230 °C). SSOD 5 and 10 wt. % show greater resistance in this region. Polysulfone is known for excellent oxidative and thermal stability due to the sulphur atom in each of the backbone chain diphenylene sulfone groups, which resist the loss of electrons to oxidizing agents (Black & Hastings, 1998). The onset of the first evolution occurs around ±520 °C in all membrane samples showing the same accelerating rate of decomposition up to approximately 540 °C (Figure 38) (Ng et al, 2019). This onset point is in agreement with that shown by Ahn et al.

(2008) who utilized silica filled Polysulfone MMM's. The second decomposition produced deviation between the samples with greater weight loss seen in the HSOD and PSF membranes than that containing SSOD, this could be attributed to a rigidified regions within the polymer due to stress created at the polymer-sodalite interface during the formation of the membranes (Vu et aly, 2003; Moore & Koros, 2005). The addition of the SSOD particles positively impacted the thermal stability of the membranes with 9.42 % of the material remaining as inert at 700 °C.

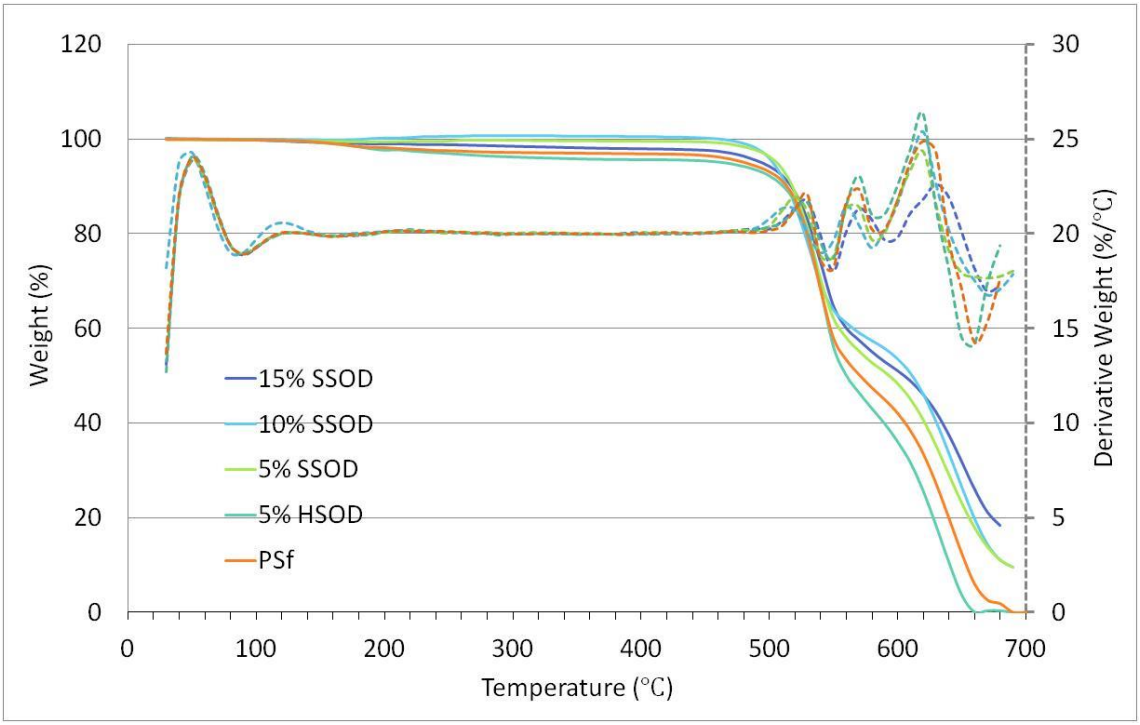


Figure 38: TGA weight (solid) and derivative weight (dashed) graphs for polysulfone mixed matrix membranes

5.3.3 Gas separation performance

Gas separation testing was conducted to evaluate the performance of the sodalite membranes for hydrogen, carbon dioxide separation in line with the second and third objectives. Gas permeations were conducted at ambient temperature and at pressures from 1-5 Bar for hydrogen, nitrogen and carbon dioxide over a permeation period of 5 minutes. Due to the variation in membrane thickness, the membrane permeance in addition to the permeability is presented.

5.3.3.1 Single gas permeations

Effect of higher porosity sodalite on gas separation performance

The results of the single gas permeation tests at 1 Bar for the various membranes are represented in Table 15. The pure PSF membrane (0 wt. %) shows low permeability and a

relatively high selectivity. The addition of the SSOD (5wt. %) increases the H_2 permeability by 582% but reduces the H_2/CO_2 selectivity by 68 %. In comparison, the addition of HSOD (5wt. %) improves the H_2 permeability of the membrane by 960 % with a 79 % reduction in H_2/CO_2 selectivity. Permeability was shown to be positively related to pore size of the zeolite material by Bastani et al. (2013), subsequently the greater pore size of the HSOD (20.3 nm) related to increased permeability than that of the SSOD (12.6 nm) but with lower selectivity. This result can also be partly explained by the presence of pores and defects on the HSOD membrane surface which would reduce the selectivity of the dense region and allow high gas permeation. The increased porosity of the SSOD which was expected to equate to improved permeability over the HSOD may have been invalidated by poor dispersion and agglomeration of particles leading to higher mass transfer resistance. The typical trade-off between permeability and selectivity was seen for the HSOD and SSOD membranes but comparing the permeance of these membranes revealed the SSOD to be slightly greater than that of the HSOD at 7.75×10^{-9} mol/m^2.s.Pa.

Table 16: Single gas permeation results conducted at 1 Bar and 25°C

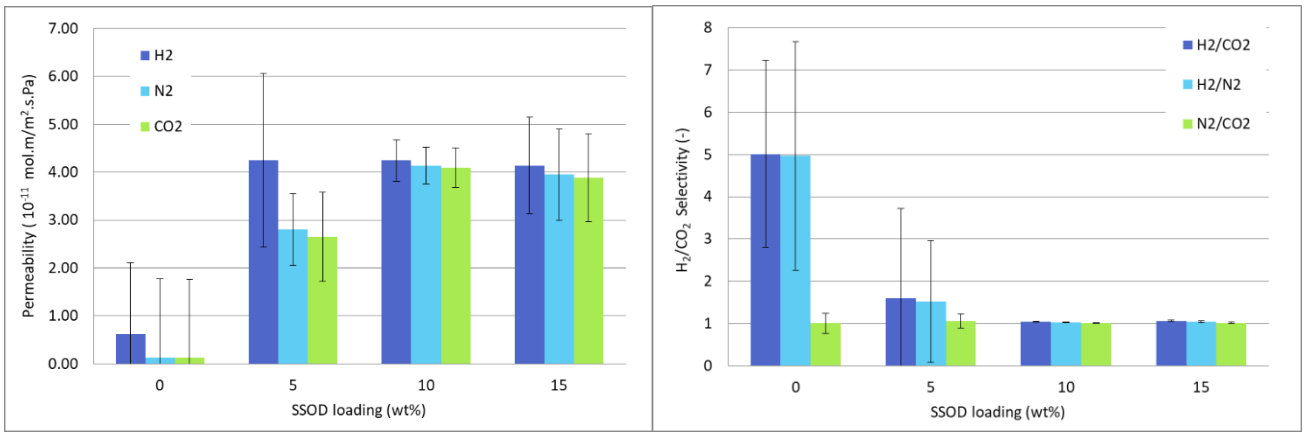
wt %	Filler	Permeability (10^{-11} mol.m/m^2.s.Pa)			Selectivity			Permeance (10^{-9} mol/m^2.s.Pa)		
		H_2	N_2	CO_2	H_2/CO_2	H_2/N_2	N_2/CO_2	H_2	N_2	CO_2
0	-	0.622	0.125	0.124	5.008	4.965	1.009	2.725	1.977	1.974
5	HSOD	6.594	6.277	6.172	1.068	1.051	1.017	7.313	5.842	5.549
5	SSOD	4.244	2.805	2.646	1.604	1.513	1.060	7.751	5.992	5.768
10	SSOD	4.246	4.140	4.090	1.038	1.026	1.012	7.538	7.354	7.261
15	SSOD	4.137	3.952	3.882	1.066	1.047	1.018	7.650	7.315	7.190

Effect of silica sodalite loading on gas separation performance

Increasing the silica sodalite loading increased the H_2, N_2 and CO_2 permeability of the membrane up to a maximum at 10 wt. % after which a slight decline was seen at 15 wt. % SSOD (Figure 39). This parabolic effect could be due to tortuosity around regions of high sodalite agglomeration which was seen at increasing sodalite loading (Kim, et al., 2007). All SSOD loaded membranes show a relative permeability greater than that of the pure PSF membrane (0 wt. %). A decrease in selectivity is noted with increasing SSOD loading up to 10 wt. % for H_2/CO_2 and H_2/N_2 after which the selectivity remains roughly the same. This is likely due to the high volume of surface defects and enhanced free volume of the membrane with increased sodalite loading and agglomerate size (Pinnau & Koros, 1991).

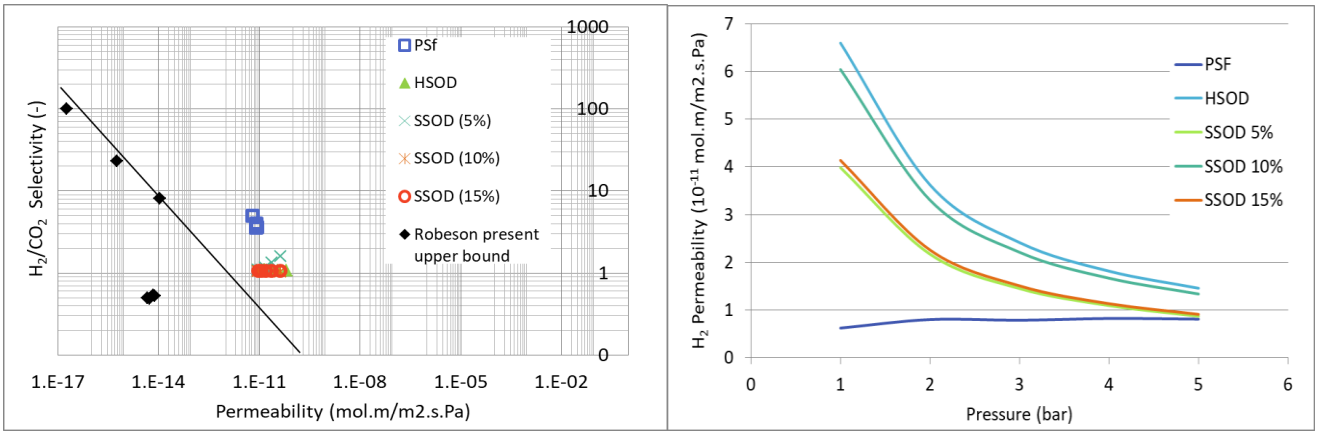
The single gas permeabilties of the membranes reported in this study are significantly less than those reported for H_2/CO_2 separation applications in literature. H_2/CO_2 ideal selectivities are

reported in literature as 0.083 (Jha & Way, 2008), 1.5-2 (Weng et al, 2010), 2.65-3.17 (Huang et al, 2010) and 2.4-4.64 (Karatay et al, 2010) for zeolite/polymer composites. The selectivity reported in this study for the SSOD/PSF MMM's falls on the lower end of this region at 1.6. The membranes produced a flux relatively similar or slightly lower than other zeolite membranes in literature at 10^{-9} to 10^{-7} mol/m^2.s.Pa (Li et al, 2010; Daramola et al, 2015; Huang et al, 2006).



(a) (b)

Figure 39: Effect of silica sodalite loading on membrane a) permeability and b) selectivity (1 Bar)



(a) (b)

Figure 40: a) Robeson's H_2/CO_2 boundary and b) Effect of pressure on H_2 permeability

The ideal selectivity of the MMM's were plotted in relation to the Robeson updated upper boundary and found to be of good performance (Figure 40a), in order to produce membranes that could successfully compete with traditional technologies, modifications to the fabrication process are required to produce defect free membranes of desirable morphology and good filler-polymer interaction (Robeson et al, 1994; Robeson, 2008). Increasing the upstream pressure form 1 to 5 Bar resulted in a decrease in the H_2 (Figure 40b), CO_2 and N_2 permeability

of the filled MMM's while the selectivity remains roughly constant. This behaviour is standard for glassy polymers; as the pressure increases the Langmuir sorption sites in the dense phase become occupied which results in an increased pressure of the permeate and decreased solubility, the impact of membrane plasticization may also account for reduced performance (Li et al, 2013).

5.3.3.2 Mixed gas separation

A 60:40 mixture of H_2:CO_2 was tested at ambient temperature and upstream pressures from 1 to 5 Bar. GC analysis conducted on the feed gas was used to determine a response factor for CO_2 of 47 210 which was used to determine the concentration of CO_2 in the permeate stream.

Effect of higher porosity sodalite on gas separation performance

Considering both the H_2 and CO_2 permeabilties, the HSOD (5 wt. %) membrane was found to be the best performing membrane with high H_2 permeability (374 % >PSF) and low CO_2 permeability producing the highest selectivity of 3.9, followed by the PSF (0 wt. %) membrane with 1.7 (Table 16). The HSOD MMM also exhibited a much higher H_2 permeance and a lower CO_2 permeance than the equivalently loaded SSOD MMM. The addition of the SSOD particles did have the desired effect of greater H_2 permeability but was accompanied by a significant increase in CO_2 permeability (435 % > PSF) and reduced selectivity. This may be attributed to membrane defects with the addition of the silica sodalite particles and the presence of voids around the agglomerates, rendering the size selective nature of the sodalite ineffective as gasses are able to diffuse through the voids around the particles instead of the sodalite pores. The permeance produced for all three of the membranes exceeds that reported by Li et al in ranges at 10^{-8} mol/m^2.s.Pa (Li et al, 2010).

The mixed gas selectivity of the HSOD membrane is greater than the ideal selectivity determined utilizing pure gasses (Table 15) as well as those reported between 1.53-3.57 by Khan et al utilizing a 50 H_2: 50 CO_2 mixture at 12 bar and 25 °C (Khan et al, 2010). The separation factor of 54.9 produced for the 5 wt. % HSOD/PSF is greater than the Knudsen selectivity of 4.7 supporting achievable separation (Bastani et al, 2013).

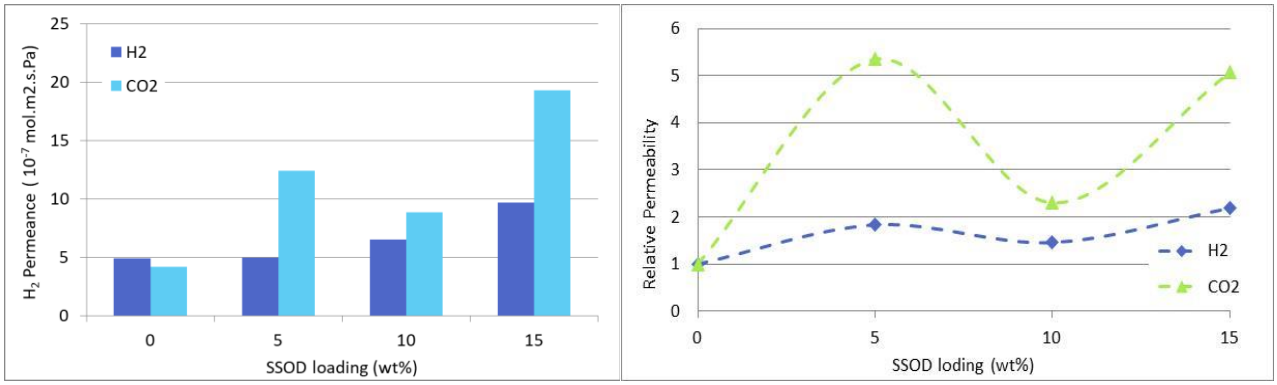
Table 17: Mixed gas permeation (60 H_2: 40 CO_2) results conducted at 1 Bar and 25°C

Wt. %	Filler	Permeability (10^{-11} mol.m/m².s.Pa)		Selectivity	Separation factor (SF)	Permeance (10^{-7} mol/m².s.Pa)	
		H_2	CO_2	H_2/CO_2	H_2/CO_2	H_2	CO_2
0		2.451	2.102	1.749	2.191	4.922	4.22
5	HSOD	11.629	4.476	3.897	54.946	27.170	10.459
5	SSOD	4.493	11.237	0.600	0.573	4.970	12.431
10	SSOD	3.573	4.836	1.108	1.135	6.544	8.857
15	SSOD	5.362	10.653	0.755	0.726	9.714	19.299

Effect of silica sodalite loading on gas separation performance

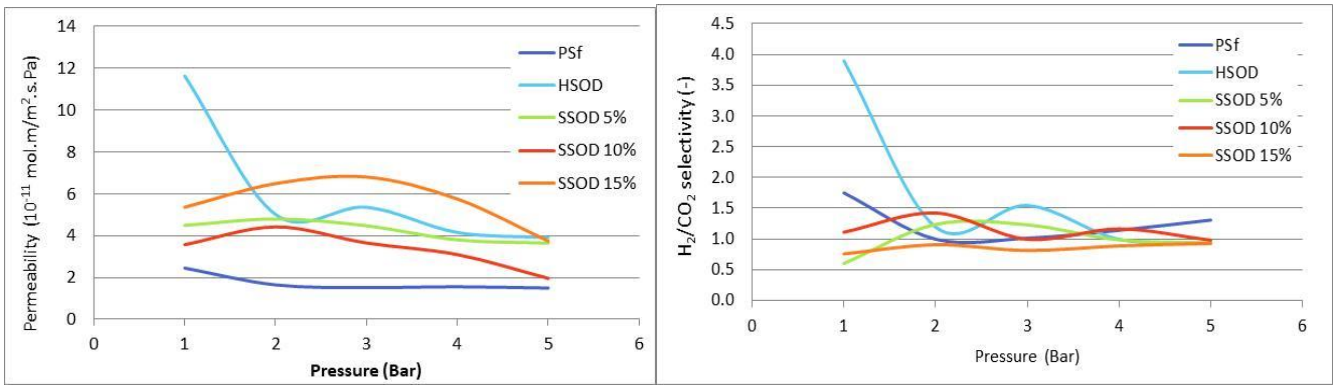
Increasing the SSOD loading resulted in an increase in the membrane H_2 permeance due to the increased porosity, the same trend was seen for the CO_2 permeance with the exception of 10 wt. % SSOD where a notable dip was observed (Figure 41a). This mass transfer resistance may be due to less agglomeration within the membrane as well as less surface pores/defects retaining the integrity of the selective layer. This produced a desirable effect on the selectivity of the membrane producing a value close to that of the pure PSF membrane. The membrane loaded with 10 wt. % SSOD displayed the highest H_2/CO_2 separation factor, however this was still lower than the pure PSF membrane.

A reduction in the H_2 permeability with increasing pressure was seen for PSF and HSOD membranes, Figure 40b as supported by Li et al (2013). Contradictory to this the membranes loaded with SSOD displayed an increased peak followed by a decline in permeability around 2-3 Bar. With the exception of the HSOD, the selectivity of the membranes remains relatively constant from1 to 5 Bar. This could again be attributed to polymer-filler compatibility (Khan et al, 2010).



(a) (b)

Figure 41: Effect of SSOD loading on a) permeance and b) relative permeability



(a) (b)

Figure 42: Effect of pressure on MMM a) permeability and b) selectivity

5.4 Concluding remarks

The Polysulfone membranes in this study displayed an asymmetric morphology consisting of a smaller layer of vertical canals and a larger sponge-like layer. SEM imaging of the 2D surface showed the dispersion of HSOD and SSOD particles throughout the membrane. Surface defects and smaller pores were visible in some membrane images. Large agglomerates of SSOD were seen with increasing size at higher filler loading. The tensile strength of the membrane decreased with the addition of HSOD and SSOD loadings above 5wt. %. All PSF mixed matrix membranes showed good thermal and oxidative stability up to 500 °C.

The optimized silica sodalite particles, displaying higher surface area and porosity than the hydrothermally synthesized hydroxy sodalite, display a greater flux of 7.75 $\times 10^{-9}$ mol/m^2.s.Pa and higher ideal selectivity than the HSOD membrane in pure gas separations. The common tradeoff between permeability and selectivity was seen with increased SSOD loading. The permeance decreased with increasing pressure while selectivity remained relatively constant.

The 5wt. % SSOD membrane performed poorly in the mixed gas separation tests with a real selectivity much lower than the HSOD and pure PSF membranes, due to an exceptionally high

CO_2 permeability. The HSOD displayed good separation at 1 Bar with a high separation factor of 54. A 10wt. % SSOD/PSF MMM was concluded to be the best of the SSOD loaded membranes with the highest selectivity at 1.1, and a H_2 permeability of 4.25 $\times 10^{-11}$ mol.m/m^2.s.Pa. Increasing the pressure resulted in a peak in the SSOD (5, 10, 15 wt. %) permeability around 2-3 Bar. The use of silica sodalite in mixed matrix membranes still holds potential for high separation performance. Changing the fabrication procedure to allow more controlled solvent evaporation and the formation of an ultra-thin skin layer may improve the membranes performance by reducing the number of surface defects and reducing the void size (Pinnau & Koros, 1991). Surface modification and post-fabrication treatments may potentially improve membrane selectivity and particle-polymer interaction.

Chapter 6: Conclusions and Recommendations

6.1 Conclusions

The capture and storage of anthropogenic CO_2 has become a topic of major focus over the past decade. The hyperinflation of energy costs, the depletion of fossil fuels and severe climate change are all factors encouraging the move to highly energy efficient of industrial processes. One application is the capture of CO_2 from H_2 in pre-combustion power generation, a process of increasing importance with the exponentially increasing energy demand. Membrane, and specifically mixed matrix membrane separation serve as viable alternatives to traditional processes if highly selective, thermally stable, easily fabricated membranes can be produced. Mixed matrix membranes combine the advantages of polymer membranes with those of inorganic fillers such as hydroxy sodalite to form membranes with the potential of high permeability and selectivity. Hydroxy sodalite is a common zeolite with a cage structure of small pore aperture capable of separating small molecules such as H_2 and He from larger ones. However, this material is plagued by the inclusion of water within the cage structures that limit the permeability of gasses, attempting to remove this through dehydration results in the collapse of the cage structures above 400 °C rendering the material useless for gas separation applications.

This study successfully synthesized silica sodalite crystals without occluded water molecules through topotactic conversion. Inconsistencies in the method utilized by previous researchers to produce high quality SSOD lead the investigation into a number of synthesis parameters; acid strength, acid treatment time, calcination time and temperature, in order to determine the synthesis values to produce high quality SSOD. These synthesized SSOD crystals were characterized and compared to the hydrothermally synthesized HSOD.

The BET surface area and pore volume of the particles was used to quantify SSOD quality and used as the responses to determine regression models considering the synthesis parameters. Acid treatment time was found to be an insignificant model factor in both the surface area and pore volume models and removed from further investigation. Calcination temperature was a significant model parameter in both the preliminary and extended models. Higher acid strength, lower calcination time (<3 h) and lower calcination temperature were found to improve SSOD quality. SSOD showed a greatly improved surface are and pore volume over HSOD with 56.56 m^2/g and 0.1810 cm^3/g, respectively. Synthesis variables of 5 M propionic acid, 1h calcination at 873 K were predicted to maximize both the surface area and pore volume of SSOD while minimizing the calcination time and temperature.

The synthesized SSOD was then utilized as a filler in polysulfone mixed matrix membranes to determine the H_2/CO_2 separation performance of the membranes utilizing the higher porosity sodalite. The effect of increasing the SSOD loading on the separation performance was also investigated. The study was constrained by ineffective equipment resulting in an unequal membrane thickness to combat this, the average of multiple castings was considered as well as membrane permeance. The hydrogen permeance of the membrane was successfully increased through the addition of the SSOD filler however, reduced ideal selectivity was reported. In relation to the traditionally synthesized HSOD, SSOD showed greater membrane performance with pure hydrogen and carbon dioxide. Utilizing a 60:40 H_2:CO_2 gas mixture; the HSOD showed greater performance over SSOD, with higher separation factor of 54.9 and H_2 permeance of 27.210^{-7} mol/m^2.s.Pa. This may be attributed to the spherical shape of the HSOD particles thereby limiting particle agglomeration as opposed to the plate like SSOD crystals which form larger agglomerates causing voids and surface defects. The SSOD/PSF MMM displayed improved performance relative to that previously reported in literature. Increasing SSOD loading was observed to improve membrane performance up to a peak at 10 wt.% SSOD.

The membrane performance was affected by surface defects and particle agglomeration but showed good potential for H_2/CO_2 relative to other zeolite mixed matrix membranes in literature. Utilizing a different fabrication procedure, a reliable casting method or surface modifications could produce defect free membranes with greater selectivity.

6.2 Recommendations

The experiment was restricted by the poor yield of sodalite produced from RUB-15, despite extensive centrifugal separation, and the large volume of propionic acid required following the treatment ratio stipulated in literature. Larger SSOD crystal size may improve separation and product yield followed by particle size reduction to produce the desired nanoparticles.

The crystallinity of the synthesized RUB-15 was found to vary greatly between replicates thereby, influencing the crystallinity of the resulting SSOD. Further research into the one pot synthesis of high crystallinity RUB-15 with short fabrication time and lower temperature should be conducted and perfected to produce a reliable synthesis protocol. While other SSOD synthesis parameters such as the effect of acid treatment ratio could be considered for investigation with the aim of improving SSOD yield. Due to this limitation only the highest SA SSOD samples from the preliminary investigation were tested in XRD analysis. Further testing of all of the samples may provide greater insight into understanding the effect synthesis variables play on sodalite crystallinity.

Other membrane fabrication methods to produce defect free membranes such as dry/ wet phase inversion could allow for defect free membranes, smaller pores and less agglomeration by controlling the macro-void distribution and reducing polymer phase separation (Chen et al, 2009; Pinnau & Koros, 1991). Functionalization to allow for better particle/polymer interaction and improved wettability or the use of coatings may also benefit separation performance. The effect of increased temperature on membrane performance has not been investigated here but serves as a critical consideration for industrial applications such as in pre-combustion CO_2 separation.

Constraints were placed on casting through the use of sub-standard equipment resulting in inconsistent membrane thickness. Consistent membrane thickness produced by a precise blade would allow for more accurate permeability calculations instead of membrane permeance as presented in this study. Defects were produced in the membranes due to air bubbles in the casting mixture despite repeated sonication and resting, a softer stirring mechanism or longer sonication and resting time may reduce membrane defects.

This study was limited to the separation of CO_2 from H_2 in a 60:40 CO_2:H_2 mixture, further studies into the effect of CO_2 concentration on membrane performance and the effect of impurities such as CO and SO_2 should also be further researched. Separation experiments were limited to ambient temperature and low pressure, in order to assess industrial feasibility the membranes should be tested under temperatures between 400-600°C and increased pressures.

Large deviation was seen between the response factors produced from GC analysis of the 60:40 H_2:CO_2 mixed gas, showing a standard error of $\pm$346.4. Due to constraints on funding and the concentration of the mixed gas, the development of a calibration curve was unachievable. A calibration curve utilizing the pure gasses and various mixtures of the two would increase the reliability of the gas separation data obtained.

The use of the improved porosity silica sodalite as an adsorption catalyst may also be investigated due to its micro-porous structure and small cage aperture enabling the capture of small molecules such as ammonia. Additionally, the hydrophobic nature of the material makes silica sodalite insensitive to moisture.

References

Ahn, J., Chung, W.-J., Pinnau, I. & Guiver, M. D., 2008. Polysulfone/silica nanoparticle mixed-matrix membranes for gas separation. *Journal of membrane science,* Volume 314, pp. 123-133.

Anthony, E. J., 2010. 11 - Chemical-looping combustion systems and technology for carbon dioxide (CO2) capture in power plants. In: *Developments and Innovation in Carbon Dioxide (CO_2) Capture and Storage Technology.* s.l.:Science Direct- Carbon Dioxide (CO_2) Capture, Transport and Industrial Applications, pp. 358-379.

Anwar, N. M. et al., 2018. CO2 capture and storage: A way forward for sustainable environment. *Journal of Environmental Management,* Volume 226, pp. 131-144.

Asakura, Y., Takayama, R., Shibue, T. & Kuroda, K., 2014. Topotactic Conversion of b-Helix-Layered Silicate into AST-Type Zeolite through Successive Interlayer Modifications. *Chemistry European Journal,* Volume 20, pp. 1893-1900.

Baker, R., 1991. *Membrane separation systems : recent developments and future directions.* New Jearsey: Park Ridge.

Bastani, D., Esmaeili, N. & Asadollahi, M., 2013. Polymeric mixed matrix membranes containing zeolites as a filler for gas separation applications: A review. *Journal of Industrial and Engineering Chemistry,* Volume 19, pp. 375-393.

Basu, A., Akhtar, J., Rahman, M. & Islam, M., 2004. A review of separation of gasses using membrane systems. *Petroleum Science and Technology,* Volume 22, p. 1343.

Belviso, C., Lettino, A. & Cavalcante, F., 2018. Influence of Synthesis Method on LTA Time-Dependent Stability. *Molecules,* 23(9), pp. 2122-.

Berry, M. B. et al., 2000. Incorporation of zeolites into composite matrices. *Microporous and Mesoporous Materials,* 39(1), pp. 205-217.

Bhattacharya, A. & Misra, B., 2004. Grafting: a versatile means to modify polymers: Techniques, factors and applications. *Progress in Polymer Science,* 29(8), pp. 767-814.

Black, J. & Hastings, G., 1998. *Handbook of Biomaterial Properties.* Dordrecht: Springer science and Business Media.

Bos, A., Punt, I., Strathmann, H. & Wessling, M., 2001. Suppression of gas separation membrane plasticization by homogeneous polymer blending. *AIChE Journal,* 47(5), pp. 1088-1093.

Breck, D. W., 1974. *Zeolite Molecular Sieves Structure, Chemistry and Use.* New York: Wiley & Sons Inc..

Castruita de León, G. et al., 2018. Effect of silica source on the synthesis and properties of polysulfone/silica composite membranes for gas separation. *Revista Mexicana de Ingeniería Química,* 17(2), pp. 693-705.

Chakraborty, S., Wang, B. & Dutta, P., 2016. Tolerance of polymer-zeolite composite membranes to mechanical strain. *Journal of membrane science,* Volume 518, pp. 192-202.

Chen, S. et al., 2009. Preparation and characterizations of asymmetric sulfonated polysulfone membranes by wet phase inversion method. *European Polymer Journal,* Volume 45, pp. 1293-1301.

Chitsiga, T. L., Daramola, M. O., Wagner, N. & Ngoy, J. M., 2018. Parametric effect of adsorption variables on CO2 adsorption of amine-grafted polyaspartamide composite adsorbent during post-combustion CO2 capture: a response surface methodology approach. *International Journal of Oil, Gas and Coal technology,* 17(3), pp. 321-336.

Chunga, T., Jianga, L., Lia, Y. & Kulprathipanja, S., 2007. Mixed matrix membranes (MMMs) comprising organic polymers with dispersed inorganic fillers for gas separation. *Progess in polymer science,* Volume 32, pp. 483-507.

Coates, J., 2006. Interpretation of Infrared Spectra, A Practical Approach. *Encyclopedia of Analytical Chemistry,* pp. 1-23.

Daramola, M., Dinat, A. & Hasrod, S., 2015. Synthesis and Characterization of Nanocomposite Hydroxy-Sodalite/Ceramic Membrane via Pore-Plugging Hydrothermal Synthesis Technique. *Journal of Membrane and Separation Technology,* Volume 4, pp. 1-7.

Daramola, M., Oloye, O. & Yaya, A., 2017. Nanocomposite sodalite/ceramic membrane for pre-combustion CO2 capture: synthesis and morphological characterization. *International journal of coal science & technology,* 4(1), pp. 60-66.

Daramola, M., Silinda, B., Masondo, S. & Oluwasina, O., 2015. Polyethersulphone-sodalite (PES-SOD)Polyethersulphone-sodalite (PES-SOD) mixed-matrix membranes: prospects for acid mine drainage (AMD) treatment. *The South African Institute of Minning and Metallurgy,* Volume 115, pp. 1221-1228.

Díaz, K., López-González, M., Castillo, L. d. & Riande, E., 2011. Effect of zeolitic imidazolate frameworks on the gas transport performance of ZIF8-poly(1,4-phenylene ether-ether-sulfone) hybrid membranes. *Journal of membrane science,* 383(1-2), pp. 206-213.

Dong, F. et al., 2019. The process of peak CO2 emissions in developed economies: A perspective of industrialization and urbanization. *Resources, Conservation & Recycling,* Volume 141, pp. 61-75.

Duval, J. et al., 1994. Preparation of Zeolite Filled Glassy Polymer Membranes. *Journal of applied polymer science,* 54(4), pp. 409-418.

Earth Life Africa Johannesburg, 2009. *Climate change, developement and energy problems in SOuth Africa: Another world is possible,* Johannesburg: OxFam International.

Etxeberria-Benavides, M. et al., 2017. High performance mixed matrix membranes (MMMs) composed of ZIF-94 filler and 6FDA-DAM polymer. *Journal of membrane science.*

Evans, M., 2019. *7 Ways to reduce CO2 emissions pollution in industry.* [Online] Available at: www.thebalancesmb.com/reducing-co2-emissions-3157794 [Accessed November 2019].

Ferreira, S. et al., 2007. Box-Behnken design: An alternative for the optimization of analytical methods. *Analytica Chimica Acta,* Volume 597, pp. 179-186.

Fischer, R. A., 1935. *The design of experiments.* 1st ed. New York: Hafner publishing company.

Fischer, R. X. & Baur, W. H., 2009. Symmetry relationships of sodalite (SOD) – type crystal structures. *Zeitschrift für Kristallographie - Crystalline Materials,* 224(4), pp. 185-197.

Gazzani, M., Macchi, E. & Manzolini, G., 2013. CO2 capture in natural gas combined cycle with SEWGS. Part A: thermodynamic performances. *International Journal of Greenhouse Gas Control,* Volume 12, pp. 493-501.

Gouedard, C., Picq, D., Launay, F. & Carrette, P. L., 2012. Amine degradation in CO2 capture I. A review. *International journal of greenhouse gas control,* Volume 10, pp. 244-270.

Groen, J. C., Peffer, L. A. A. & Perez-Ramirez, J., 2003. Pore size determination in modified micro- and mesoporous materials. Pitfalls and limitations in gas adsorption data analysis. *Microporous and Mesoporous Materials,* Volume 60, pp. 1-17.

Grubler, A. & Fujii, Y., 1991. Inter-generational and spatial equity issues of carbon accounts. *Energy,* 16(11-12), pp. 1397-1416.

Hashemifard, S., Ismail, A. & Matsuura, T., 2011. Mixed matrix membrane incorporated with large pore size halloysite nanotubes (HNT) as filler for gas separation: Experimental. *Journal of Colloid and Interface Science,* Volume 359, pp. 359-370.

Hashemifard, S., Ismail, A. & Matsuura, T., 2011. Mixed matrix membrane incorporated with large pore size halloysite nanotubes (HNTs) as filler for gas separation: Morphological diagram. *Chemical Engineering Journal,* Volume 172, pp. 581-590.

Hess, S. & Staudt, C., 2007. Variation of esterfication conditions to optimize solid-state crosslinking reaction of DABA-containing copolyimide membranes for gas separations. *Desalination,* 217(1-3), pp. 8-16.

Hinchliffe, A. & Porter, K., 2000. A comparison of membrane separation and distillation. *Institution of chemical engineers,* Volume 78, pp. 255-268.

Huang, A., Bux, H., Steinbach, F. & Caro, J., 2010. Molecular-Sieve Membrane with Hydrogen Permselectivity: ZIF-22 in LTA Topology Prepared with 3-Aminopropyltriethoxysilane as Covalent Linker. *Angewandte Chemie,* 122(29), pp. 2075-5081.

Huang, A., Dou, W. & Caro, J., 2010. Steam-Stable Zeolitic Imidazolate Framework ZIF-90 Membrane with Hydrogen Selectivity through Covalent Functionalization. *Journal of the american chemical society,* 132(44), pp. 15562-15564.

Huang, Y., Baker, R. W. & Vane, L. M., 2010. Low-Energy Distillation-Membrane Separation Process. *Industrial & Engineering Chemistry Research,* Volume 49, pp. 3760-3768.

Huang, Z. et al., 2006. Enhanced Gas Separation Properties by Using Nanostructured PES-Zeolite 4A Mixed Matrix Membranes. *Journal of applied polymer science,* Volume 101, pp. 3800-3805.

IEA, 2019. *Global Energy & CO2 Status Report 2018,* Paris: IEA.

International Energy Agency, 2015. *World energy outlook.* Paris: International Energy Agency.

International Zeolite Association, 2007. *Database of Zeolite Structures.* [Online] Available at: http://europe.iza-structure.org/IZA-SC/framework.php?STC=SOD

IPCC, 2018. *Global Warming of 1.5°C. An IPCC Special Report on the impacts of global warming of 1.5°C above pre-industrial levels and related global greenhouse gas emission pathways, in the context of strengthening the global response to the threat of climate change,,* Geneva: World Meteorological Organization.

Iravaniniaa, M., Mirfendereski, M. & Mohammadi, T., 2011. Pervaporation separation of toluene/n-heptane mixtures using a MSE-modified membrane: Effects of operating conditions. *Chemical Engineering Research and Design,* 90(3), pp. 397-408.

Ismail, A., Khulbe, K. & Matsuura, T., 2015. *Gas separation membranes: Polymeric and inorganic.* s.l.:springer.

Jansen, D., Gazzani, M., Manzolini, G. & Van Dijk, E., 2015. Pre-combustion CO2 capture. *International Journal of Greenhouse Gas Control,* Volume 40, pp. 167-187.

Jha, P. & Way, J. D., 2008. Carbon dioxide selective mixed-matrix membranes formulation and characterization using rubbery substituted polyphosphazene. *Journal of Membrane Science,* 324(1-2), pp. 151-161.

Junaidi, M. et al., 2013. Fluorocarbon functionalized SAPO-34 zeolite incorporated in asymmetric mixed matrix membranes for carbon dioxide separation in wet gases. *Fuel process technology,* 112(22), pp. 1-6.

Kapantaidakis, G. C., Kaldis, S. P., Dabou, X. S. & Sakellaropoulos, G. P., 1996. Gas permeation through PSF-PI miscible blend membranes. *Journal of membrane science,* 110(2), pp. 239-247.

Karatay, E., Kalıpçılar, H. & Yılmaz, L., 2010. Preparation and performance assessment of binary and ternary PES-SAPO 34-HMA based gas separation membranes. *Journal of membrane science,* 364(1-2), pp. 75-81.

Karger, J. & Ruthven, D., 1992. *Diffusion in Zeolites and Other Microporous Materials.* New York: Wiley.

Karniadakis, G., Beskok, A. & Aluru, N., 2005. *Microflows and Nanoflows- Fundamentals and Simulation.* New York: Springer.

Khajavi, S., Jansen, J. & Kapteijn, F., 2010. Production of ultra pure water by desalination of seawater using a hydroxy sodalite membranes. *Journal of membrane science,* Volume 356, pp. 52-57.

Khajavi, S., Kapteijn, F. & Jansen, J. C., 2007. Synthesis of thin defect-free hydroxy sodalite membranes: New candidate for activated water permeation. *Journal of Membrane Science,* Volume 299, pp. 63-72.

Khajavi, S. et al., 2010. Thermostability of hydroxy sodalite in view of membrane applications. *Microporous and mesoporous materials,* Volume 132, p. 510.

Khan, A. J. et al., 2010. Hydrogen separation and purification using polysulfone acrylate–zeolite mixed matrix membranes. *Journal of Membrane Science,* Volume 350, pp. 340-346.

Kim, S. et al., 2007. *High permeability/ high diffusivity mixed matrix membranes for gas separation.* Blacksburg, Virginia: Virginia Polytechnic Insitute and State University.

Koike, M. et al., 2017. Topotactic conversion of layered silicate RUB-15 to silica sodalite through interlayer condensation in N-methylformamide. *Dalton Transactions,* Volume 46, pp. 10232-10239.

Kooli, F., Liu, Y., Hbaieb, K. & Al-Faze, R., 2016. A novel synthetic route to obtain RUB-15 phase by pseudo solid-state conversion. *Microporous and Mesoporous Materials,* Volume 228, pp. 116-122.

Kosinov, N., Gascon, J., Kapteijn, F. & Hensen, E., 2016. Recentdevelopmentsinzeolitemembranesforgasseparation. *Journal of membrane science,* Volume 499, pp. 65-79.

Lane, K., 2018. *IEA Energy Efficiency 2018 and World Energy Outlook 2018.* Brussels: International Energy Agency.

Leung, D., Caramanna, G. & Mercedes Maroto-Valer, M., 2014. An overview of current status of carbon dioxide capture and storage technologies. *Renewable and Sustainable Energy Reviews,* Volume 39, pp. 426-443.

Lin, B. & Li, X., 2011. The effect of carbon tax on per capita CO2 emissions. *Energy Policy,* 39(9), pp. 5137-5146.

Lindsey, R., 2019. *Climate Change: Atmospheric Carbon Dioxide.* [Online] Available at: https://www.climate.gov/news-features/understanding-climate/climate-change-atmospheric-carbon-dioxide
[Accessed 22 October 2019].

Li, P., Chung, T. S. & Paul, D. R., 2013. Gas sorption and permeation in PIM-1. *Journal of Membrane Science,* Volume 432, pp. 50-57.

Liu, Y., Hu, E., Khan, E. & Lai, Z., 2010. Synthesis and characterization of ZIF-69 membranes and separation for CO2/CO mixture. *Journal of membrane science,* 353(1), pp. 36-40.

Li, Y. et al., 2010. Zelitic imidazolate framework ZIF-7 based molecular sieve membrane for hydrogen separation.. *Journal of membrane science,* Volume 354, pp. 48-54.

Madaeni, S. & Moradi, P., 2011. Preparation and characterization of asymmetric polysulfone membrane for separation of oxygen and nitrogen gases. *Journal of applied polymer science,* 121(4), pp. 2157-2167.

Mahajan, R., Burns, R., Schaeffer, M. & Koros, W., 2002. Challenges in forming successful mixed matrix membranes with rigid polymeric materials. *Journal of applied polymer science,* 86(8), pp. 81-90.

Mahajan, R. & Koros, W., 2002. Mixed matrix membrane materials with glassy polymers, Part 1. *Polymer engineering and science,* Volume 42, pp. 1420-1432.

Marler, B. & Gies, H., 2012. Hydrous layer silicates as precursors for zeolites obtained through topotactic condensation: a review. *European journal of mineralogy,* Volume 24, pp. 405-428.

Marler, B., Stroter, N. & Gies, H., 2005. The structure of the new pure silica zeolite RUB-24, Si32O64, obtained by topotactic condensation of the intercalated layer silicate RUB-18. *Microporous and Mesoporous Materials,* Volume 83, pp. 201-211.

Matteucci, S., Yampolskii, Y., Freeman, B. D. & Pinnau, I., 2006. Transport of gases and vapors in glassy and rubbery polymers. In: *Materials Science of Membranes for Gas and Vapor Separation.* s.l.:Wiley and Sons, pp. 1-47.

McNaught, A. D. & Wilkinson, A., 1997. *IUPAC. Compendium of Chemical Terminology.* 2nd (the 'Gold Book') ed. Oxford: Blackwell Scientific Publications.

Melgar, V., Kim, J. & Othman, M., 2015. Zeolitic imidazolate framework membranes for gas separation: A review of synthesis methods and gas separation performance. *Journal of Industrial and Engineering Chemistry,* Volume 28, pp. 1-15.

Momma, K. & Izumi, F., 2011. VESTA 3 for three-dimensional visualization of crystal, volumetric and morphology data. *Journal of applied crystallography,* Volume 44, pp. 1272-1276.

Montgomery, D. C., 2013. *Design and analysis of experiments.* 8th ed. Arizona: Wiley and Sons, Inc..

Moore, T. & Koros, W., 2005. Non-ideal effects in organic–inorganic materials for gas separation membranes. *Journal,* 739(1-3), pp. 87-98.

Moparthi, A., Uppaluri, R. & Gill, B., 2010. Economic feasibility of silica and palladium composite membranes for industrial dehydrogenation reactions. *Chemical Engineering Research and Design,* Volume 88, pp. 1088-1101.

Moradihamedani, P., Ibrahim, N. A., Yunus, W. M. Z. W. & Yusof, N. A., 2015. Study of Morphology and Gas Separation Properties of Polysulfone/Titanium Dioxide Mixed Matrix Membranes. *Polymer engineering science,* Volume 55, pp. 367-374.

Moteki, T. et al., 2011. Role of Acidic Pretreatment of Layered Silicate RUB-15 in its Topotactic Conversion into Pure Silica Sodalite. *Chemistry of materials,* Volume 23, pp. 3564-3570.

Moteki, T., Chaikitisilp, W., Shimojima, A. & Okuba, T., 2008. Silica sodalite without occluded organic maatter by topotactic conversion of lamellar precursor. *American Chemical Society,* Volume 130, pp. 15780-15781.

Mrabet, Z., Alsamara, M., Salman Saleh, A. & Anwar, S., 2019. Urbanization and non-renewable energy demand: A comparison of developed and emerging countries. *Energy,* Volume 170, pp. 832-839.

Münzer, S., Caro, J. & Behrens, P., 2008. Preparation and characterization of sodium-free nanocrystalline sodalite. *Microporous and Mesoporous Materials,* Volume 110, pp. 3-10.

Nagelkerken, I. & Connell, S. D., 2015. Global alteration of ocean ecosystem functioning due to increasing human CO2 emissions. *Proceedings of the Nation Academy of Sciences of the United States of America,* 112(43), pp. 13272-13277.

Ng, H. M., Saidi, N. M., Kasi, R. & Subramaniam, R. T., 2019. Thermogravimetric Analysis of Polymers. *Encyclopedia of Polymer Science and Technology.*

NIST/SEMATECH, 2010. *Engineering statistics handbook.* s.l.:National institute of standards and technology.

Nunes, S. P. & Peinemann, K., 2001. *Membrane Technology in the Chemical Industry.* Weinheim: Wiley.

Oberhagemann, U. et al., 1996. A Layer Silicate: Synthesis and Structure of the Zeolite Precursor RUB-15—$[N(CH_3)_4]_8[Si_{24}O_{52}(OH)_4]\cdot_{20}\ H_2O$. *Angewandte chemie international edition,* 35(23-24), pp. 2869-2872.

Oloye, O. & Daramola, M. O., 2017. *Synthesis and performance evaluation of nanocomposite ceramic-sodalite membranes for pre-combustion co2 capture.* Johannesburg: University of the Witwatersrand.

ONE Energy, 2017. *The current electricity crisis in South Africa.* [Online] Available at: http://www.oneenergy.co.za/Energy-crisis-south-africa.asp

Onoji, S. E., Iyuke, S. E., Igbafe, A. I. & Daramola, M. O., 2017. Transesterification of Rubber Seed Oil to Biodiesel over a Calcined Waste Rubber Seed Shell Catalyst: Modeling and Optimization of Process Variables. *Energy and Fuels,* Volume 31, pp. 6109-6119.

Pachauri, R., Meyer, L. & Core Writing Team, 2014. *Climate Change 2014: Synthesis report. Contribution of Working Groups I, II and III to the Fifth Assessment Report of the,* Geneva, Switzerland: IPCC.

Peivasti, M., Madandar, A. & Mohammadi, T., 2008. Effect of operating conditions on pervaporation of methanol/methyltert-butyl ether mixtures. *Chemical Engineering and Processing: Process Intensification,* Volume 47, pp. 1069-1074.

Pinnau, I. & Koros, W. J., 1991. Structures and Gas Separation Properties of Asymmetric Polysulfone Membranes Made by Dry, Wet and Dry/ Wet Phase Inversion. *Journal of Applied Polymer Science,* Volume 43, pp. 1491-1502.

Pires, J. C. M., Martins, F. G., Alvim-Ferraz, M. C. M. & Simões, M., 2011. Recent developments on carbon capture and storage: An overview. *Chemical Engineering Research and Design,* Volume 89, pp. 1446-1460.

Porter, M., 1990. *Handbook of industrial membrane technology.* New Jersey: Noyes Publications.

Prabhu, A. & Oyama, S., 2000. Highly hydrogen selective ceramic membranes: application to the transformation of greenhouse gases. *Journal of membrane science,* 176(2), pp. 233-248.

Rafiq, S. et al., 2012. Separation of CO2 from CH4 using polysulfone/polyimide silica nanocomposite membranes. *Separation and Purification Technology,* Volume 90, pp. 162-172.

Rampedi, R., Dhlamini, S. & Daramola, M., 2016. *Topotactic conversion of RUB-15 to Silica Sodalite Crystals,* Johannesburg: School of Chemical and Metallurgical Engineering, University of the Witwatersrand (Unpublished).

Reible, D. D. & Shair, F. H., 1982. A technique for the measurement of gaseous diffusion in porous media. *Journal of soil science,* Volume 33, pp. 165-174.

Rezakazemi, M. et al., 2014. State-of-the-art membrane based CO2 separation using mixed matrix membranes (MMMs): An overview on current status and future directions. *Progress in polymer science,* Volume 39, pp. 817-861.

Robeson, L. M., 1991. Correlation of separation factor versus permeability for polymetric membranes. *Journal of membrane science,* Volume 62, p. 165.

Robeson, L. M., 2008. The upper bound revisited. *Journal of membrane science,* Volume 320, pp. 390-400.

Robeson, L. M. et al., 1994. High performance polymers for membrane separation. *Polymer,* 35(23), pp. 4970-4978.

Sadorsky, P., 2013. Do urbanization and industrialization affect energy intensity in developing countries?. *Energy economics,* Volume 37, pp. 52-59.

Scholes, C., Smith, K., Kentish, S. & Stevens, G., 2010. CO2 capture frompre-combustionprocesses—Strategiesformembrane gas separation. *Intarnational Journal of Greenhouse Gas Control,* Volume 4, pp. 739-755.

Shen, Y. & Lua, A., 2012. Preparation and characterization of mixed matrix membranes based on poly(vinylidene fluoride) and zeolite 4A for gas separation. *Polymer engineering science,* Volume 52, pp. 2106-2113.

Singh, T., Kang, D.-Y. & Nair, S., 2013. Rigorous calculations of permeation in mixed-matrix membranes: Evaluation of interfacial equilibrium effects and permeability-based models. *Journal of membrane science,* Volume 448, pp. 160-169.

Sing, K., 1985. Reporting Physisorption Data for Gas/Solid Systems with Special Reference to the Determination of Surface Area and Porosity. *Pure and Applied Chemistry,* Volume 57, pp. 603-619.

Smith, B., Loganathan, M. & Shantha, M., 2010. A review of the water-gas shift reaction kinetics. *International journal of chemical reactor engineering,* 8(Review R4).

Song, Q. et al., 2012. Zeolitic imidazolate framework (ZIF-8) based polymer nanocomposite membranes for gas separation. *Energy and environmental science,* Volume 5, pp. 8359-8369.

Suer, M., BaC, N. & Yilmaz, L., 1994. Gas permeation characteristics of polymer-zeolite mixed matrix membranes. *Journal of membrane science,* Volume 91, pp. 77-86.

Takahashi, N. & Kuroda, K., 2011. Material design of layered silicates through covalent modification of interlayer surfaces. *Journal of materials chemistry,* Volume 21, pp. 14336-14353.

Takahashi, S. & Paul, D. R., 2006. Gas permeation in poly(ether imide) nanocomposite membranes based on surface-treated silica. Part 1: Without chemical coupling to matrix. *Polymer,* 47(21), pp. 7519-7534.

Tin, P. et al., 2003. Effects of cross-linking modification on gas separation performance of Matrimid membranes. *Journal of membrane science,* Volume 225, pp. 77-90.

Tsai, H. A., Huang, D. H., Ruaan, R. C. & Lai, J. Y., 2001. Mechanical Properties of Asymmetric Polysulfone Membranes Containing Surfactant as Additives. *Industrial and Engineering Chemistry Research,* 40(25), pp. 5917-5922.

Vaezi, M. & Babaluo, A., 2014. Effect of dehydration temperature on the H2 separation potential of hydroxy sodalite zeolite membranes. *Iranian Journal of Hydrogen & Fuel Cell,* Volume 4, pp. 209-214.

Visser, T., Masetto, N. & Wessling, M., 2007. Materials dependence of mixed gas plasticization behavior in asymmetric membranes. *Journal of membrane science,* 306(1-2), pp. 16-28.

Vu, D., Koros, W. & Miller, S., 2003. Mixed matrix membranes using carbon molecular sieves 1. Preparation and experimental results. *Journal of membrane science,* Volume 211, p. 311.

Wang, L.-J. & Hong, F. C.-N., 2005. Effects of surface treatments and annealing on carbon-based molecular sieve membranes for gas separation. *Applied Surface Science,* 240(1-4), pp. 161-174.

Wang, Y. X., Gies, H. & Marler, B., 2005. Synthesis and Crystal Structure of Zeolite RUB-41 Obtained as Calcination Product of a Layered Precursor: a Systematic Approach to a New Synthesis Route. *Chemistry of materials,* 17(1), pp. 43-49.

Wang, Z. et al., 2001. Pure-Silica Zeolite Low-k Dielectric Thin Films. *Advanced materials,* 13(10), pp. 746-749.

Weng, T., Tseng, H. & Wey, M., 2010. Fabrication and characterization of poly(phenylene oxide)/SBA-15/carbon molecule sieve multilayer mixed matrix membrane for gas separation. *International journal of hydrogen energy,* Volume 35, pp. 6971-6983.

Wennersten, R., Sun, Q. & Li, H., 2015. The future potential for Carbon Capture and Storage in climate change mitigation e an overview from perspectives of technology, economy and risk. *Journal of Cleaner Production,* Volume 103, pp. 724-736.

World Bank group, 2010. *World Development Report 2010: Development and Climate Change.* washington, DC: The World bank.

Xu, X. et al., 2004. Microwave-assisted hydrothermal synthesis of hydroxy-sodalite zeolite membrane. *Microporous and Mesoporous Materials,* 75(3), pp. 173-181.

Zhang, P., 2016. *Adsorption and Desorption Isotherms.* s.l.:Ke Research Group.

Zhao, Z. et al., 2013. Insights into the topotactic conversion process from layered silicate RUB-36 to FER-type zeolite by layer reassembly. *Chemistry of minerals,* Volume 25, pp. 840-847.

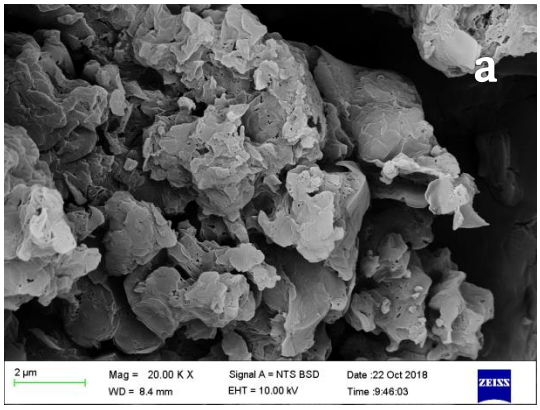
Zheng, Z., Guliants, V. & Misture, S., 2009. Sodalites as ultramicroporous frameworks for hydrogen separation at elevated temperatures : thermal stability, template removal , and hydrogen accessibility. *Journal of porous materials,* Volume 16, p. 343.

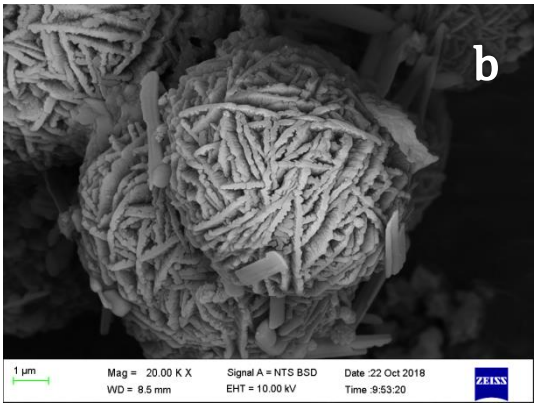
Zornoza, B. et al., 2013. Metal organic framework based mixed matrix membranes: An increasingly important field of research with a large application potential. *Microporous and Mesoporous Materials,* Volume 166, pp. 67-78.

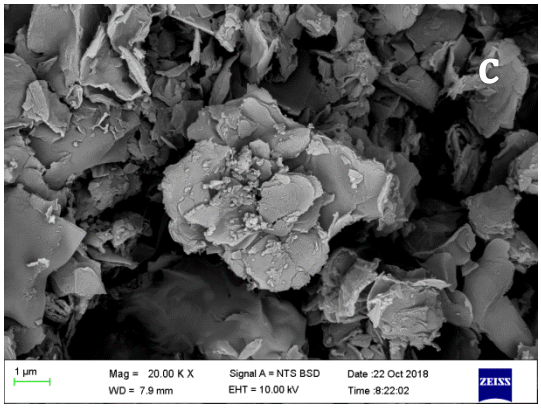
Appendix A: Supplementary data and imaging

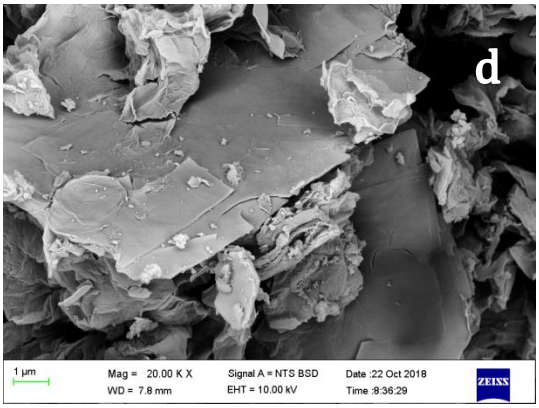
A.1) Chapter 4 additional images

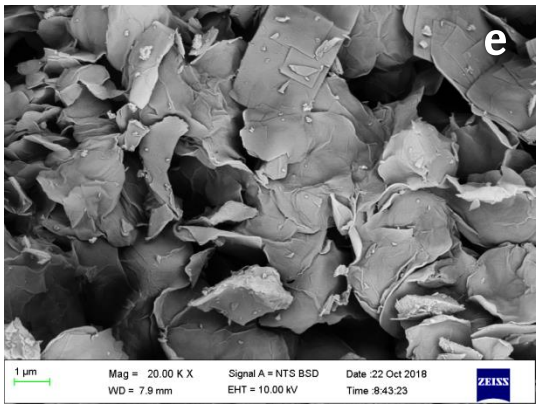
Figure A: SEM imaging for synthesized samples a)RUB-15; b)HSOD; c)SSOD1; d)SSOD2; e)SSOD3; f)SSOD4; g)SSOD5; h)SSOD6; i)SSOD7; j)SSOD8; k)SSOD9

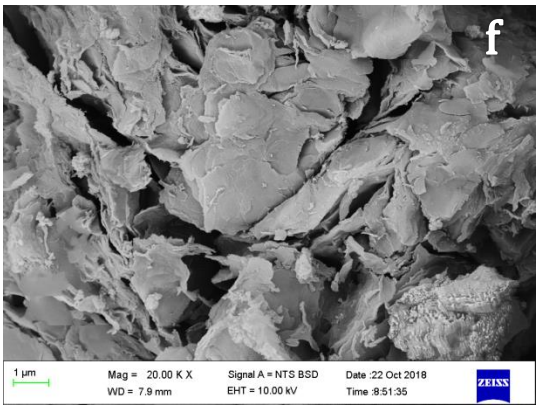


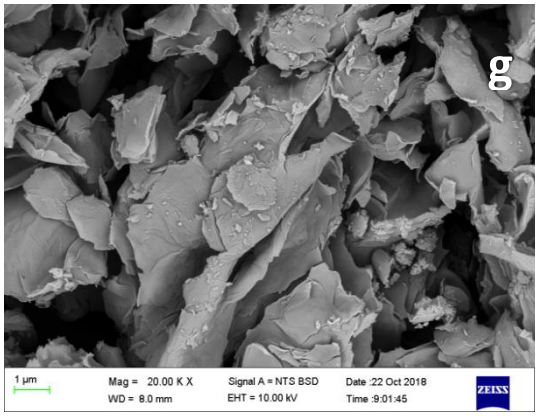


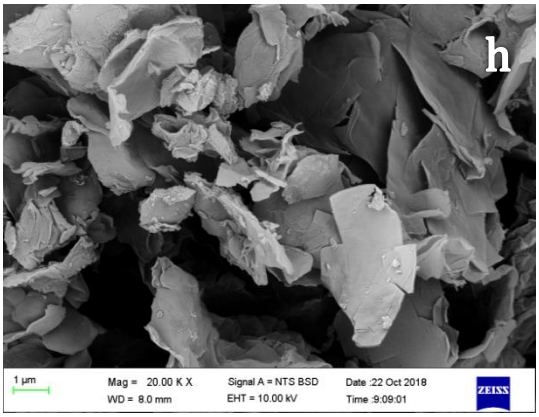


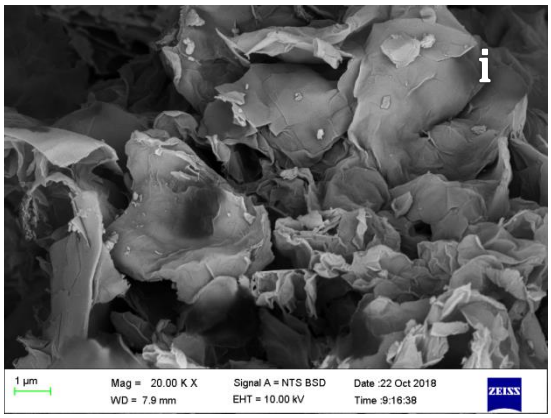


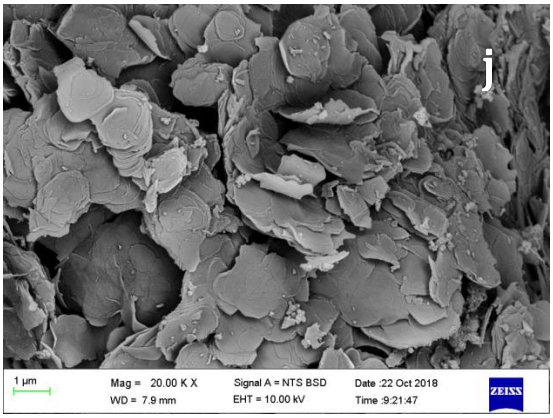


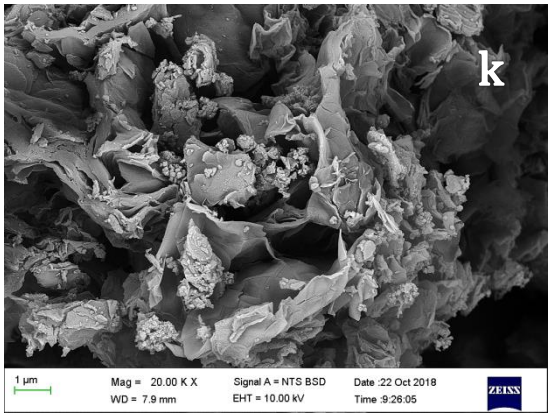



g
1 µm
Mag = 20.00 K X
WD = 8.0 mm
Signal A = NTS BSD
EHT = 10.00 kV
Date :22 Oct 2018
Time :9:01:45
ZEISS


h
1 µm
Mag = 20.00 K X
WD = 8.0 mm
Signal A = NTS BSD
EHT = 10.00 kV
Date :22 Oct 2018
Time :9:09:01
ZEISS

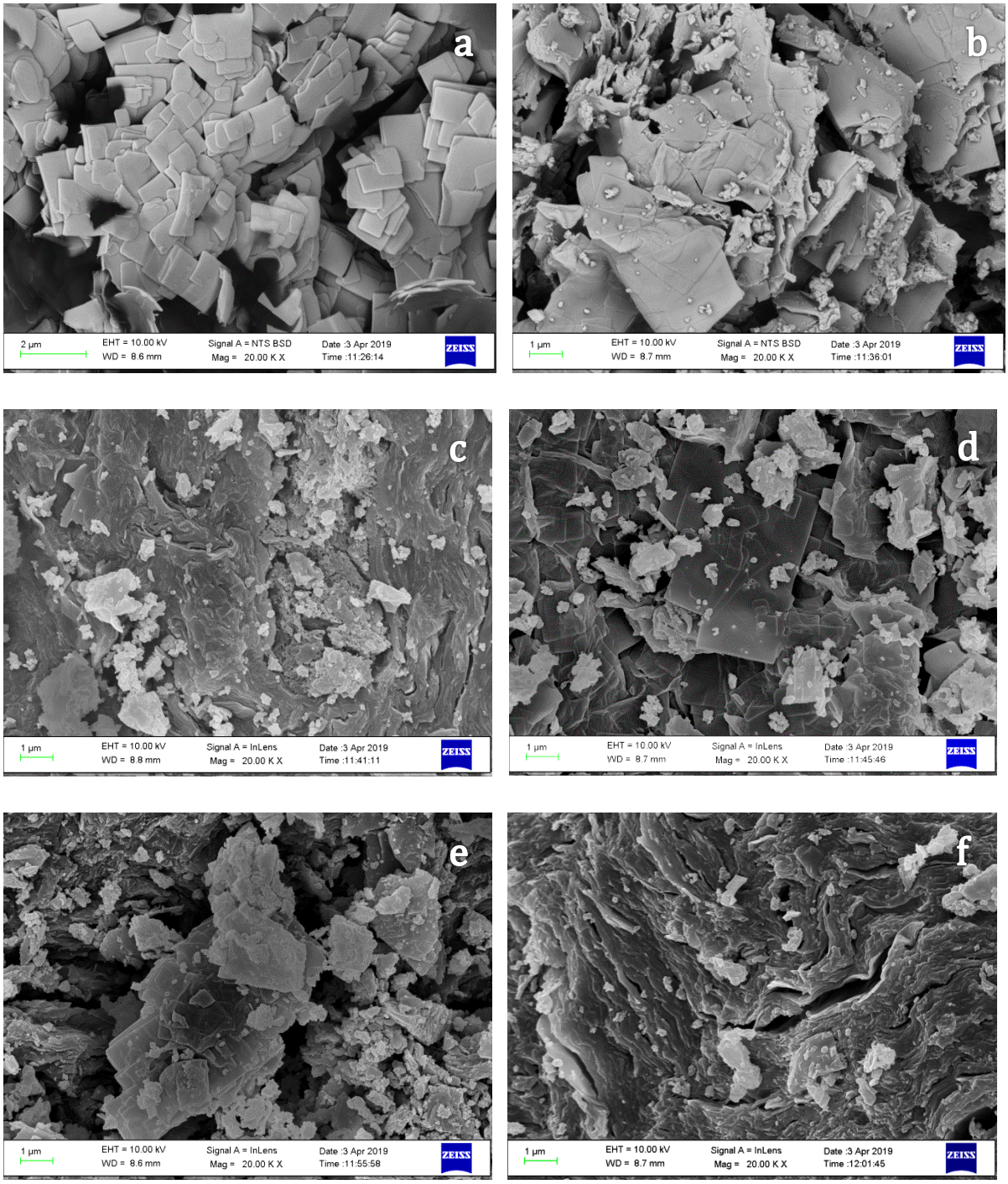

i
1 µm
Mag = 20.00 K X
WD = 7.9 mm
Signal A = NTS BSD
EHT = 10.00 kV
Date :22 Oct 2018
Time :9:16:38
ZEISS

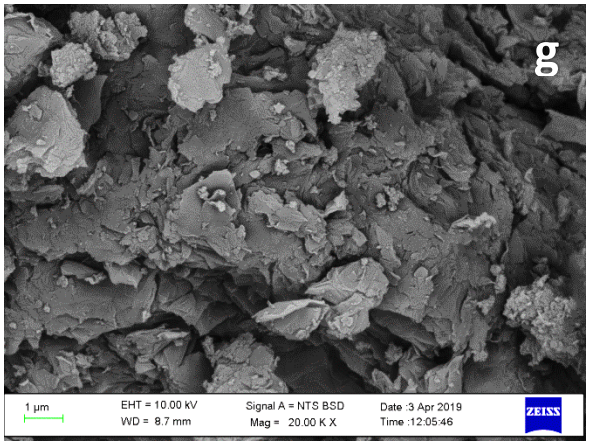

j
1 µm
Mag = 20.00 K X
WD = 7.9 mm
Signal A = NTS BSD
EHT = 10.00 kV
Date :22 Oct 2018
Time :9:21:47
ZEISS


k
1 µm
Mag = 20.00 K X
WD = 7.9 mm
Signal A = NTS BSD
EHT = 10.00 kV
Date :22 Oct 2018
Time :9:26:05
ZEISS

A.2) Chapter 5 additional images

Figure B: SEM imaging for synthesized samples a)RUB-15; b)SSOD6; c)SSOD9; d)OPT1; e)OPT2; f)OPT3; g)OPT4





A.3) Chapter 7 additional dataTable 18: Membrane thickness for single gas permeations

Membrane	wt%	Average thickness (cm)			
		1	2	3	4
PSF	0	0.00472	0.00818	0.00454	0.00546
HSOD	5	0.0096	0.00864	0.00492	0.00742
SSOD	5	0.0091	0.00408	0.00482	0.00398
SSOD	10	0.00594	0.00494	0.00614	0.0055
SSOD	15	0.00418	0.00484	0.00548	0.00708

Table 19: Robeson updated upper limit data (Appendix E.1)

H_2 Permeability (barrer)	H_2 Permeability (mol.m/m^2.s.Pa)	Selectivity H_2/CO_2
0.0545	1.83E-17	100.9
1.753	5.87E-16	23.1
31.9	1.07E-14	8.05
13.9	4.66E-15	0.495
16.2	5.43E-15	0.489
20.4	6.83E-15	0.538
23.3	7.81E-15	0.53

Table 20: H_2 single gas permeation results (averages of 4 membranes)

Membrane	Inlet Pressure (barg)	Flowrate (ml/min)	Temperature (°C)	Pressure drop (bar)	Permeability (cm^3(STP)/cm.s.bar)	Permeability (mol.m/m^2.s.Pa)	Permeance (mol/m^2.s.Pa)
PSF	1	38	24	1	0.00014	6.22E-12	2.73E-09
	2	54		2	0.00018	8.01E-12	2.07E-09
	3	66		3	0.00018	7.85E-12	1.71E-09
	4	82		4	0.00018	8.24E-12	1.59E-09
	5	94		5	0.00018	8.10E-12	1.46E-09
HSOD	1	103	25.75	1	0.00148	6.59E-11	7.31E-09
	2	110		2	0.00081	3.62E-11	4.24E-09
	3	109		3	0.00054	2.41E-11	2.82E-09
	4	110		4	0.00041	1.81E-11	2.13E-09
	5	109		5	0.00033	1.46E-11	1.69E-09
SSOD 5%	1	108	22.5	1	0.00095	4.24E-11	7.75E-09
	2	109		2	0.00052	2.31E-11	4.22E-09
	3	109		3	0.00035	1.55E-11	2.83E-09
	4	110		4	0.00026	1.17E-11	2.13E-09
	5	110		5	0.00021	9.35E-12	1.71E-09
SSOD 10%	1	106	25.25	1	0.00095	4.25E-11	7.54E-09
	2	107		2	0.00052	2.33E-11	4.14E-09
	3	107		3	0.00035	1.56E-11	2.77E-09

	4	107		4	0.00026	1.17E-11	2.08E-09
	5	107		5	0.00021	9.36E-12	1.66E-09
SSOD 15%	1	107	24	1	0.00093	4.14E-11	7.65E-09
	2	108		2	0.00051	2.26E-11	4.18E-09
	3	108		3	0.00034	1.51E-11	2.79E-09
	4	108		4	0.00025	1.13E-11	2.1E-09
	5	109		5	0.00020	9.10E-12	1.69E-09

Table 21: N_2 single gas permeation results (averages of 4 membranes)

Membrane	Inlet Pressure (barg)	Flowrate (ml/min)	Temperature (°C)	Pressure drop (bar)	Permeability (cm^3(STP)/cm.s.bar)	Permeability (mol.m/m^2.s.Pa)	Permeance (mol/m^2.s.Pa)
PSF	1	28	24	1	0.000028	1.25E-12	1.98E-09
	2	31		2	0.000034	1.53E-12	1.18E-09
	3	34		3	0.000035	1.56E-12	8.65E-10
	4	37		4	0.000037	1.66E-12	7.07E-10
	5	40		5	0.000039	1.73E-12	6.18E-10
HSOD	1	82	24	1	0.001406	6.28E-11	5.84E-09
	2	87		2	0.000766	3.42E-11	3.36E-09
	3	91		3	0.000512	2.29E-11	2.36E-09
	4	97		4	0.000384	1.72E-11	1.87E-09
	5	101		5	0.000307	1.37E-11	1.56E-09
SSOD 5%	1	84	22.75	1	0.000628	2.81E-11	5.99E-09

	2	92		2	0.000401	1.79E-11	3.55E-09
	3	99		3	0.000307	1.37E-11	2.56E-09
	4	104		4	0.000250	1.12E-11	2.02E-09
	5	103		5	0.000197	8.77E-12	1.60E-09
SSOD 10%	1	103	23	1	0.000927	4.14E-11	7.35E-09
	2	104		2	0.000506	2.26E-11	4.01E-09
	3	104		3	0.000338	1.51E-11	2.68E-09
	4	103		4	0.000253	1.13E-11	2.00E-09
	5	103		5	0.000202	9.02E-12	1.60E-09
SSOD 15%	1	103	23.5	1	0.000885	3.95E-11	7.31E-09
	2	103		2	0.000482	2.15E-11	3.99E-09
	3	103		3	0.000321	1.43E-11	2.66E-09
	4	103		4	0.000241	1.08E-11	1.99E-09
	5	103		5	0.000194	8.64E-12	1.60E-09

Table 22: CO_2 single gas permeation results (averages of 4 membranes)

Membrane	Inlet Pressure (barg)	Flowrate (ml/min)	Temperature (°C)	Pressure drop (bar)	Permeability (cm^3(STP)/cm.s.bar)	Permeability (mol.m/m^2.s.Pa)	Permeance (mol/m^2.s.Pa)
PSF	1	28	21.75	1	0.00003	1.24E-12	1.97E-09
	2	32		2	0.00004	1.98E-12	1.24E-09
	3	36		3	0.00005	2.13E-12	9.30E-10
	4	40		4	0.00005	2.24E-12	7.80E-10

	5	44		5	0.00005	2.27E-12	6.86E-10
HSOD	1	78	23.5	1	0.00138	6.17E-11	5.55E-09
	2	80		2	0.00075	3.35E-11	3.11E-09
	3	83		3	0.00050	2.24E-11	2.14E-09
	4	86		4	0.00038	1.67E-11	1.67E-09
	5	89		5	0.00030	1.34E-11	1.38E-09
SSOD 5%	1	81	23.25	1	0.00059	2.65E-11	5.77E-09
	2	90		2	0.00039	1.75E-11	3.47E-09
	3	97		3	0.00030	1.33E-11	2.50E-09
	4	100		4	0.00024	1.07E-11	1.94E-09
	5	101		5	0.00019	8.55E-12	1.56E-09
SSOD 10%	1	102	24.25	1	0.00092	4.09E-11	7.26E-09
	2	102		2	0.00050	2.22E-11	3.95E-09
	3	102		3	0.00033	1.48E-11	2.63E-09
	4	101		4	0.00025	1.11E-11	1.96E-09
	5	101		5	0.00020	8.85E-12	1.57E-09
SSOD 15%	1	101	24.25	1	0.00087	3.88E-11	7.19E-09
	2	101		2	0.00047	2.12E-11	3.92E-09
	3	101		3	0.00032	1.41E-11	2.62E-09
	4	101		4	0.00024	1.05E-11	1.95E-09
	5	101		5	0.00019	8.44E-12	1.56E-09

Table 23: Mixed gas ($60H_2$:$40CO_2$) separation data

Trial	Set Pressure (bar)	Flowrate (ml/min)	Temperature (°C)	Area (uV.min)		Presure drop (bar)	Thickness (cm)
				H_2	CO_2		
PSF	1	32	25	10664.0	2199.1	1	0.00498
	2	56		10212.5	3804.9	2	0.00498
	3	77		24741.1	3679.4	3	0.00498
	4	100		8434.7	2334.4	4	0.00498
	5	113		1144.2	55.3	5	0.00498
HSOD	1	106	24	1846.3	113.0	1	0.00428
	2	183		15671.1	2794.1	2	0.00428
	3	260		1791.5	122.7	3	0.00428
	4	328		12630.2	3849.4	4	0.00428
	5	396		22361.4	4783.1	5	0.00428
SSOD5%	1	50	25	26411.2	5069.7	1	0.00904
	2	82		8347.7	2598.4	2	0.00904
	3	115		6500.2	2063.1	3	0.00904
	4	143		31992.9	3955.1	4	0.00904
	5	175		40361.2	4740.7	5	0.00904
SSOD10%	1	53	25	23173.1	3487.7	1	0.00546
	2	117		7544.0	1806.0	2	0.00546
	3	170		29972.2	3828.9	3	0.00546

	4	180		6944.0	2110.7	4	0.00546
	5	153		22635.5	4082.9	5	0.00546
SSOD15%	1	91	24	14294.9	4510.8	1	0.00552
	2	206		29451.4	4309.6	2	0.00552
	3	337		46740.5	5448.0	3	0.00552
	4	368		48300.2	5073.2	4	0.00552
	5	295		43122.0	4808.4	5	0.00552

Table 24: Mixed gas ($60H_2$:$40CO_2$) calculated results

Membrane	Set Pressure (bar)	Xperm		Permeability (mol.m/m².s.Pa)		Selectivity H_2/CO_2	Permeance (mol/m².s.Pa)		SF
		H_2	CO_2	H_2	CO_2		H_2	CO_2	
PSF	1	0.767	0.233	2.45E-11	2.10E-11	1.75	4.92E-07	4.22E-07	2.19
	2	0.596	0.404	1.65E-11	2.48E-11	0.99	3.31E-07	4.99E-07	0.98
	3	0.610	0.390	1.52E-11	2.25E-11	1.01	3.05E-07	4.53E-07	1.04
	4	0.752	0.248	1.56E-11	2.05E-11	1.14	3.12E-07	4.11E-07	2.03
	5	0.994	0.006	1.49E-11	1.72E-11	1.31	3.00E-07	3.45E-07	112.97
HSOD	1	0.988	0.012	1.16E-10	4.48E-11	3.90	2.72E-06	1.05E-06	54.95
	2	0.704	0.296	5.01E-11	6.30E-11	1.19	1.17E-06	1.47E-06	1.58
	3	0.987	0.013	5.36E-11	5.21E-11	1.54	1.25E-06	1.22E-06	50.55
	4	0.592	0.408	4.16E-11	6.28E-11	0.99	9.71E-07	1.47E-06	0.97
	5	0.493	0.507	3.91E-11	6.32E-11	0.93	9.13E-07	1.48E-06	0.65

SSOD5%	1	0.462	0.538	4.49E-11	1.12E-10	0.60	4.97E-07	1.24E-06	0.57
	2	0.724	0.276	4.80E-11	5.83E-11	1.24	5.31E-07	6.45E-07	1.75
	3	0.781	0.219	4.47E-11	5.47E-11	1.23	4.95E-07	6.05E-07	2.38
	4	0.580	0.420	3.80E-11	5.80E-11	0.98	4.20E-07	6.41E-07	0.92
	5	0.497	0.503	3.64E-11	5.87E-11	0.93	4.03E-07	6.49E-07	0.66
SSOD10%	1	0.630	0.370	3.57E-11	4.84E-11	1.11	6.54E-07	8.86E-07	1.14
	2	0.808	0.192	4.42E-11	4.66E-11	1.42	8.09E-07	8.54E-07	2.81
	3	0.594	0.406	3.65E-11	5.52E-11	0.99	6.69E-07	1.01E-06	0.97
	4	0.776	0.224	3.10E-11	4.00E-11	1.16	5.67E-07	7.32E-07	2.31
	5	0.567	0.433	1.96E-11	3.01E-11	0.98	3.59E-07	5.51E-07	0.87
SSOD15%	1	0.521	0.479	5.36E-11	1.07E-10	0.76	9.71E-07	1.93E-06	0.73
	2	0.543	0.457	6.49E-11	1.08E-10	0.90	1.18E-06	1.95E-06	0.79
	3	0.422	0.578	6.80E-11	1.26E-10	0.81	1.23E-06	2.28E-06	0.49
	4	0.462	0.538	5.76E-11	9.74E-11	0.89	1.04E-06	1.77E-06	0.57
	5	0.490	0.510	3.74E-11	6.06E-11	0.93	6.78E-07	1.10E-06	0.64

A.4) RUB-15 Comparative XRD graphs from literature

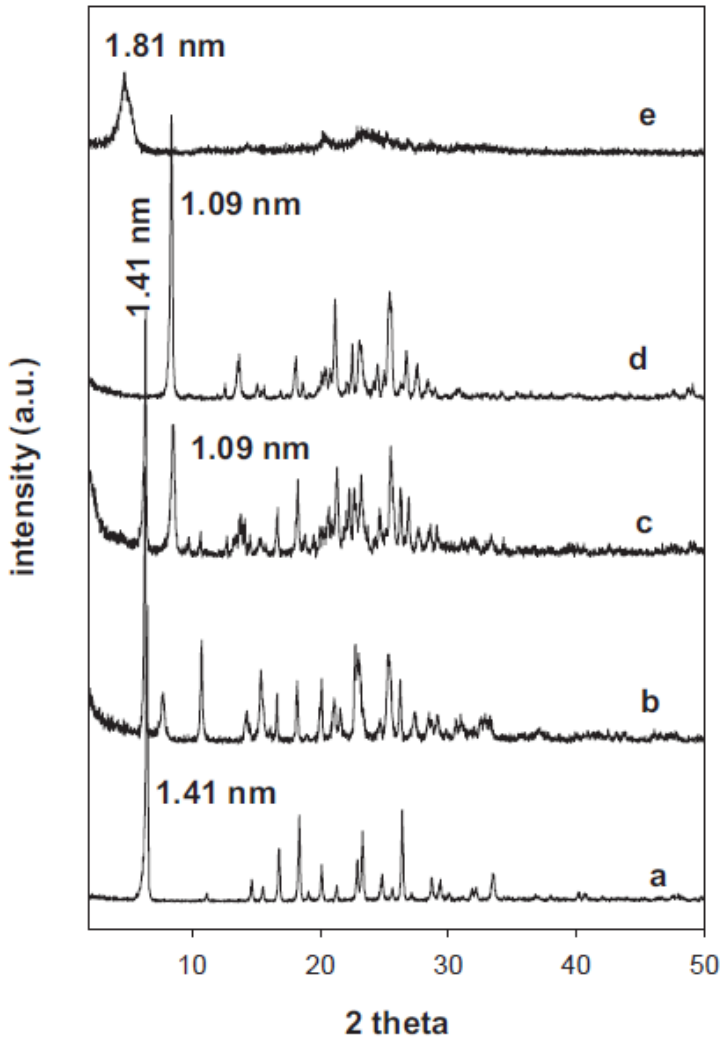


Fig. 2. Powder XRD of H-mag treated with $TMAOH.5H_2O$ at 150 °C with different amounts of water added. (a) sample 3 (b) sample 8, (c) sample 9, (d) sample 10, and (e) sample 11.

Figure as published by Kooli et al in A novel synthetic route to obtain RUB-15 phase by pseudo solid-state conversion (2016)

Copy right permission attained from Elsevier as per Appendix D.3

Appendix B: Design expert data

B.1) Preliminary Investigation

Surface Area candidate models

Linear model

Source	Sum of	df	Mean	F-value	p-value	
Model	2162.8	3	720.93	2.2582	0.1994	not significant
A-Concentration	158.99	1	158.99	0.498	0.5119	
B-Time	19.783	1	19.783	0.062	0.8133	
C-Temperature	1984	1	1984	6.2147	0.055	
Curvature	0	0				
Residual	1596.2	5	319.25			
Cor Total	3759	8				

Run	Actual	Predicted	Residual	Leverage	Internally	External	Cook's	Influence	Standard	(y-y')	(y-y')^2
1	42.91	50.69	-7.78	0.49	-0.61	-0.56	0.09	-0.55	4.00	-7.78	60.55
2	21.74	40.97	-19.23	0.11	-1.14	-1.19	0.04	-0.42	9.00	-19.23	369.96
3	70.54	53.83	16.70	0.49	1.30	1.44	0.40	1.40	2.00	16.70	278.99
4	42.27	31.25	11.01	0.49	0.86	0.83	0.17	0.81	5.00	11.01	121.32
5	18.85	19.19	-0.34	0.49	-0.03	-0.02	0.00	-0.02	8.00	-0.34	0.12
6	79.44	59.60	19.84	0.49	1.55	1.92	0.57	1.87	3.00	19.84	393.47
7	43.61	62.75	-19.14	0.49	-1.49	-1.80	0.53	-1.75	1.00	-19.14	366.36
8	26.02	28.11	-2.09	0.49	-0.16	-0.15	0.01	-0.14	7.00	-2.09	4.38
9	23.38	22.34	1.04	0.49	0.08	0.07	0.00	0.07	6.00	1.04	1.08
										SSE	1596.23
										MSE	177.36

2 Factor Interaction model

Source	Sum of	df	Mean	F-value	p-value	
Model	2636.2	6	439.37	0.7827	0.6551	not significant
A-Concentration	158.99	1	158.99	0.2832	0.6478	
B-Time	19.783	1	19.783	0.0352	0.8684	
C-Temperature	1984	1	1984	3.5341	0.2009	
AB	334.61	1	334.61	0.596	0.5208	
AC	33.833	1	33.833	0.0603	0.829	
BC	105.01	1	105.01	0.1871	0.7076	
Curvature	0	0				
Residual	1122.8	2	561.39			
Cor Total	3759	8				

Run	Actual	Predicted	Residual	Leverage	Internally	External	Cook's	Influence	Standard	(y-y')	(y-y')^2
1	42.91	49.90	-6.99	0.86	-0.79	-0.68	0.56	-1.68	4.00	-6.99	48.91
2	21.74	40.97	-19.23	0.11	-0.86	-0.77	0.01	-0.27	9.00	-19.23	369.96
3	70.54	58.73	11.80	0.86	1.34	2.89	1.58	7.20	2.00	11.80	139.29
4	42.27	30.47	11.80	0.86	1.34	2.89	1.58	7.20	5.00	11.80	139.29
5	18.85	7.05	11.80	0.86	1.34	2.89	1.58	7.20	8.00	11.80	139.29
6	79.44	67.64	11.80	0.86	1.34	2.89	1.58	7.20	3.00	11.80	139.29
7	43.61	50.60	-6.99	0.86	-0.79	-0.68	0.56	-1.68	1.00	-6.99	48.91
8	26.02	33.01	-6.99	0.86	-0.79	-0.68	0.56	-1.68	7.00	-6.99	48.91
9	23.38	30.37	-6.99	0.86	-0.79	-0.68	0.56	-1.68	6.00	-6.99	48.91
										SSE	1122.78
										MSE	124.75

3 factor interaction model

Source	Sum of	df	Mean	F-value	p-value	
Model	3342.8	7	477.54	1.1474	0.6184	not significant
A-Concentration	158.99	1	158.99	0.382	0.6476	
B-Time	19.783	1	19.783	0.0475	0.8633	
C-Temperature	1984	1	1984	4.7669	0.2734	
AB	334.61	1	334.61	0.804	0.5347	
AC	33.833	1	33.833	0.0813	0.8232	
BC	105.01	1	105.01	0.2523	0.7037	
Curvature	0	0				
ABC	706.57	1	706.57	1.6976	0.4167	
Residual	416.21	1	416.21			
Cor Total	3759	8				

Run	Actual	Predicted	Residual	Leverage	Internally	External	Cook's	Influence	Standard	(y-y')	(y-y')^2
1	42.91	40.50	2.40	0.99	1.00	0.00	8.88	0.00	4.00	2.40	5.78
2	21.74	40.97	-19.23	0.11	-1.00	0.00	0.02	0.00	9.00	-19.23	369.96
3	70.54	68.13	2.40	0.99	1.00	0.00	8.88	0.00	2.00	2.40	5.78
4	42.27	39.86	2.40	0.99	1.00	0.00	8.88	0.00	5.00	2.40	5.78
5	18.85	16.44	2.40	0.99	1.00	0.00	8.88	0.00	8.00	2.40	5.78
6	79.44	77.04	2.40	0.99	1.00	0.00	8.88	0.00	3.00	2.40	5.78
7	43.61	41.21	2.40	0.99	1.00	0.00	8.88	0.00	1.00	2.40	5.78
8	26.02	23.61	2.40	0.99	1.00	0.00	8.88	0.00	7.00	2.40	5.78
9	23.38	20.97	2.40	0.99	1.00	0.00	8.88	0.00	6.00	2.40	5.78
										SSE	416.21
										MSE	46.25

Significant model

Source	Sum of	df	Mean	F-value	p-value	
Model	1984	1	1984	7.8242	0.0266	significant
C-Temperature	1984	1	1984	7.8242	0.0266	
Curvature	0	0				
Residual	1775	7	253.57			
Cor Total	3759	8				

Term	Adjusted F-value	Model p-value	
Model	8.760693291	0.025287962	significant
Curvatur	1.837833262	0.224008007	

Std. Dev.	15.924		RÂ²	0.5278	PRESS	2876.1
Mean	40.971		Adjusted	0.4603	-2 Log Likelihood	73.1
C.V. %	38.866		Predicte	0.2349	BIC	77.494
			Adeq Pre	4.1958	AICc	79.1

Factor	Coefficient	df	Standard	95% CI	95% CI	VIF
Intercept	40.97	1.00	5.31	28.42	53.52	
C-Temperature	-15.75	1.00	5.63	-29.06	-2.44	1

Pore Volume candidate models

Linear model

Source	Sum of	df	Mean	F-value	p-value	
Model	0.000683	3	0.000228	2.732713	0.153466	not significant
A-Concentration	8.63E-05	1	8.63E-05	1.035938	0.355462	
B-Time	5.54E-06	1	5.54E-06	0.066462	0.806833	
C-Temperature	0.000591	1	0.000591	7.09574	0.044681	
Residual	0.000417	5	8.33E-05			
Cor Total	0.0011	8				

Run	Actual	Predicted	Residual	Leverage	Internally	Externally	Cook's	Influence	Standard	(y-y')	(y-y')^2
1	0.065	0.065	0.000	0.486	0.058	0.052	0.001	0.050	4	3.77E-04	1.42E-07
2	0.049	0.060	-0.012	0.111	-1.359	-1.531	0.058	-0.541	9	-1.17E-02	1.37E-04
3	0.072	0.067	0.005	0.486	0.792	0.758	0.148	0.737	2	5.18E-03	2.69E-05
4	0.064	0.056	0.008	0.486	1.238	1.329	0.362	1.293	5	8.10E-03	6.56E-05
5	0.046	0.048	-0.001	0.486	-0.229	-0.206	0.012	-0.200	8	-1.50E-03	2.24E-06
6	0.081	0.072	0.010	0.486	1.453	1.709	0.499	1.662	3	9.51E-03	9.04E-05
7	0.064	0.073	-0.009	0.486	-1.409	-1.623	0.469	-1.578	1	-9.22E-03	8.50E-05
8	0.052	0.054	-0.003	0.486	-0.388	-0.352	0.036	-0.342	7	-2.54E-03	6.44E-06
9	0.051	0.049	0.002	0.486	0.273	0.246	0.018	0.239	6	1.79E-03	3.19E-06
										SSE	4.17E-04
										MSE	4.63E-05

2 Factor interaction model

Source	Sum of	df	Mean	F-value	p-value	
Model	0.000827	6	0.000138	1.008763	0.575364	not significant
A-Concentration	8.63E-05	1	8.63E-05	0.632057	0.509961	
B-Time	5.54E-06	1	5.54E-06	0.040551	0.85903	
C-Temperature	0.000591	1	0.000591	4.329323	0.172951	
AB	3.27E-05	1	3.27E-05	0.239623	0.672903	
AC	1.39E-05	1	1.39E-05	0.1018	0.779921	
BC	9.69E-05	1	9.69E-05	0.709227	0.488354	
Curvature	0	0				
Residual	0.000273	2	0.000137			
Cor Total	0.0011	8				

Run	Actual	Predicted	Residual	Leverage	Internally	Externally	Cook's	Influence	Standard	(y-y')	(y-y')^2
1	0.065	0.068	-0.002	0.861	-0.551	-0.423	0.269	-1.053	4	-2.40E-03	5.75E-06
2	0.049	0.060	-0.012	0.111	-1.062	-1.136	0.020	-0.402	9	-1.17E-02	1.37E-04
3	0.072	0.066	0.005	0.861	1.222	1.717	1.323	4.276	2	5.32E-03	2.83E-05
4	0.064	0.059	0.005	0.861	1.222	1.717	1.323	4.276	5	5.32E-03	2.83E-05
5	0.046	0.041	0.005	0.861	1.222	1.717	1.323	4.276	8	5.32E-03	2.83E-05
6	0.081	0.076	0.005	0.861	1.222	1.717	1.323	4.276	3	5.32E-03	2.83E-05
7	0.064	0.066	-0.002	0.861	-0.551	-0.423	0.269	-1.053	1	-2.40E-03	5.75E-06
8	0.052	0.054	-0.002	0.861	-0.551	-0.423	0.269	-1.053	7	-2.40E-03	5.75E-06
9	0.051	0.054	-0.002	0.861	-0.551	-0.423	0.269	-1.053	6	-2.40E-03	5.75E-06
										SSE	2.73E-04
										MSE	3.03E-05

3 Factor interaction model

Source	Sum of	df	Mean	F-value	p-value	
Model	0.000946	7	0.000135	0.877922	0.678728	not significant
A-Concentration	8.63E-05	1	8.63E-05	0.560855	0.590782	
B-Time	5.54E-06	1	5.54E-06	0.035983	0.880657	
C-Temperature	0.000591	1	0.000591	3.841624	0.300342	
AB	3.27E-05	1	3.27E-05	0.212629	0.724942	
AC	1.39E-05	1	1.39E-05	0.090332	0.81413	
BC	9.69E-05	1	9.69E-05	0.629332	0.573054	
ABC	0.000119	1	0.000119	0.7747	0.540519	
Curvature	0	0				
Residual	0.000154	1	0.000154			
Cor Total	0.0011	8				

Run	Actual	Predicted	Residual	Leverage	Internally	Externally	Cook's	Influence	Standard	(y-y')	(y-y')^2
1	0.065	0.064	0.001	0.986	1	0.0	8.875	0	4	1.46E-03	2.14E-06
2	0.049	0.060	-0.012	0.111	-1	0.0	0.015625	0	9	-1.17E-02	1.37E-04
3	0.072	0.070	0.001	0.986	1	0.0	8.875	0	2	1.46E-03	2.14E-06
4	0.064	0.063	0.001	0.986	1	0.0	8.875	0	5	1.46E-03	2.14E-06
5	0.046	0.045	0.001	0.986	1	0.0	8.875	0	8	1.46E-03	2.14E-06
6	0.081	0.080	0.001	0.986	1	0.0	8.875	0	3	1.46E-03	2.14E-06
7	0.064	0.062	0.001	0.986	1	0.0	8.875	0	1	1.46E-03	2.14E-06
8	0.052	0.050	0.001	0.986	1	0.0	8.875	0	7	1.46E-03	2.14E-06
9	0.051	0.050	0.001	0.986	1	0.0	8.875	0	6	1.46E-03	2.14E-06
										SSE	1.54E-04
										MSE	1.71E-05

Significant model

Source	Sum of	df	Mean	F-value	p-value	
Model	0.000678	2	0.000339	6.314602	0.042839	significant
A-Concentration	8.63E-05	1	8.63E-05	1.608902	0.260494	
C-Temperature	0.000591	1	0.000591	11.0203	0.021016	
Curvature	0.000154	1	0.000154	2.868657	0.151097	
Residual	0.000268	5	5.36E-05			
Cor Total	0.0011	8				

Std. Dev.	0.007325		RÂ²	0.71638
Mean	0.060457		Adjusted	0.602932
C.V. %	12.11531		Predicted	NAâ€“Â¹â€“
			Adeq Pre	5.12789

Factor	Coefficien	df	Standard	95% CI	VIF
Intercept	0.061919	1	0.00259	0.05526	
A-Concen	-0.00328	1	0.00259	-0.00994	1.00E+00
C-Temper	-0.0086	1	0.00259	-0.01525	1.00E+00
Ctr Pt 1	-0.01316	1	0.007769		

Run	Actual	Predicted	Residual	Leverage	Internally	Externally	Cook's	Influence	Standard	(y-y')	(y-y')^2
1	0.065314	0.067231	-0.00192	0.375	-0.3311	-0.299443663	0.016444	-0.23195	4	-0.00192	3.68E-06
9	0.048761	0.048761	0	1					9	0	0
3	0.071785	0.067231	0.004554	0.375	0.786406	0.751383973	0.092765	0.58202	2	0.004554	2.07E-05
8	0.064075	0.056607	0.007468	0.375	1.289636	1.411983443	0.249474	1.093718	5	0.007468	5.58E-05
5	0.046246	0.050038	-0.00379	0.375	-0.65481	-0.612535202	0.064317	-0.47447	8	-0.00379	1.44E-05
2	0.081013	0.073801	0.007212	0.375	1.245513	1.341376317	0.232695	1.039026	3	0.007212	5.2E-05
4	0.063952	0.073801	-0.00985	0.375	-1.70082	-2.343337079	0.433919	-1.81514	1	-0.00985	9.7E-05
6	0.051776	0.056607	-0.00483	0.375	-0.83433	-0.80433328	0.104416	-0.62303	7	-0.00483	2.33E-05
7	0.051193	0.050038	0.001155	0.375	0.199505	0.179157053	0.00597	0.138774	6	0.001155	1.33E-06
										SSE	0.000268
										MSE	2.98E-05

B.2) Extended Investigation

Surface Area model

Lack of fit summary

Source	SOS	df	Meas square	F-value	P-value
Linear	0.061	0.353	0.332	-0.060	
2FI	0.068	0.515	0.605	0.067	Suggested
Quadratic	0.910	0.333	0.427	-1.609	
Cubic	0.333		0.661		Aliased

Source	SOS	df	Meas squ	F-value	P-value	
Mean vs Total	63838.4	1	63838			
Linear vs Mean	6521.8	3	2173.9	3.315	0.061	
2FI vs Linear	4109.4	3	1369.8	3.531	0.068	Suggeste
Quadratic vs 2FI	292.2	3	97.408	0.173	0.910	
Cubic vs Quadratic	2146.3	3	715.42	2.151	0.333	Aliased
Residual	665.3	2	332.67			
Total	77573.4	15	5171.6			

Source	SOS	df	Meas squ	F-value	P-value	
Linear	6547.9	9	727.54	2.187	0.353	
2FI	2438.5	6	406.42	1.222	0.515	Suggeste
Quadratic	2146.3	3	715.42	2.151	0.333	
Cubic	0.0	0				Aliased
Pure Error	665.3	2	332.67			

Source	std. dev	R2	Adjusted R2	Predicted R2	PRESS	
Linear	25.608	0.475	0.332	-0.060	14566	
2FI	19.697	0.774	0.605	0.067	12821	Suggested
Quadratic	23.713	0.795	0.427	-1.609	35837	
Cubic	18.239	0.952	0.661		*	Aliased

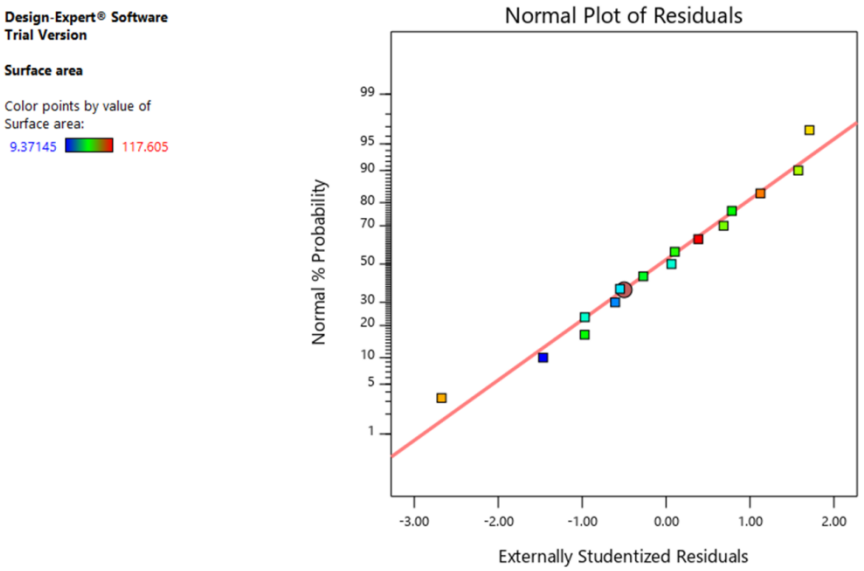
Significant model

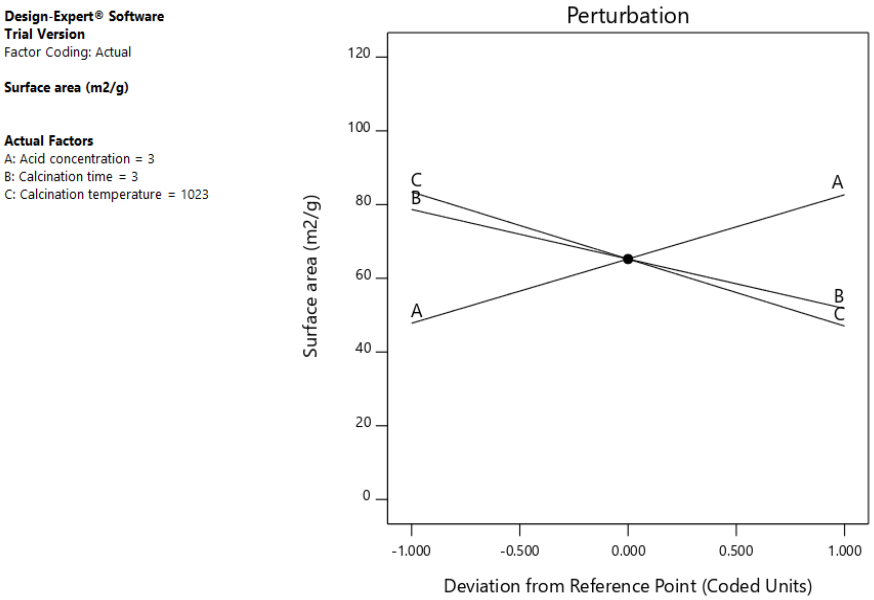
Source	SOS	df	Meas square	F-value	P-value	
Model	10 631.16	6	1 771.86	4.5669	0.0263	significant
A-Acid concentration	2 429.53	1	2 429.53	6.2620	0.0368	significant
B-Calcination time	1 444.02	1	1 444.02	3.7219	0.0898	
C-Calcination temperatur	2 648.23	1	2 648.23	6.8257	0.0310	significant
AB	3 415.56	1	3 415.56	8.8035	0.0180	significant
AC	526.48	1	526.48	1.3570	0.2776	
BC	167.34	1	167.34	0.4313	0.5298	
Residual	3 103.83	8	387.98			
Lack of Fit	2 438.49	6	406.42	1.2217	0.5151	not significant
Pure Error	665.33	2	332.67			
Cor Total	13 734.98	14				

Std. Dev.	19.7		RÂ²	0.77402
Mean	65.2		Adjusted	0.60454
C.V. %	30.2		Predicted	0.06654
			Adeq Pre	7.29657

Factor	Coefficient estimate	df	std error	95% Cl low	95% Cl high	VIF
Intercept	65.2372133	1	5.08578558	53.509371	76.965056	
A-Acid concentration	17.426725	1	6.96399872	1.3677152	33.485735	1
B-Calcination time	-13.435144	1	6.96399872	-29.49415	2.6238661	1
C-Calcination temperatur	-18.194194	1	6.96399872	-34.2532	-2.135184	1
AB	-29.221388	1	9.84858143	-51.93226	-6.510518	1
AC	-11.472538	1	9.84858143	-34.18341	11.238332	1
BC	-6.46805	1	9.84858143	-29.17892	16.24282	1

Run order	actual value	predicted	residual	leverge	internally studentized residuals	externally SR	cook's distance	influence on fitted value DFFITS	STD order		(Y-Y2)^2
1	23.82	32.02	-8.20	0.57	-0.63	-0.61	0.07	-0.69	1		67.255
2	99.25	125.32	-26.08	0.57	-2.01	-2.68	0.76	-3.06	2		679.92
3	82.36	63.60	18.76	0.57	1.45	1.58	0.39	1.80	3		352.11
4	40.90	40.01	0.89	0.57	0.07	0.06	0.00	0.07	4		0.7924
5	41.93	54.53	-12.60	0.57	-0.97	-0.97	0.18	-1.11	5		158.77
6	117.60	112.33	5.27	0.57	0.41	0.38	0.03	0.44	6		27.816
7	33.64	41.09	-7.45	0.57	-0.57	-0.55	0.06	-0.63	7		55.54
8	63.42	53.00	10.42	0.57	0.80	0.78	0.12	0.90	8		108.62
9	104.74	90.40	14.34	0.57	1.11	1.12	0.23	1.29	9		205.78
10	63.84	76.46	-12.62	0.57	-0.97	-0.97	0.18	-1.11	10		159.28
11	76.14	66.95	9.20	0.57	0.71	0.69	0.09	0.78	11		84.587
12	9.37	27.14	-17.77	0.57	-1.37	-1.47	0.35	-1.68	12		315.72
13	59.74	65.24	-5.50	0.07	-0.29	-0.27	0.00	-0.07	13		30.211
14	67.35	65.24	2.12	0.07	0.11	0.10	0.00	0.03	14		4.478
15	94.44	65.24	29.21	0.07	1.53	1.71	0.02	0.46	15		852.96
										SSE	3103.8
										MSE	206.92





Pore Volume model

Lack of fit summary

Source	SOS	df	Meas square	F-value	P-value
Linear	0.116554	0.534194	0.239429	-0.160545	Suggested
2FI	0.7197624	0.454468	0.10721	-1.215511	
Quadratic	0.9063983	0.287839	-0.290086	-5.088894	
Cubic	0.2878393		0.346823		Aliased

Source	SOS	df	Meas squa	F-value	P-value	
Mean vs Total	0.07039	1	0.07039			
Linear vs Mean	0.00275	3	0.00092	2.4691	0.1166	Suggested
2FI vs Linear	0.0006	3	0.00020	0.457	0.7198	
Quadratic vs 2FI	0.00034	3	0.00011	0.1788	0.9064	
Cubic vs Quadrati	0.00251	3	0.00084	2.6252	0.2878	Aliased
Residual	0.00064	2	0.00032			
Total	0.07722	15	0.00515			

Source	SOS	df	Meas squa	F-value	P-value	
Linear	0.00344	9	0.000383	1.201	0.5342	Suggested
2FI	0.00285	6	0.000474	1.4891	0.4545	
Quadratic	0.00251	3	0.000836	2.6252	0.2878	
Cubic	0	0				Aliased
Pure Error	0.00064	2	0.000319			

Source	std. dev	R2	Adjusted R2	Predicted R2	PRESS	
Linear	0.019	0.4024	0.2394	-0.1605	0.0079	Suggested
2FI	0.021	0.4898	0.1072	-1.2155	0.0151	
Quadratic	0.025	0.5393	-0.2901	-5.0889	0.0416	
Cubic	0.018	0.9067	0.3468			Aliased

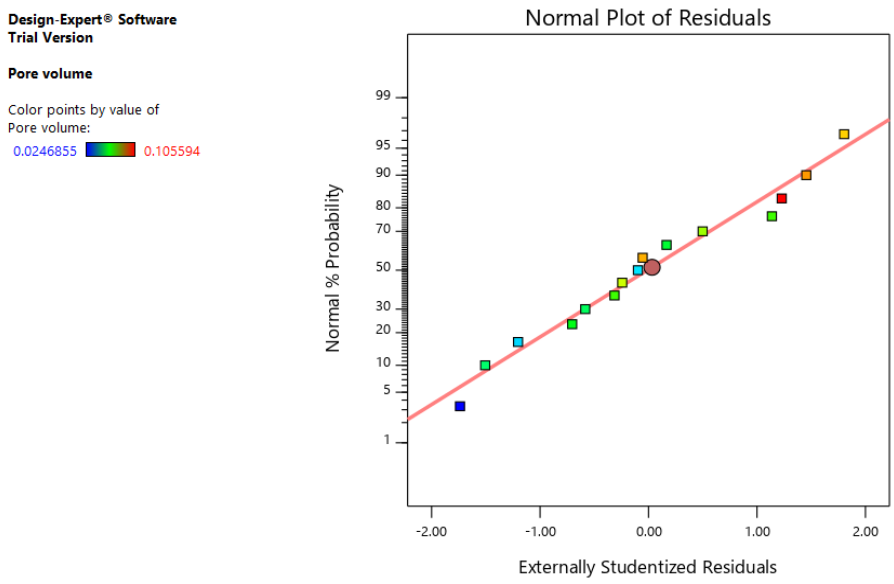
Significant model

Source	SOS	df	Meas square	F-value	P-value	
Model	0.0027	2	0.0014	3.96	0.048	significant
A-Acid concentrati	0.0004	1	0.0004	1.13	0.309	
C-Calcination temp	0.0023	1	0.0023	6.79	0.023	
Residual	0.0041	12	0.0003			
Lack of Fit	0.0035	10	0.0003	1.09	0.569	not significant
Pure Error	0.0006	2	0.0003			
Cor Total	0.0068	14				

Std. Dev.	0.01851		RÂ²	0.3977
Mean	0.06851		Adjusted R	0.2974
C.V. %	27.0228		Predicted F	0.0803
			Adeq Preci	5.8024

Factor	Coefficient estimate	df	std error	95% Cl low	95% Cl high	VIF
Intercept	0.0685051	1	0.0047798	0.0580909	0.0789	
A-Acid concentration	0.0069579	1	0.006545	-0.007302	0.0212	1
C-Calcination temperature	-0.017061	1	0.006545	-0.031321	-0.0028	1

Run order	actual value	predicted	residual	leverge	internally studentized residuals	externally SR	cook's dista	influence on fitted value DFFITS	STD order		(Y-Y2)^2
1	0.0419	0.0615	-0.0196	0.1917	-1.1806	-1.2023	0.1102	-0.5855	1		3.86E-04
2	0.0635	0.0755	-0.0120	0.1917	-0.7187	-0.7035	0.0408	-0.3425	2		1.43E-04
3	0.0891	0.0615	0.0275	0.1917	1.6549	1.8036	0.2165	0.8782	3		7.59E-04
4	0.0700	0.0755	-0.0054	0.1917	-0.3260	-0.3136	0.0084	-0.1527	4		2.94E-05
5	0.0567	0.0786	-0.0219	0.3167	-1.4323	-1.5060	0.3169	-1.0252	5		4.80E-04
6	0.0917	0.0925	-0.0009	0.3167	-0.0561	-0.0537	0.0005	-0.0366	6		7.37E-07
7	0.0429	0.0445	-0.0016	0.3167	-0.1020	-0.0977	0.0016	-0.0665	7		2.44E-06
8	0.0611	0.0584	0.0027	0.3167	0.1740	0.1668	0.0047	0.1135	8		7.09E-06
9	0.1056	0.0856	0.0200	0.1917	1.2033	1.2286	0.1144	0.5983	9		4.01E-04
10	0.0814	0.0856	-0.0042	0.1917	-0.2522	-0.2421	0.0050	-0.1179	10		1.76E-05
11	0.0702	0.0514	0.0187	0.1917	1.1243	1.1380	0.0999	0.5542	11		3.50E-04
12	0.0247	0.0514	-0.0268	0.1917	-1.6078	-1.7378	0.2043	-0.8462	12		7.16E-04
13	0.0578	0.0685	-0.0107	0.0667	-0.5996	-0.5829	0.0086	-0.1558	13		1.15E-04
14	0.0777	0.0685	0.0092	0.0667	0.5157	0.4993	0.0063	0.1334	14		8.51E-05
15	0.0934	0.0685	0.0249	0.0667	1.3916	1.4549	0.0461	0.3888	15		6.19E-04
										SSE	4.11E-03
										MSE	2.74E-04

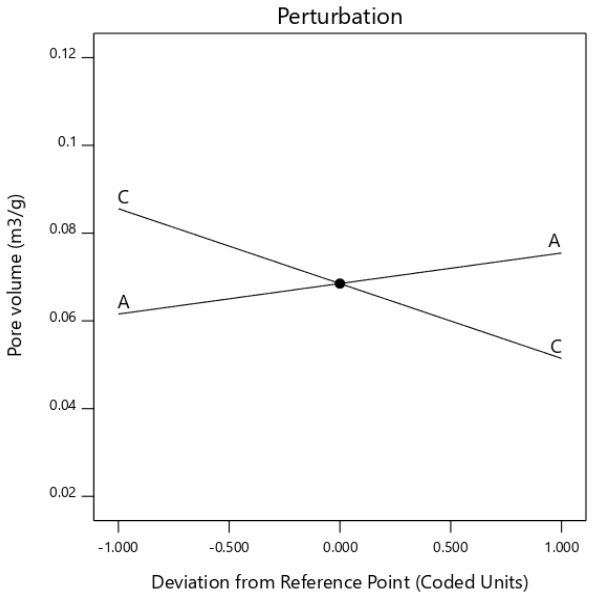


Design-Expert® Software
Trial Version
Factor Coding: Actual

Pore volume (m3/g)

Actual Factors
A: Acid concentration = 3
B: Calcination time = 3
C: Calcination temperature = 1023

Factors not in Model
B



Optimization

Name	goal	lower limit	upper limit	lower weight	upper weight	importance
A:Acid concentration	is in range	1	5	1	1	3
B:Calcination time	is in range	1	5	1	1	3
C:Calcination temperatur	is in range	873	1173	1	1	3
Surface area	maximize	9.37145	117.60475	1	1	3
Pore volume	maximize	0.02469	0.1055935	1	1	3

Appendix C: Operating procedures

C.1) Procedure for operating membrane gas separation system

As adapted from the dissertation by Oloye & Daramola (2017)

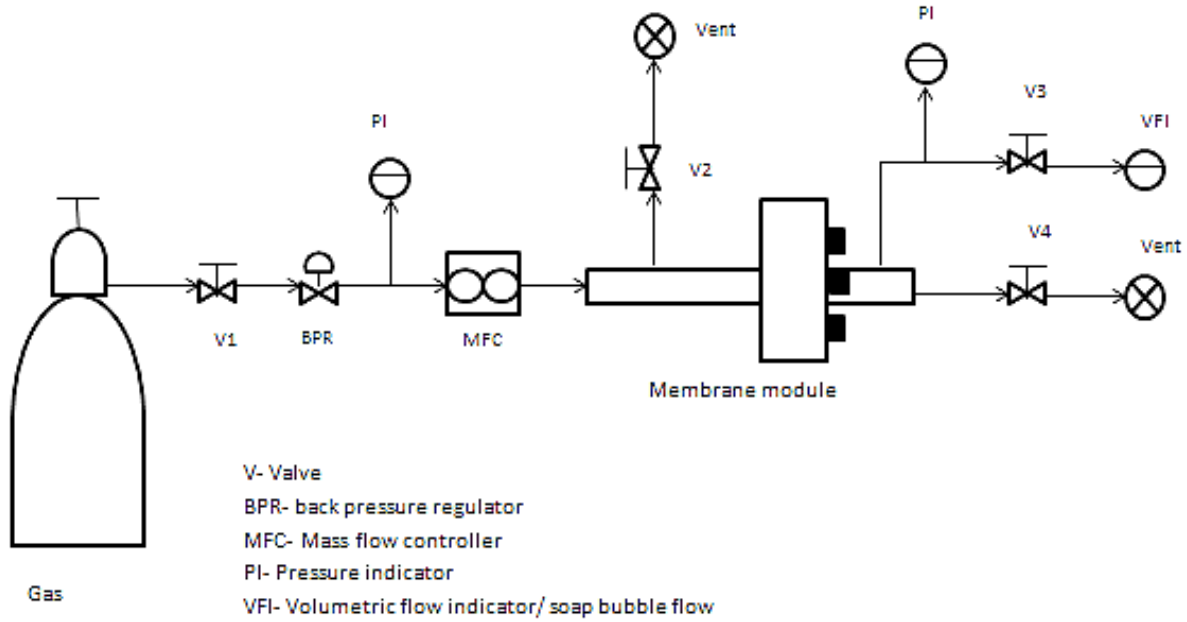


Figure 42: Schematic diagram of membrane gas separation rig



a) b)

Figure 43: a) membrane module and b) gas separation rig

Loading and preparing the membrane module

1. Cut membrane to circular template
2. Coat the sides of the membrane module with petroleum jelly
3. Carefully place the membrane in the module, ensuring the membrane aligns with the module
4. Replace the other half of the membrane module and crew in the bolts tightly using the spanner to prevent gas leakage
5. Screw in both end of the membrane module to the retentate and permeate lines, ensuring it is air-tight.

Setting the gas lines pressure and flow

1. Open gas cylinders and set to desired pressures
2. Open valves (V1, V2 & V4)
3. Adjusting the forward pressure regulators to set the individual gas inlet pressures to the desired pressures
4. Adjust the mass flow control by turning carefully the right hand screw of the mass flow controller.

Analysing the gas mixtures by GC

For the feed gas mixture:

1. Switch valve V9 to the back pressure regulator
2. Switch valve V10 to the feed position
3. Switch the gas line selector switch to FEED/RETENTATE
4. Trap the gas from the GC line and analyze with the GC until statistically repeatable results are obtained.

For the permeate gas:

1. Switch valve V9 to the reactor
2. Switch valve V10 to the retentate position
3. Switch the gas line selector switch to FEED/RETENTATE
4. Trap the gas from the GC line and analyze with the GC until statistically repeatable results are obtained.
5. Repeat the above till the desired results are obtained.

C.2) GC operating procedure

Gas Chromatography (Bruker 430-GC) Standard Operating Procedure developed for J. Smith

1. Ensure carrier gas valve is open. Located above machine to the right on silver panelling
2. Turn on black switch on bottom left of GC machine
3. Open compass CDS software
   Password: compass
4. On left hand side panel, go to system tab.
   Tick all boxed in system and by-type sub-tabs (bruker, chromatogram and status)
5. Open method
   >File >Open> Open method >choose a method of desired specs to display gasses (Haysep 5 chosen for H_2/CO_2)
6. Starting system/ running a sample
   >Acquisition> quick start> method (use drop down tab to select the method)> ok> insert run name> start
7. To check readiness of GC
   >system >overview> all 4 quadrants should be green and waiting for injection will be shown on the bottom of the screen
8. If the system is ready inject sample
   - Insert syringe needle into yellow tube on right hand side of GC
   - Open the valve on the syringe
   - Inject small quantity
   - Close syringe valve
   - Press PLAY (I>) button on GC interface
   - Allow sample to run full time
9. Once post run operations are finished your data is available
   >file >open >open chromatogram> select run
10. Analysing chromatogram
    - >add peak mode (icons bar at top) > use cursor to pin start and end of peak> right click on peak> peak> add to peak ID table
    - Repeat on all peaks
    - >process> reprocess > close
    - >results sub-tab to find area results
11. Pure gasses can be tested first to determine retention time of peaks
12. Convert area to a response factor to find concentration
    To calibrate: first run inlet sample to determine RF from known concentrations

$$RF = \frac{area\ (uv\text{min})}{concentration\ (mole\ frac)}$$

13. Fill in log-book and turn off machine when finished

Appendix D: Copy right permissions

D.1) Figure 1

This Agreement between Christin Eden ("You") and Elsevier ("Elsevier") consists of your license details and the terms and conditions provided by Elsevier and Copyright Clearance Centre.

License Number	4691820111411
License date	Oct 18, 2019
Licensed Content Publisher	Elsevier
Licensed Content Publication	Journal of Membrane Science
Licensed Content Title	The upper bound revisited
Licensed Content Author	Lloyd M. Robeson
Licensed Content Date	Jul 15, 2008
Licensed Content Volume	320
Licensed Content Issue	1-2
Licensed Content Pages	11
Start Page	390
End Page	400
Type of Use	reuse in a thesis/dissertation
Portion	figures/tables/illustrations
Number of figures/tables/illustrations	2

Format	both print and electronic
Are you the author of this Elsevier article?	No
Will you be translating?	No
Original figure numbers	Figure 10 and Table 10
Title of your thesis/dissertation	Synthesis and performance evaluation of optimized silica sodalite in polysulfone mixed matrix membranes for pre-combustion CO2 capture
Expected completion date	Jan 2020
Estimated size (number of pages)	105
Requestor Location	Christin Eden Emily Hob-house Street 13 Pennsylvania. Honeydew Ridge Estate 2 Honeydew Johannesburg, Gauteng 7188 South Africa Attn: Christin Eden
Publisher Tax ID	ZA 4110266048
Total	0.00 AUD
Terms and Conditions	

D.2) Figure 2

This Agreement between Christin Eden ("You") and Elsevier ("Elsevier") consists of your license details and the terms and conditions provided by Elsevier and Copyright Clearance Centre.

License Number	4702950307382

License date	Nov 06, 2019
Licensed Content Publisher	Elsevier
Licensed Content Publication	Journal of Membrane Science
Licensed Content Title	Synthesis of thin defect-free hydroxy sodalite membranes: New candidate for activated water permeation
Licensed Content Author	Sheida Khajavi,Freek Kapteijn,Jacobus C. Jansen
Licensed Content Date	Aug 1, 2007
Licensed Content Volume	299
Licensed Content Issue	1-2
Licensed Content Pages	10
Start Page	63
End Page	72
Type of Use	reuse in a thesis/dissertation
Portion	figures/tables/illustrations
Number of figures/tables/illustrations	1
Format	both print and electronic
Are you the author of this Elsevier article?	No
Will you be translating?	No
Title	Synthesis and performance evaluation of optimized silica sodalite in polysulfone mixed matrix membranes for pre-combustion CO2 capture
Institution name	n/a

Expected presentation date	Jan 2020
Portions	fig. 1
Requestor Location	Christin Eden Emily Hob-house Street 13 Pennsylvania. Honeydew Ridge Estate 2 Honeydew Johannesburg, Gauteng 7188 South Africa Attn: Christin Eden
Publisher Tax ID	ZA 4110266048
Total	0.00 AUD

D.3) Figure A.4

ELSEVIER LICENSE
TERMS AND CONDITIONS
Sep 06, 2020

This Agreement between Christin Eden ("You") and Elsevier ("Elsevier") consists of your license details and the terms and conditions provided by Elsevier and Copyright Clearance Center.

License Number	4903110738332
License date	Sep 06, 2020
Licensed Content Publisher	Elsevier
Licensed Content Publication	Microporous and Mesoporous Materials
Licensed Content Title	A novel synthetic route to obtain RUB-15 phase by pseudo solid-state conversion
Licensed Content Author	Fethi Kooli,Yan Liu,Kais Hbaieb,Rawan Al-Faze
Licensed Content Date	Jul 1, 2016
Licensed Content Volume	228
Licensed Content Issue	n/a
Licensed Content Pages	7
Start Page	116
End Page	122
Type of Use	reuse in a thesis/dissertation
Portion	figures/tables/illustrations
Number of figures/tables/illustrations	1

Format	electronic
Are you the author of this Elsevier article?	No
Will you be translating?	No
Title	Synthesis and performance evaluation of optimized silica sodalite in polysulfone mixed matrix membranes for pre-combustion CO2 capture
Institution name	University of the Witwatersrand
Expected presentation date	Nov 2020
Portions	Figure 1 and 2
Requestor Location	Christin Eden Emily Hob-house Street 13 Pennsylvania. Honeydew Ridge Estate 2 Honeydew Johannesburg, Gauteng 7188 South Africa Attn: Christin Eden
Publisher Tax ID	ZA 4110266048
Total	0.00 AUD

Appendix E: Copy of first page of publications

TCCS-10, 2019
Trondheim, Norway

The 10th Trondheim Conference on CO_2 Capture, Transport and Storage
June 17-19, 2019

DEVELOPMENT OF SILICA SODALITE WITH ENHANCED POROSITY VIA TOPOTACTIC SYNTHESIS FOR PRE COMBUSTION CO_2 CAPTURE

C-I. Eden, N. Ntombela, M.O. Daramola*

School of Chemical and Metallurgical Engineering, Faculty of Engineering and the Built Environment, University of the Witwatersrand, Johannesburg, South Africa

* Corresponding author e-mail: michael.daramola@wits.ac.za

Abstract

Topotactic conversion of layered silicates is reported to yield sodalite with enhanced frameworks, chemical compositions and predictable outcomes. Traditional hydrothermal synthesis results in sodalite with occluded matter preventing the effective use of sodalite cages for adsorption and separation applications. However, the reproducibility of high quality silica sodalite depends on obtaining optimized synthesis conditions and investigating the effect these conditions is essential. A 2^3 factorial design was employed to investigate the effect of process variables (acid strength, acid treatment time and calcination temperature) on the quality of silica sodalite produced via topotactic conversion in this study. XRD, SEM and Nitrogen physisorption at 77K were used for physio-chemical characterization of the sodalite samples. The produced sodalite crystals were used in membrane synthesis, and the membrane was tested for $CO_2/H_2/N_2$ separation. Sodalite of desirable crystallinity and plate-like morphology was produced with surface area and porosity of 79.44m^2/g and 0.081cm^3/g, respectively. An incomplete transformation of sodalite at low acid concentration and treatment time was experienced. A significant improvement on surface area and pore volume was reported on all samples as compared to that of the hydroxy sodalite. Analysis of the regression model obtained from the experimental data indicates acid treatment time as an insignificant variable. The preliminary investigation of the application for membrane synthesis indicates enhanced porosity of the HSOD improved the membrane H_2 permeance by 178%.

Keywords: *Silica sodalite, Topotactic conversion, Response surface methodology*

1. Introduction

Increasing levels of anthropogenic CO_2 have been noted as a major cause for environmental climate change. The most effective means for remediation focuses on point-source emission such as power plants [1]. The majority of the world's energy production comes from the combustion of fossil fuels, and an example of a system employed to achieve this is the Natural Gas Combined Cycle (NGCC) or Integrated Gasification Combined Cycle (IGCC) which result in large volumes of CO_2 emissions [2]. The depletion of fossil fuels and the increasing energy demand have led to a global movement utilize environmentally damaging chemicals [7, 8]. Membrane systems provide an alternative with low energy intensity, operating and capital costs as well as high flux [9]. However, the high temperature and steam utilized in coal gasification means that membranes used for in pre-combustion CO_2 capture need to be thermally and hydro-thermally stable, with good separation performance to make them an economically feasible alternative to traditional methods [9, 10]. Polymeric membranes form the majority of membranes current used in industry, however these membranes can be brittle and exhibit an undesirable trade-off between permeability

ARTICLE IN PRESS

Materials Today: Proceedings xxx (xxxx) xxx

Contents lists available at ScienceDirect

Materials Today: Proceedings

journal homepage: www.elsevier.com/locate/matpr

Evaluation of silica sodalite infused polysulfone mixed matrix membranes during H_2/CO_2 separation

C.L. Eden [a], M.O. Daramola [b,*]

[a] School of Chemical and Metallurgical Engineering, Faculty of Engineerinng and the Built Environment, University of the Witwatersrand, Wits 2050, Johannesburg, South Africa
[b] Department of Chemical Engineering, Faculty of Engineering, Built Environment and Information Technology, University of Pretoria, Private Bag X20 Hatfield, Pretoria 0028, South Africa

ARTICLE INFO

Article history:
Received 17 November 2019
Received in revised form 10 February 2020
Accepted 16 February 2020
Available online xxxx

Keywords:
Silica sodalite
Mixed matrix membranes
Pre-combustion
Carbon capture
Nanocomposite
Global warming

ABSTRACT

Global warming and environmental degradation have stimulated the drive towards the capture of large point source carbon emissions and reducing high energy intensity of industrial processes. Mixed membranes infused with high porosity silica sodalite are potential useful for pre-combustion CO_2 capture. However, development of high quality mixed matrix membranes is a challenge. In this study, silica sodalite (SSOD) infused polysulfone (PSF) membranes were developed and evaluated for pre-combustion CO_2 capture. The SSOD was obtained via topotactic conversion of layered silicates; and the membrane was prepared using the phase inversion method. The physicochemical nature of the SSOD and the SSOD/PSF was checked using XRD, SEM, and N_2 physisorption at 77 K. Single gas permeation used to check membrane quality. N_2 physisorption shows that the SSOD possesses higher surface area of 56.56 m^2/g and pore volume of 0.181 cm^3/g, when compared to that of the hydrothermally-synthesized hydroxy sodalite (HSOD) crystals (surface area: 27.43 m^2/g; pore volume: 0.084 cm^3/g). The SSOD/PSF membrane is asymmetric with higher mechanical strength than the ordinary PSF. Loading the PSF with SSOD enhanced its H_2 permeance from 4.9×10^{-7} $mol/m^2 \cdot s \cdot Pa$ but with a decrease in H_2/CO_2 separation factor from 2.2 to 0.6. While the enhanced H_2 permeance is attributed to the enhanced porosity of the SSOD, the ideal selectivity is low but still within the values reported in literature. Increasing the SSOD loading up to 10 wt% enhanced the quality and performance of the PSF membrane, displaying H_2 permeance of 6.5×10^{-7} $mol/m^2 \cdot s \cdot Pa$ and a separation factor of 1.1. Though results reported in this study are promising, a robust synthesis protocol that will further enhance both the H_2 selectivity and H_2 permeance of the membrane is required. Furthermore, more studies are required on the process optimization and techno-economic feasibility for pre-combustion CO_2 capture.
© 2020 Elsevier Ltd. All rights reserved.
Selection and peer-review under responsibility of the scientific committee of the International Symposium on Nanostructured, Nanoengineered and Advanced Materials.

1. Introduction

Rapid environmental change and global warming associated with increasing levels of anthropogenic carbon dioxide have seen a global push towards carbon capture and the high energy efficiency of industrial processes. In addition, the increasing energy from large point source emitters such as power plants is vital for sustainable energy generation. Pre-combustion carbon capture is favourable over post-combustion methods due to the higher CO_2 concentration (>20%) and pressure in the H_2/CO_2 flue gas [2]. Integrated gasification combined cycle (IGCC) power plants generate synthesis gas through the gasification process by heating carbon

Appendix F: Similarity Index Report

803769:plagiarism_check.docx

ORIGINALITY REPORT

11%	3%	7%	7%
SIMILARITY INDEX	INTERNET SOURCES	PUBLICATIONS	STUDENT PAPERS

PRIMARY SOURCES

1	Masakazu Koike, Yusuke Asakura, Megumi Sugihara, Yoshiyuki Kuroda, Hidehiro Tsuzura, Hiroaki Wada, Atsushi Shimojima, Kazuyuki Kuroda. "Topotactic Conversion of Layered Silicate RUB-15 to Silica Sodalite through Interlayer Condensation in N-Methylformamide", Dalton Trans., 2017 Publication	1%
2	Hoang Vinh-Thang, Serge Kaliaguine. "Predictive Models for Mixed-Matrix Membrane Performance: A Review", Chemical Reviews, 2013 Publication	<1%
3	Submitted to Universiti Teknologi Petronas Student Paper	<1%
4	Submitted to University of Witwatersrand Student Paper	<1%
5	link.springer.com Internet Source	<1%
	etd.lib.metu.edu.tr	